Electrochemical detection of 4-chlorophenol on phthalocyanine-metal organic framework sensors

by

Nokubongwa Xol'sile Dlamini

Submitted in fulfilment of the requirements for the degree

Master of Science in Chemistry

In the Faculty of Natural & Agricultural Sciences

University of Pretoria

Pretoria

February 2022

Declaration

I, Nokubongwa Xol'sile Dlamini declare that the dissertation, which I hereby submit for the degree Master of Science in Chemistry at the University of Pretoria, is my own work and has not previously been submitted by me for a degree at this or any other tertiary institution.

SIGNATURE: ……

DATE: …….

Dedication

To my mother

Lencane Mary Dlamini

Acknowledgements

Dear God, I come before you, to thank you for being my strength and shield, for the gift of wisdom and understanding throughout my academic journey.

I am grateful to my supervisors, Dr N Nombona and Prof M Diale for the continued support, words of encouragement, patience, and guidance throughout this study. I am privileged to have learnt from the best.

I would like to thank my parents for helping me to shape my life with positivity and love. To my mother ngiyabonga Nkhosi, the sacrifices you made for me to be where I am today do not go unnoticed. Thank you for believing in me, I am because you are! To my siblings, Nomfanelo (mamcool) and Nonkosi (bestie) thank you for the love and support. To the babies, Simelesihle and Asimile, believe that you can, and you will.

I wish to thank the University of Pretoria for providing a conducive environment to carry out this research and the National Research Foundation for financial support.

To my lab mates and friends, thank you for entertaining my silly jokes and for lunch times. It has been good.

Abstract

Metal organic frameworks (MOFs) have been used as electrochemical sensors owing to their high surface area and porosity. Unfortunately, the low conductivity and redox activity of MOFs limit their application in electrochemical sensing. To address this problem redox-active materials can be incorporated in MOFs to produce MOF composites. In this work we report on the synthesis and characterization of Zeolitic imidazolate framework-8 (ZIF-8), Zirconium based MOF (UiO-66) and their corresponding phthalocyanine (Pc) composites. Solvothermal synthesis was used to obtain ZIF-8, UiO-66, and their composites in powder form. The morphology and elemental composition were attained using scanning electron microscopy (SEM) and energy dispersive X-ray (EDX) analysis, respectively. The composites were composed of agglomerated rods surrounded by irregular polyhedral structures. The presence of MOF and Pc elements confirmed that the Pcs were within the MOFs. The crystallographic properties of the composites were probed using powder X-ray diffraction (PXRD) which showed that the composites were more crystalline than the pristine MOFs. The increase in order of the structure of the composites confirmed incorporation of the Pcs onto the MOFs. The surface area and pore size distribution of the composites were determined using Brunauer-Emmett-Teller (BET) analysis. The pore volume ranged from 0.10 to 0.37 cc/g. The decrease in surface area and pore volume of the composites indicated that the Pcs were adsorbed onto the MOF pores. The optical properties of the composites were obtained using ultraviolet-visible (UV-vis) spectroscopy. The composites exhibited the characteristic B and Q bands of phthalocyanines and showed metal-to-metal charge transfer between MOFs and Pcs confirming that the phthalocyanines were incorporated within the MOF structure. ZIF-8, UiO-66 and their corresponding phthalocyanine composites were immobilized on a glassy carbon electrode (GCE) using the drop drying method. The modified electrodes were used for the detection of 4-chlorophenol, and the electrochemical responses were recorded using cyclic voltammetry. The electrocatalytic behaviour of the electrodes modified with MOF composites showed improved oxidation compared to the ZIF-8 or UiO-66 modified electrodes. The FePc@ZIF-8 modified electrode showed the best catalytic behaviour with an anodic peak potential at 0.54 V while FePc@UiO-66 behaved best with respect to enhancing catalytic currents. The limit of detection ranged from 0.05 mM to 2.8 mM for all redox active composites. This work shows that phthalocyanine-MOF composites are effective electro-catalysts and may be developed for the detection of other environmental pollutants.

Table of contents

Chapter 3: Experimental

Chapter 4: Results and discussion

Chapter 5: Electrocatalysis

Chapter 6: Conclusion and future prospects

Supplementary information

References

List of abbreviations

^{1}H-NMR	Proton nuclear magnetic resonance
AFM	Atomic force microscopy
ATR	Attenuated total reflectance
AuNPs	Gold nanoparticles
BET	Brunauer-Emmett-Teller
CNTs	Carbon nanotubes
CPs	Chlorophenols
CPE	Carbon paste electrode
CV	Cyclic voltammetry
DBU	1,8-Diazobicyclo (5.4.0) undec-7-ene
DMF	N, N- dimethylformamide
DMSO	Dimethyl sulfoxide
DNA	Deoxyribonucleic acid
DOXO	Doxorubicin
DSSC	Dye sensitized solar cell
EDCs	Endocrine disrupting compounds
EDX	Energy dispersive X-ray
EWC	Emerging water contaminants
FTIR	Fourier transform infrared
FWHM	Full width at half maximum
GCE	Glassy carbon electrode
HCC	Hepatocellular carcinoma
HER	Hydrogen evolution reaction

HOMO	Highest occupied molecular orbital
ILAG	Ion-and-liquid assisted grinding
IUPAC	International Union of Pure and Applied Chemistry
LAG	Ligand assisted grinding
LIBs	Lithium batteries
LMCT	Ligand to metal charge transfer
LUMO	Lowest unoccupied molecular orbital
MA	Monocarboxylic acid
MIL	Materials of Institute Lavoisier
MLCT	Metal to ligand charge transfer
MMCT	Metal to metal charge transfer
MOF	Metal organic frameworks
MWCNTs	Multi walled carbon nanotubes
MPc	Metallophthalocyanines
MRI	Magnetic resonance imaging
MS	Mechanochemical synthesis
NG	Neat grinding
NMR	Nuclear magnet resonance
NPs	Nanoparticles
OER	Oxygen evolution reaction
ORR	Oxygen reduction reaction
PBS	Phosphate buffered saline
Pc	Phthalocyanine
PPCPs	Pharmaceuticals and personal care products

PV	Photovoltaic
PXRD	Powder X-ray diffraction
siRNAs	Small interfering ribonucleic acids
RD	Rhombic dodecahedral
ROS	Reactive oxidative species
SBU	Secondary subunits
SCE	Saturated calomel electrode
SEM	Scanning electron microscopy
SOD	Sodalite
SURMOFs	Surface supported metal organic frameworks
TC	Truncated cubes
TMDs	Transitional metal dichalcogenides
TNTs	Titanium dioxide nanotubes
TRD	Truncated rhombic dodecahedral
UiO-66	Zirconium based MOF
UV	Ultraviolet
UV-vis	Ultraviolet-visible
XPS	X-ray photoelectron spectroscopy
ZIF-8	Zeolitic imidazolate framework-8

List of symbols

µ	Micro
g	Gram
p	Pico
L	Litre
δ	Deuterated
cm	Centimetre
m	Metre
ml	Millilitre
MHz	Megahertz
nm	Nanometre
kHz	Kilohertz
λ	Wavelength
$\mathbf{V_P}$	Pore volume
α	Electron transfer coefficient
v	Scan rate
R	Gas constant
T	Temperature
Q	Total charge
β	Peak broadening
D	Diffusion coefficient
C	Concentration
A	Surface area of the electrode
F	Faraday's constant

n	Number of electrons
I_p	Peak current
Γ	Surface coverage
E_i	Initial potential
E_f	Switching potential
E_{pa}	Anodic potential
I_{pa}	Anodic current
E_{pc}	Cathodic potential
I_{pc}	Cathodic current

List of figures

List of schemes

List of tables

Chapter 1: Introduction

1.1 Background

Water is the earth's most abundant natural resource. However, environmental pollution, which may be described as the introduction of foreign materials to the ecosystem remains a problem globally as it poses a threat to living organism, including human health. Industrialisation has led to the increase of pollutants released into the environment and is the main source of water pollution. The introduction of foreign substances into the aquatic environment impairs the water quality which affects aquatic life and causes adverse effects to human health leading to an imbalance in the ecosystem. Human beings are mainly exposed to pollutants in water through ingestion of contaminated water and aquatic products. These pollutants are then absorbed by the body and failure of the biological system to break them down or flush them out of the body results in accumulation of foreign substances in biological tissues causing undesirable health issues (*1*).

Apart from rapid industrialisation, sewage discharge into water streams and surface run off from agricultural land where synthetic chemicals are used are also prominent sources of water pollution (*2*). Although there are different types of water pollutants, micropollutants will be pertinent in this study. There has been growing concern in the occurrence of micropollutants in water bodies over the last couple of years. Natural and synthetic compounds may both be regarded as micropollutants, these include personal care products (PPCPs), pharmaceuticals, and endocrine disrupting compounds (EDCs). Despite their existence in the aquatic environment at very low concentrations ($pg.L^{-1}$ to $\mu g.L^{-1}$), they are still associated with ecotoxicological effects such as endocrine disruption, resistance of microorganisms to antibiotics, interference in platelet, white and red blood cell production, and many other deleterious effects to human health (*3*, *4*).

On release into the environment, micropollutants undergo degradation which determine their elimination. Sedimentation, filtration, and disinfecting form part of the main existing techniques for water purification. Unfortunately, these techniques are not targeted on the elimination of micropollutants in water but rather on that of suspended particles and microorganisms (*3-6*). Recent studies have reported several methods for monitoring and elimination of micropollutants during the water treatment process and these depend on the physiochemical properties of a specific micropollutant. Chromatographic, spectrochemical, and electrochemical sensing techniques are part of these methods amongst others (*5-8*) and for

the purpose of this study we will focus on the latter, paying specific attention to metal organic frameworks (MOFs) and their composites as electrochemical sensors.

MOFs represent a category of porous materials with exceptional features amongst which a high surface area is the most outstanding. The chemical composition and structure differs from one framework to another, and this determines their application in storage, separation, and catalysis (*9-11*). When MOFs are employed as electrochemical sensors, the metal ions in MOFs are generally expected to exhibit electrocatalytic behaviour and the organic linkers to facilitate further catalysis by adsorbing target molecules (*12*). Regardless of all the excellent properties suggesting that MOFs are suitable candidates for electrochemical sensing, finding redox active MOFs is still a challenge, due to weak electronic transfer between organic linkers and non-redox-active metal within some MOFs. To address this problem, MOFs can be modified post synthesis, by forming composites through host-guest interactions as a benefit of their porous nature. Guest molecules that can be incorporated into MOFs to enhance their electrochemical performance include polymers, nanoparticles, carbon nanostructures, biomolecules and many more (*10, 13*).

Electrochemical sensors offer better selectivity and sensitivity for adsorption of various molecules compared to conventional analytical techniques such as chromatography and spectroscopy. Therefore, changing the surface chemistry of an already existing electrode can improve its detection limit towards a certain analyte. Thus, in this work we will pay attention to designing electrochemical sensors using electro-active MOF composites for surface modification of the glassy carbon electrode (GCE). GCE modified with MOFs and MOF composites have been reported for determination of a variety of analytes by numerous researchers. Those that have been studied intensely can be grouped into MOFs doped with biomolecules, metal oxide MOF composites, metal nanoparticle MOF composites, and MOFs incorporated with carbon nanomaterials (*9, 13*).

Carbon nanotubes (CNTs) have received the outmost popularity as carbon nanomaterials. They can be single, double, or multiple walled and are sp^2 hybridised. Their hollow cylindrical structure permits control of their diameter, length, and wall number (*9, 14*). Due to their outstanding electrical conductivity, CNTs have been used in sensor systems in combination with MOFs to improve their electrocatalytic activity (*9, 15*). For example, incorporating multi walled carbon nanotubes (MWCNTs) inside a nickel MOF (Ni-MOF) demonstrated that the Ni-MOF/MWCNT composite exhibited remarkable sensing ability with selectivity towards

urea and stability over a month (*16*). Geim and Novoselov discovered another nanomaterial based on carbon, this was graphene oxide (GO) and its high conductivity and electrocatalytic activity gained popularity within the scientific community. Like CNTs, GO is also sp^2 hybridised and its two-dimensional (2D) sheets offers a high surface area, allowing easy combination with metallic nanomaterials. It has also been reported that these sheets are responsible for effective electron transfer between GO and metallic materials such as MOFs (*9, 17*). In one case, Zhang *et al* developed a hybrid polyoxometalate based MOF integrated with reduced graphene oxide (POMOF/rGO) for dopamine detection. Both materials used were electrochemically active therefore a synergistic effect was observed towards dopamine oxidation due to π-π interactions between the composite and dopamine. Overall, the fabricated biosensor displayed good stability, reproducibility and selectivity (*18*).

Palladium, (Pd), copper (Cu), platinum (Pt), silver (Ag), and gold (Au) are some of the catalytically active metals that have been combined with MOFs for GCE modification in order to enhance the catalytical activity of the electrode. Owing to their high surface area, excellent electrochemical properties and biocompatible structure, gold nanoparticles (AuNPs) have been used for various sensor applications. Silver nanoparticles have also gained a lot of popularity over the years due to their superior electrical conductivity, photoelectrochemical and antimicrobial activity (*9, 13*). There are three strategies to explore in order to produce metal nanoparticle/MOF composites. Firstly, pre-synthesized nanoparticles can be loaded into MOFs. For example, Hosseini *et al* fabricated an electrocatalyst from Au-SH-SiO_2 doped Cu-MOF which showed efficient electrocatalytic activity for hydrazine and L-cysteine oxidation (*19, 20*).

The second method involves the production of nanoparticle/MOF composites within MOF cavities by using MOFs as templates. This strategy was used to generate AgNPs/Zn-MOF composites through the reduction of silver nitrate ($AgNO_3$) in aqueous solution containing preformed zinc MOF (Zn-MOF) and the composite modified GCE displayed improved electrocatalytic activity when used for hydrogen peroxide (H_2O_2) reduction (*21*). The third approach affords hybrid MOFs through a one pot synthesis procedure. For instance, efficient electrocatalysis for sodium borohydride ($NaBH_4$) oxidation was achieved with PtNPs/MOF composites synthesized using this method (*22*). Metal oxide/MOF composites have provided improved conductivity, good biocompatibility and high surface area and have been used as fluorescence sensors among other spectroscopic systems. The sensing ability of such composites is dependent on their spectroscopic properties (*9, 23*), while MOFs incapsulated

with biomolecules have proven to be highly efficient as biosensor, in drug delivery and various fields (*24*).

Porphyrins have also been used to form MOF composites. The macrocyclic compounds can either be used as a ligand in MOF formation or incorporated in an already existing MOF to form a composite (*10, 11, 25*). Porphyrins are redox active, and MOF composites based on them have shown good electrocatalytic activity for oxidation of various molecules. Owing to that, porphyrin-based MOFs have been used to develop electrochemical, colorimetric, and fluorescence sensors. Chemical selectivity between MOFs and guest molecules is attributed to open metal sites, hydrogen bonding, electrostatic and π-π interactions (*12, 13, 26*). Like porphyrins, phthalocyanine have been used for various sensing activity and their extended π-system permits rapid redox processes (*7, 27*) . Therefore, in this work will take advantage of the π-system in phthalocyanines (Pcs) to form π-π interactions between Pcs and Zeolite imidazolate framework-8 (ZIF-8). We will also form Pc@MOF composites using Zirconium based MOF (UiO-66). By doing so we hope to enhance catalytic selectivity and sensitivity of the MOFs towards 4-chlorophenol detection through the delocalization of π-electrons between the conjugated system of the organic molecules and the MOF composites.

1.2 Problem statements and justification

Water can be used for many purposes, the main one being human consumption. The rapid growth in population exacerbates pressure on existing water sources, especially in arid places that are faced with acute water resource constraints (*4*) . In cases where the water sources are deemed fit for human consumption, the prevalence of micropollutants still remains a challenge as monitoring them is still unregulated and water treatment plants are not equipped for eliminating them to afford clean water for human consumption (*6, 28*). The ability of micropollutants to cause severe health issues at trace levels make it even more necessary to monitor them and eliminate them from water to prevent them from accumulating or forming metabolites as this may impact human livelihood in the long term (*6*).

Although chromatography and mass spectrometry have been used for removal of micropollutants in water (*7, 8*), simple, inexpensive, and more specific techniques may be used for this purpose. Therefore, we propose a model for the efficient removal of 4-chlrophenol from water at low concentrations using metal organic frameworks (MOFs) incorporated with metallophthalocyanines (MPcs).

1.3 Hypothesis

Incorporation of MPcs in MOFs will enhance selectivity and sensitivity of metal organic framework ZIF-8 and UiO-66 as electrocatalysts for the detection of 4-chlorophenol.

1.4 Aims and objectives

The study aims at the application of cyclic voltammetry for more efficient detection of 4-chlorophenol in aqueous media using ZIF-8 or UiO-66 composite modified GCE.

In order to accomplish this, the following objectives are proposed:

i. Synthesis and characterization of metallophthalocyanines.
ii. Synthesis and characterization of metal organic frameworks.
iii. Synthesis and characterization of MPc@MOF composites.
iv. Electrochemical detection of 4-chlorophenol in aqueous solution.

Chapter 2: Literature review

2.1 Metal organic frameworks (MOFs) and their properties

Metal organic frameworks (MOFs) are crystalline materials formed when polyatomic organic ligands which may be negatively charged or aromatic (mainly carboxylic acids and nitrogen containing ligands) coordinate to metal ions and bridge to connect metal centres (**Fig. 2.1)** (*29-32*) . A certain criterion is followed for a compound to be referred to as a MOF. That includes, a distinct geometric structure which implies high crystallinity of the compound, modifiability of the organic ligands which link secondary subunits (SBUs) to form frameworks and strong bonding between SBUs as strong bonding interactions provides stability to the framework (*33, 34*).

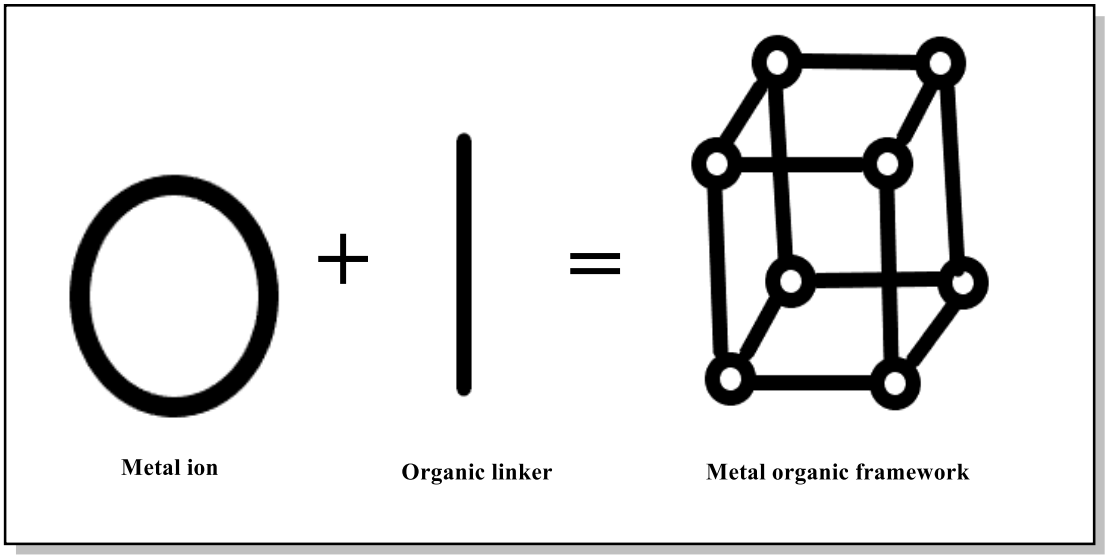

Figure 2.1: Components of metal-organic frameworks.

The appearance of MOFs dates back to the 1990s with the likes of HKUST-1 (HKUST- Hong Kong University of Science and Technology) and MOF-2 which had a relatively low surface area (*35, 36*). Later developments in MOF research led to the discovery of NU-110 (NU - North-western University) and MIL-101 (MIL - Materials of Institute Lavoisier) (*34*). These, among others are highly porous with a surface area ranging from 1000 to 10 000 $m^2.g^{-1}$ which is greater than most conventional porous materials (*37, 38*). The characteristics mentioned above render MOFs suitable for applications such as catalysis, biomedicine, gas storage, sensors, and photovoltaic cells (*34, 39-41*).

2.2 General synthesis of MOFs

Different synthetic routes are required for MOFs as they have a major effect on the morphology, particle size, yield, and reaction time. Therefore, different methods have been used for the synthesis of MOFs. These include the conventional, sonochemical, mechanochemical, microwave assisted and electrochemical syntheses (*42*).

2.2.1 Conventional syntheses

The basis of this method is the temperature range, which is distinguished by two categories namely, solvothermal and non-solvothermal. Reactions that are carried above solvent boiling point in a closed system and rely on internal pressure are denoted solvothermal. Contrary to that, non-solvothermal reactions are carried out at temperatures that do not exceed the boiling point of the solvent under ambient pressure (*42*).

These reactions allow the control of the nucleation rate and crystal growth through adjustment of reaction conditions. Common MOFs (**Fig. 2.2**) such as MOF-5, HKUST-1, and ZIF-8 have been synthesized at room temperature. Some of these MOFs for example, ZIF-8 and MOF-5 have good chemical and thermal stability (*42, 43*).

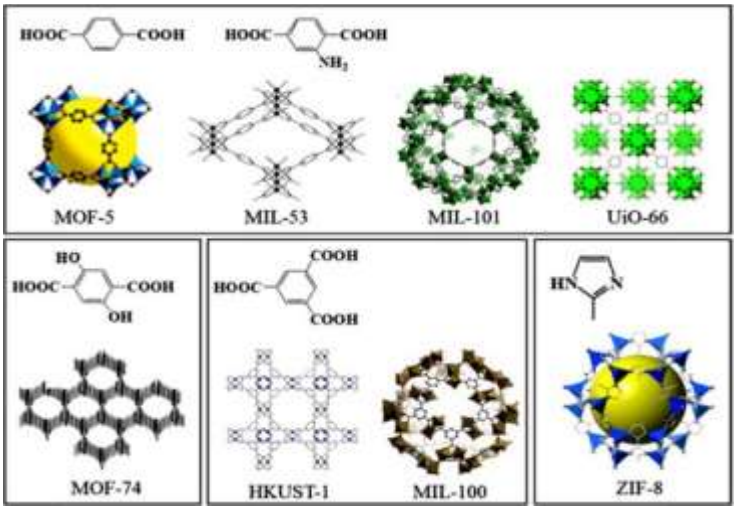

Figure 2.2: Examples of common MOFs and ligands (*32*).

2.2.2 Sonochemical synthesis

Sonochemistry is based on the interaction between matter and energy. For a reaction to proceed, some form of energy is required and, in this case, that energy is supplied by ultrasound (*42, 44*). Stock *et al* (*42*) described ultrasound as a mechanical vibration with a frequency

between 20 kHz and 10 MHz. Vibrations occur in cycles and when high energy ultrasound interacts with liquids, an area of compressions and rarefaction are formed.

Cavities (small bubbles) are formed at low pressure regions (rarefaction). Cavity formation is a result of a pressure drop below that of the solvent or reactant's vapour pressure. Under alternating pressure, the vapor of the solute diffuses into the bubble which grows and accumulate ultrasound energy until they reach a maximum size at which they become unstable and collapse, releasing energy rapidly. This process is known as caviation.

2.2.3 Mechanochemical synthesis

The drawbacks of solvothermal techniques is that they require long reaction times and utilize organic solvents which have serious environmental consequences. To avoid these, mechanochemical synthesis can be employed. This type of synthesis involves intermolecular bond breaking followed by chemical transformation (*42*).

Mechanochemical synthesis (MS) is conducted in solid state or solvent free environment, whereby coordination and polymerization reactions are a result of mechanically induced molecular-surface collisions. MS is suitable for large scale synthesis of MOFs with organic linkers that have poor solubility in common solvents (*30*).

MS has drawn attention as a green synthesis route because reactions can occur at room temperature without the use of organic solvents. Reaction times are shortened (10 - 60 min) with high yields. MOFs that are small in particle size are formed and where metal oxides are used as precursors, only water is a by-product (*30, 42*).

There are three ways of constructing MOFs through mechanochemical synthesis. The first method is known as neat grinding (NG), a method in which the reaction progresses in the absence of a solvent. The formation of a MOF is accomplished by utilizing oxides/hydroxides as a metal source which in combination with protons generated by organic ligands form water as a by-product. Secondly, ligand assisted grinding (LAG) may be used. This method uses catalytic amounts of liquid phase to increase the mobility of reagents, thus resulting in a quicker and versatile reaction. Lastly, ion-and-liquid assisted grinding (ILAG) uses small amounts of solvent with trace amounts of salt derivatives to speed up MOF formation (*30, 42*).

2.2.4 Microwave assisted synthesis

Energy introduction through microwave radiation is a common technique in synthetic chemistry, particularly in organic chemistry. Electromagnetic and electronic interactions between molecules in polar solvents, electrons, ions in solid or solution is the basis of the method. In the latter case and in the presence of an oscillating electromagnetic field, polar molecules align themselves while solids form an electric current and the solid's resistance to the current is responsible for heating. Thus, when the appropriate frequency is applied, the kinetic energy of the system increases due to molecular collisions. MOFs syntheses using microwave (MW) assisted synthesis has focused mainly on production of nanoscale material, improvement of product purity, acceleration of crystallization and selective synthesis of polymorphs (*42*).

Stock *et al* (*42*) reported the first synthesis of MOFs using MW assisted synthesis which focused on Cr-MIL-100. They recorded a product yield of 44% which was comparable to that obtained using the conventional synthesis method. Nanosized Cr-MIL-101 (~50 nm) has been synthesized by optimizing reaction conditions like water, concentration, and pH. It was reported that size decreased with increase in pH and a decrease in water concentration (*45*). A 37% yield was recorded from synthesis of MIL-101 using MW (*42*, *45*). According to Khan *et al* MIL-101 was the smallest MOF obtained in fair yield in solid phase (*45*).

2.2.5 Electrochemical synthesis

In electrochemistry, MOFs serve as catalysts in energy conversion reactions. These include hydrogen evolution reaction (HER), oxygen evolution reaction (OER) as well as oxygen reduction reaction (ORR) (*40*).

The wish to obtain high productivity of MOF HKUST-1 lead to the development of electrochemical synthesis of MOFs (*32*, *42*). The reaction setup of electrochemical synthesis of MOFs requires a battery cell which acts as a power supply, an electrochemical medium in which a cathode and an anode are immersed in. This medium contains the organic linkers and metal salts needed for formation of a desired MOF (**Fig. 2.3**) (*32*).

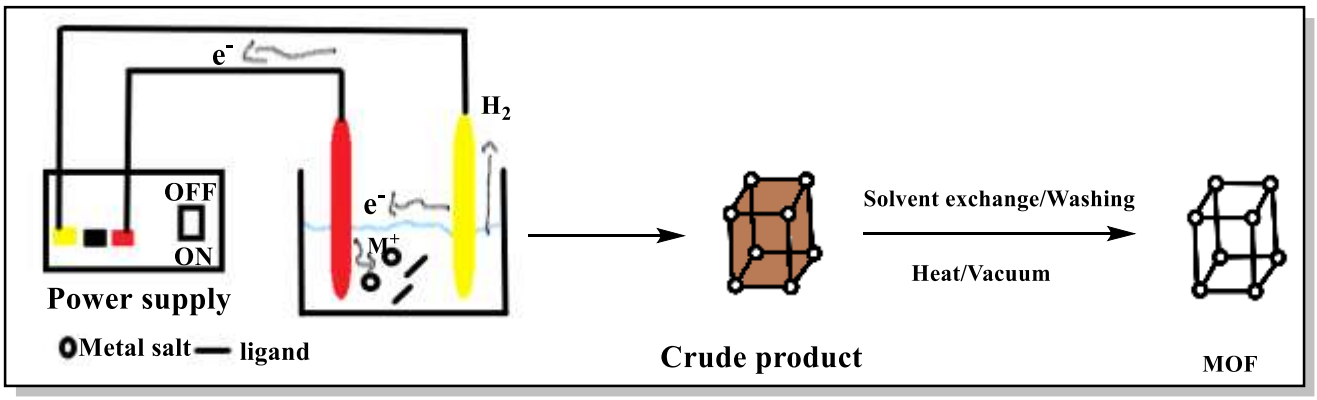

Figure 2.3: Electrochemical synthesis of MOFs.

In electrochemical synthesis of MOFs, anodic dissolution is responsible for the continuous introduction of metal ions to the reaction medium instead of using metal salts. Protic solvents are utilized to prevent metal deposition on the cathode and in turn hydrogen gas (H_2) is formed (*32*, *42*).

2.3 Applications of MOFs

2.3.1 Gas separation

Gas separation is carried out for separation of gases that usually consist of elements having concentrations in the same order of magnitude. The gas uptake ability of MOF-5 was reported as the property that could make it possible to separate rare gas mixtures through adsorption on the MOF. Rare gas mixtures are normally found technically under low temperature air separation units (*46*).

In contrast to gas purification reactions, three techniques are used to separate gas mixtures. These are distillation, pressure thermal and thermal swing adsorption-desorption (*31*). The noble gas mixture of krypton and xenon (Kr-Xe) has been performed on MOF adsorbents using pressure swing adsorption (*31*, *46*) . Upon gas separation of krypton and xenon, the two can be marketed individually. Krypton can be used as a filler in lamp industry, while xenon can be used as a narcotic medical gas (*31*).

Gas separations are essential for clean energy applications and environmental sustainability. Natural gas, for example, contains high amounts of acidic gases (H_2S and CO_2) which we need to get rid of in order to prevent pipeline corrosion and to increase the heating value. Hydrogen and carbon dioxide (H_2/CO_2) separation is important for H_2 purifications and pre-combustion

of CO_2 captured in power plants. Gas separation membranes made up of two-dimensional (2D) nanomaterials like graphene oxide, transitional metal dichalcogenides (TMDs) and zeolite nanosheets has been used for gas separation processes. These are highly efficient, which is attributed to their molecular thickness and extremely low mass-transfer barrier. 2D MOF nanosheet based membranes have shown some potential in gas separation processes and are expected to be highly efficient (selective) and attain high productivity (permeability) due to their well-defined pore structures and nano-meter thickness which recognises small gas molecules based on shape and size (*39*).

2.3.2 Biomedicine

The high porosity, tunable pore structure, large surface area and biodegradability of MOFs makes MOF nanoparticles suitable for host-guest chemistry (*34*, *39*). Evans *et al* reported on a drug delivery system that demonstrate desired control of guest encapsulation and release using MOF nanoparticles and their modified counterparts. For example, nanoparticles of MOFs Cr-MIL-101 and Fe-MIL-100 were utilized as carriers of biologically active cargo. These were treated with a dispersion of lipids which led to the formation of a lipid bilayer around the MOF. This resulted in the development of a system for dye loaded MOF nanoparticles coated with the bilayer which was loaded into target cancer cells. The active compounds of the nanoparticles were delivered inside the cancer cells to carry out their function by triggering them with a surfactant like triton X-100 (*34*).

Zhao *et al* reported on the use of UiO (Zr-MOF) nanosheets for simultaneous and efficient delivery of cisplatin and pooled small interfering RNAs (siRNAs) to drug resistant ovarian cancer cells. The large pore size of UiO permits for loading of cisplatin while siRNA coordinates to vacant sites on zirconium (Zr) which increases the chemotherapeutic efficacy in vitro (*39*).

2.3.3 Sensors

MOFs have proven to be good candidates as detectors of various compounds in aqueous solution (*32*). Achievements have been made in the detection of glucose, heavy metal ions, hydrogen peroxide (H_2O_2) etc. owing to developments in nanostructured MOFs that have been

used as electrochemical sensors. To afford electrochemical sensing capabilities, active ligands and metals are utilized for the introduction of catalytic and redox active sites to the MOF (*40*).

Evans *et al* reported that MOFs possess emission properties and that their tunability renders them as suitable candidates for sensing of hazardous material such as biomolecules, solvents, and ions. Five pathways are responsible for the emission property in MOFs, they are metal based emission, ligand based emission, metal to metal charge transfer (MMCT), metal to ligand charge transfer (MLCT) and ligand to metal charge transfer (LMCT) (*34*). 2D MOF nanosheets were developed to meet the demand for highly sensitive and selective sensors. Due to their high surface area, they have been used for the detection of adenosine, microRNA and DNA (*39*).

2.3.4 Gas storage

Global warming and depletion of fossil fuels inspired research in the field of gas storage and the exploration of alternative renewable energy resources. Gas adsorption is dependent on the surface at which molecules adsorb, therefore the surface area and porosity of MOFs allows for capture of energy rich gases like hydrogen and hydrocarbons (*34, 41*). Also, MOFs can be used for capturing carbon monoxide and other greenhouse gases (*34*).

Hydrogen is considered a clean energy carrier, reason being that on its oxidation in fuel cells or engines, it only produces water as a by-product. Thus, it is an inexhaustible source of water. Also, fuel cells that utilize hydrogen as an energy source were reported to have an efficiency that is more than two-folds when compared to that of internal combustion engines. Regardless of these attractive attributes, the major drawback lies in the lack of efficient, economical, and safe systems for hydrogen storage. Since the realisation of hydrogen adsorption on MOFs, numerous MOFs have been developed and has shown better performances as hydrogen sorbents compared to other porous materials (*47*).

Like hydrogen, methane gas is also considered as a clean energy source. Due to its high hydrogen-to-carbon ratio and low carbon emission, it provides more energy, and its purification is simpler compared to petroleum oil. Normally, methane is stored in high-pressure tanks. These tanks are heavy and potentially explosive, therefore the porosity of MOFs prompted their use as methane storage systems although the first measurement done on MOFs reported limited uptake. The field of methane storage in MOFs is still developing but at a slower pace than hydrogen storage (*47*).

MOFs have been successfully used for CO_2 capture as well in attempt to solve the global warming issue attributed to high carbon dioxide (CO_2) emission due to high energy consumption. This application takes advantage of the high surface area and porosity of MOFs (*47, 48*). The high thermal stability, modifiable chemical functionality and ordered structure of MOFs also qualifies them as a superior medium for CO_2 adsorption (*48*).

2.3.5 Catalysis

The defined framework of MOFs can be tuned chemically from inside the MOF, this makes them attractive for catalysis. Compared to conventional homogenous catalysts, MOFs are heterogenous which deems them fit for recycling and easy removal of the catalyst. MOF based catalysts can be divided into MOFs with an active site at the metal centre and composites where the MOF acts as a support for the active catalyst. Structural integrity and rigidity of the framework is gained from the metal ions functioning as structural nodes. These may however serve as sites for catalysis, depending on the coordination environment (*34*).

Catalytic reactions in which MOFs have shown promise include electrocatalysis, and photocatalysis. In photocatalysis, a reaction relies on the conversion of solar energy to chemical energy (*32*) while in electrocatalysis a chemical reaction occurs at an electrode-analyte interface. Catalytic reactions on MOFs have been used for water remediation, water oxidation, H_2 and CO_2 generation among others. Due to their good porosity and high surface area which can provide multiple metal sites for electrocatalytic reactions, MOFs have shown potential as substitutes for the scarce and cost inefficient platinum-based catalyst (*32, 40*).

2.3.6 Photovoltaic cells

Photovoltaic (PV) cells have gained a lot of attention as a green energy source. Regardless of the silicon solar cell that have been commercialized, more efficient charge separation is still required to increase the conversion factor of solar energy to electric energy. As a result, MOFs have been considered for this application (*41*). For example, MOF-5 was tested as an active material in a solar cell in the absence of a photosensitizing dye and an electrolyte that increases charge transport and prevents electron-hole recombination. A photocurrent was observed when the MOF-5 cell was illuminated with light from a solar simulator which indicated the conversion of solar energy to electrical energy (*49*).

In solar cells MOFs have been utilized to improve device performance by incorporating their powders into other materials such as perovskites to form composites (*50, 51*). However, on their own MOFs allow for the construction of novel materials by modifying the properties of the organic compounds used as SBUs. An example of this is the fabrication of solids based on porphyrin which has a high efficiency for absorbing visible light and converting it to electric energy (*52, 53*).

MOF based PV devices have been constructed following two concepts that involve the use of surface supported MOFs (SURMOFs), that being (a) all solid state SURMOF PV (b) dye sensitized solar cell (DSSC)-like SURMOF PV. A variety of compounds have demonstrated that SURMOFs and MOF thin films are suitable as photoactive layers in PV devices (*52*).

2.4 Porosity of MOFs

2.4.1 Porosity and specific surface area

In order to understand the physical properties of MOFs we first need to familiarise ourselves with the basic concepts of porous materials. In 1994, the International Union of Pure and Applied Chemistry (IUPAC) made this easy for all scientists when they published a report titled "Recommendations for the characterization of porous solids". This report describes a porous solid as a solid pore with cavities, channels or interstices, that are deeper than they are wider (*54*). Size is the major parameter for distinguishing between different porous solids which are grouped into three subclasses (*54-56*):

1. Micropores: Pore width is lesser than 2 nm.
2. Mesopores: Pore width is between 2 and 50 nm.
3. Macropores: Pore width is greater than 50 nm.

MOFs have a high surface areas and pore volume. The porosity of a material is measured with its specific surface area (S). This is the area accessible on a solid surface per unit mass of that material denoted with the unit $m^2.g^{-1}$. The Brunauer-Emmett-Teller (BET) theory is the standard method applied for determining the specific surface area of porous materials (*54, 56*). The specific surface area is measured with nitrogen gas sorption (adsorption and desorption) isotherms obtained at 77 K (*54, 57*). It is significant to note that BET analysis relies on the assumption that adsorption occurs by multilayer formation and that the number of adsorbed

layers is infinite at the saturation pressure, that is, adsorption occurs as if on a free surface (*57*). Adsorption isotherms are used to describe how adsorbates interact with porous materials and optimize their use. IUPAC classified adsorption isotherms into six main group (**Fig. 2.4**), with the first five types initially proposed by Brunauer and co-workers (*58*).

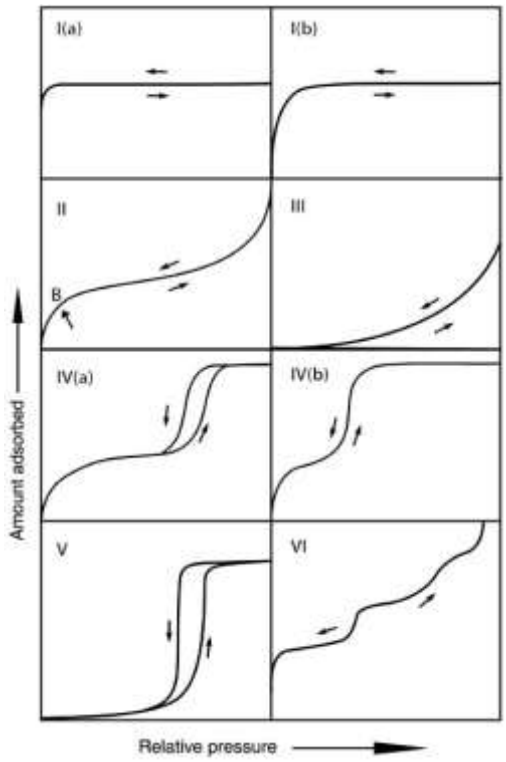

Figure 2.4: UIPAC adsorption isotherm classification (*58*).

Type I also known as the Langmuir isotherm is characteristic of microporous materials. It indicates an adsorption process with low affinity for the adsorbate while the plateau represents monolayer coverage, a typical behaviour for chemisorption during which the asymptotic approach to a limiting quantity shows that all of the surface sites are occupied. The reversible isotherm may be divided into two groups, type Ia being a result of microporous materials primarily having narrow micropores while type Ib is observed with materials having pore size distributions over a broader range (*58*). Type II isotherms (BET isotherms) are observed with physisorption and are commonly encountered when adsorption occurs on macroporous or non-porous powders. The inflection point (knee) on this isotherm termed 'point B' indicates completion of monolayer coverage and the onset of multilayer adsorption. Type III isotherms (Freundlich isotherms) are characteristic of microporous or non-porous solids due to weak attractive forces. This feature allows minimum uptake in the beginning but upon adsorption of a single molecule, the weak adsorbent-adsorbate interactions, promote clustering of adsorbed

molecules around the most favourable site on the solid surface. Monolayer and multilayer adsorption on mesoporous materials is describe by type IV isotherms. During adsorption there is an increase in adsorbate uptake as the pores are being filled. This may be observed with an increase in the slope. The knee of this type of isotherm generally occurs towards complete adsorption of the first monolayer, that is, towards the beginning of multilayer adsorption (*58, 59*).

Similarly, to type I isotherm, Type IV is also divided into two groups. A hysteresis loop is evident in a type IVa isotherm and is linked with the occurrence of pore condensation when the pore diameter surpasses a certain critical diameter that is dependent on the adsorption system and temperature. For simplicity, it worth noting that the first part of the isotherm corresponds to the type II isotherm in a non-porous form. Type IVb isotherms are observed for conical and cylindrical mesopores that are closed at the tapered ends. Type V isotherms which indicates pore condensation and hysteresis can be obtained with microporous or mesoporous solids (*58*). The initial part of this isotherm is identical to type III, indicating relatively weak interaction between the adsorbent and adsorbate. Lastly, type VI isotherms are borderline cases between the two or more aforementioned types. It is associated with rare layer-by-layer adsorption on a highly uniform non-porous surface and can be identified with steps, whose height represents the capacity of each adsorbed layer and its sharpness is dependent on the system and temperature (*58, 59*).

2.4.2 Pore volume and size distribution

Another important variable of MOFs that can be measured using BET analysis is pore volume (Vp). This is the total accessible volume per gram of adsorbent material given in the unit cm^3/g. The distribution of this volume with respect to the pore size is known as pore size distribution, which is an important property as it controls the diffusion of adsorbates into porous materials (*54, 56*). This concept assumes that the pores are cylindrical, therefore the size in question is the pore radius (rp). Thus the pore size distribution is represented by the derivative dVp/drp (*54*).

2.5 Zeolitic imidazole frameworks

Microporous materials with crystalline topologies analogous to that of zeolites exist as a subclass of MOFs. These are known as zeolitic imidazole frameworks (ZIFs). These were first reported by Chen *et al* and Yaghi *et al* almost concurrently in the early 2000s. ZIF structures are built through the connecting of 4 tetrahedral units (*60-63*). Unlike in zeolites, tetrahedral Si and Al are replaced by transitional metal ions Zn^{2+} or Co^{2+} while the bridging O is replaced by ligands derived from imidazolate (*63*).

Similar to zeolites, ZIFs are characterized by large cavities connected through small windows. This class of MOFs have rapidly become materials of interest due to their low toxicity, good biocompatibility, low cost, and exceptional chemical and thermal stability making them capable of diverse applications such as gas adsorption and storage, heterogenous catalysis, drug delivery and chemical sensing (*60-62, 64*). Our study will focus on ZIF-8, a widely investigated ZIF because it combines desirable properties of both zeolites and MOFs (*60, 65*).

2.5.1 ZIF-8

2.5.1.1 Properties of ZIF-8

ZIF-8 is composed of zinc ions coordinated with 2-methylimidazole (Hmim) in a tetrahedral geometry giving the chemical formula $Zn(mim)_2$. Since zinc possesses a bivalent metal centre and has a tetrahedral geometry, imidazolate ligands use two coordination sites on the metal resulting in the formation of different cyclic rings. These rings are further connected via the remaining coordination sites into 3-dimensional (3D) MOFs with sodalite (SOD) topology (*66*) and a large pore diameter of 11.6 Å that is accessible through small apertures with diameters of 3.4 Å (*60, 67-70*).

In essence, coordination is enabled by deprotonation of the imidazole ligand. Imidazole is a five-membered heterocyclic compound which can be deprotonated to form an azolate anion. By doing so, each nitrogen atom can ligate to the zinc metal ion. The two nitrogen donors of the imidazole (im) ligand are oriented at an angle of 135°-145°. Within the imidazole bridging range, the octagon, nonagon, and decagon geometries requires angles 135°, 140° and 144° respectively (*66, 71*). The bridge of the imidazole ligand to zinc at an angle close to 145°

corresponds with the bridging angle of Si-O-Si that is found and preferred in many zeolites (*71*) (**Fig. 2.5**). Thus, for ZIF-8 we expect a decagon geometry.

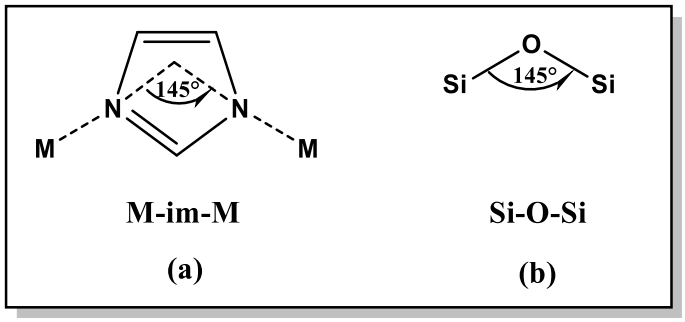

Figure 2.5: Bridging angles in (a) metal imidazole (b) zeolites.

2.5.1.2 ZIF-8 crystal structure

ZIF-8 crystals are characterised as having rhombic dodecahedral (RD), truncated rhombic dodecahedral (TRD) or cubic morphologies (*63, 64, 67, 72*)(**Fig. 2.6**). The formation of cubic ZIF-8 crystals indicate the beginning of crystal growth in the [100] facet orientation. According to Wulff's rules, the final RD morphology of ZIF-8 in its most thermodynamically stable state is determined by the slowest growing direction [110] (*63, 73*). RD shaped ZIF-8 crystals can be described as a polyhedral with twelve rhombus-shaped facets. If the vertices of such a polyhedron are cut, a TRD ZIF-8 crystal is formed. In simple terms the intermediate TRD shaped crystal may be described as a RD with square cuts in the six [100] vertices and is a consequence of incomplete crystal growth (*63, 74*).

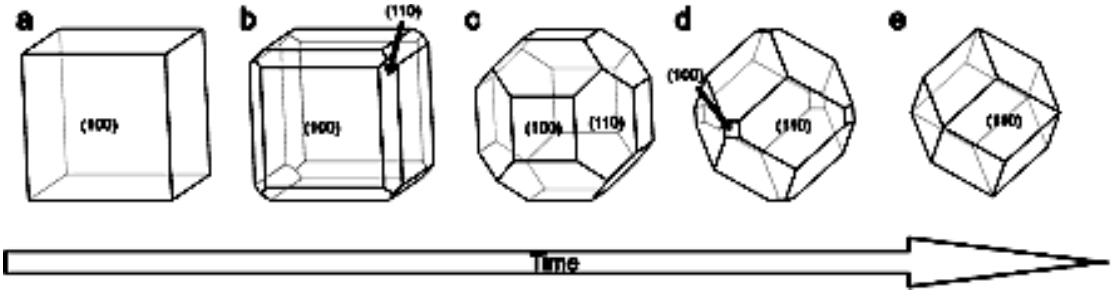

Figure 2.6: Illustration of change in ZIF-8 crystal morphology with time (a) cube (b) truncated cube (c and d) truncated rhombic dodecahedron (e) rhombic dodecahedron (*72*).

The crystal growth process may be controlled during synthesis in order to obtain a specific desired shape. This may be achieved by using capping agents, which when adsorbed on the surface of a crystalline facet do not only have an effect on the shape of the crystal but inhibits

crystal growth as well. In the case of ZIF-8, growth inhibitors also facilitate the formation of stable colloids by preventing aggregation. Intentionally hindering the growth process of ZIF-8 crystals may be useful for various applications (*63, 73*).

2.5.2 ZIF-8 synthesis

Great effort has been made in the development of synthesis procedures for ZIF-8 in high purity and in an environmentally friendly manner. The solvothermal method in different organic solvents is typically used for the synthesis of ZIF-8. Alternatively, sonochemical, microwave, mechanochemical, microfluid and dry gel synthesis may be used to prepare ZIF-8 crystals with ease, at low cost with improved yields (*62, 67, 69*). Yaghi's group first synthesized ZIF-8 using the solvothermal route with heating (140 °C) in dimethylformamide (DMF) for a period of 24 hours, with an intent of investigating the chemical and thermal stability of the framework.

While doing so, the porosity of the framework was demonstrated. A surface area of 1947 m^2/g and a and pore volume of 0.663 cm^3/g was reported. However, solvent effects were observed on introduction of an organic solid molecules in the SOD cage (*67, 71*). Apart from the solvent, recent reports have shown that there are other factors to consider during ZIF-8 synthesis that influence the size and morphology of crystals which in turn will determine the application of the MOF. Therefore, in addition to solvent effects we will highlight the effect of reactant concentration, temperature, metal source and added surfactant during ZIF-8 synthesis.

2.5.2.1 Solvent effect

DMF is one of the organic solvents that have been used in the synthesis of ZIF-8. However, the solvent can be trapped inside the aperture of the SOD cage due its large molecular size. To rectify this, DMF can be removed from the pore network through solvent exchanged. DMF can be replaced with methanol, reason being that methanol molecules have a smaller diameter than DMF. The solvent influences crystal morphology significantly because the rate of crystal growth and mass transport can be altered by the depletion and movement of ions that promote crystal growth at the crystal/solution interface. Most researchers have reported the synthesis of ZIF-8 in other organic solvents, however, organic solvents may pollute the environment and can also pose great risk resulting from their flammability and toxicity. Therefore, water is the best choice of solvent for ZIF-8 synthesis (*65, 67*).

Water has smaller molecules than the SOD cage of ZIF-8 and it also promotes a rapid depletion rate as opposed to when methanol is used which results in the formation of ZIF-8 crystals with a large size and in some cases may be aggregated (*65*). The initial report of ZIF-8 synthesis in aqueous solution was performed at room temperature and the crystals obtained exhibited poor porosity and low surface areas as compared to those synthesized in organic solvents (*75*). This suggested that amorphous compounds were formed as by-products. Eventually, Tanaka's group managed to prepare pure crystals under the same condition, but it required excess of the imidazole source which in turn will influence the crystal size of ZIF-8 in aqueous solution (*67, 76*).

2.5.2.2 Reactant concentration

Colloidal particles are formed through crystallization, however the nucleation rate determines the size of the particles formed. Rapid nucleation leads to the formation of a large number of nuclei and slows down crystal growth which in turn results in formation of small sized particles. Slow nucleation on the other hand has the opposite effects, yielding particles that are large in size. The nucleation rate is dependent on the reaction rate between the ligand and metal ions to form a coordination complex (*77*). Therefore, size control of ZIF-8 particles can be controlled by regulating the concentration of the reagents. This can be achieved in two ways (a) changing the reactant ratio by adjusting the concentration of either one of the reactants and (b) adjusting the concentration of both reactants at a constant ratio. Increasing the concentrations of both Zn^{2+} and 2-Hmim simultaneously promotes both nuclei growth and nucleation of ZIF-8, whereas increasing the concentration of either Zn^{2+} or 2-Hmim enhances ZIF-8 nucleation but hampers nuclei growth leading to the formation of small ZIF-8 particles (*61, 67*).

The use of excess Hmim can be used to explain ZIF-8 formation, reason being that Zn^{2+} is most likely to undergo hydrolysis and many other side reactions. Thus, ZIF-8 formation begins with Hmim deprotonation followed by formation of $Zn(mim)_2$. In its deprotonated form Hmim can act as a linker while in its neutral form it can act as a stabilizer. While ZIF-8 crystallization drives deprotonation of Hmim, having excess of the neutral form in solution terminates crystal growth, resulting in the formation of small ZIF-8 particles (*78, 79*).

2.5.2.3 Temperature effect

The first time Chen *et al* synthesized ZIF-8 at room temperature it took a month while Yaghi's method at 140 °C only took 24 hours. This can be partially attributed to the high temperature which has an impact on the crystallization process (*71, 80*). ZIF-8 particle size and shape can be controlled through temperature adjustments which was demonstrated by comparing two experiments, one performed at room temperature and another in an ice bath. ZIF-8 nucleation was driven by supercooling instead of supersaturation. A reduction in the reaction temperature increased supercooling which induced a big drop in Gibbs energy thus enhancing nucleation over crystal growth. Therefore, ZIF-8 crystals synthesized in the presence of ice were smaller in size compared to those synthesized at room temperature. Nuclei growth of ZIF-8 was further hindered by low reaction rate at low reaction temperature which also confirmed that nuclei growth was strongly suppressed. The purification process also influenced the particle size. Under both conditions, the particle size increased with time although ZIF-8 particles synthesized at room temperature were still larger than those synthesized in the presence of ice. This is a result of a strong centrifugal forces that bring the ZIF-8 particles together thus grow larger through further framework connections between smaller particles. Both methods did however exhibit comparable yields. Therefore, the size of ZIF-8 particles can be controlled without sacrificing yields (*61*).

The effect of reaction temperature was also investigated under heating where one reaction was carried out at 80 °C and the other at 140 °C. ZIF-8 with a RD geometry was obtained at 80 °C and a TRD geometry was observed at 140 °C. Controlling the reaction temperature alters the degree of saturation which changes the growth rate of each crystallographic face of ZIF-8. The RD resulted from a high degree of saturation which induces rapid growth on the [100] facets and delays growth on the [110] facets. The resulting RD structure at 80 °C is in accordance with Bravis' rule, which stipulates that rapid growth on the [100] facets will lead to an expansion of the slower growing [110] faces and shrinkage of the other crystallographic faces. On the other hand, lower levels of saturation most likely led to immediate growth rates of the [100], [110] and [111] crystallographic faces yielding TRD shaped ZIF-8 (*81*).

2.5.2.4 Metal source

A variety of zinc salts have be used in ZIF-8 synthesis, notwithstanding the advantages metal salts offer with respect to processability, as a metal ion source, metal salts have been utilized to manipulate the crystal size and morphology of ZIF-8 (*82*). Reactivity of the metal in solution determines the size of ZIF-8 crystal. In methanol, small sized ZIF-8 particles can be generated in the presence of $Zn(NO_3)_2$ as the metal source. This is due to relatively weak solvation of the Zn^{2+} ion in methanol which drives quick nucleation and coordination between the metal ion and ligand. Substituting $Zn(NO_3)_2$ with $Zn(CH_3COO)_2$ slows down the speed at which ZIF-8 crystals are generated drastically, resulting in the production of ZIF-8 crystals that are large in size. The strong interaction between $(CH_3COO)^-$ and Zn^{2+} paired with the weak solvation of the metal ions in methanol prohibits rapid nucleation. Hence medium sized particles can also be obtained using $Zn(CH_3COO)_2$ in methanol by limiting interaction between the solvent and the metal ion. This strategy involves mixing the metal salt and with the ligand prior to addition of the solvent. This reduces solvation time of the Zn^{2+} in solution as Hmim immediately reacts with the metal ion upon the addition of methanol (*67*).

Schejn *et al* also investigated the role of different zinc sources in ZIF-8 synthesis at room temperature and in the presence of methanol. They used $Zn(acac)_2$, $Zn(AOc)_2$, $ZnBr_2$, $Zn(ClO_4)_2$, $ZnCl_2$, ZnI_2, $(ZnNO_3)_2$ and $ZnSO_4$ as metal precursors. In their report they evaluated the relationship between crystal grown rate, size, and morphology. It was evident that crystal morphology evolves with time resulting in cubic structured crystals changing to intermediate shapes and finally to a stable rhombic dodecahedral morphology. With respect to size, using $Zn(acac)_2$, $Zn(ClO_4)_2$, $(ZnNO_3)_2$ and $ZnSO_4$ yielded nanosized crystals with sizes ranging from 50 to 200 nm. ZIF-8 crystals with sizes between 350 and 650 nm were observed when $Zn(AOc)_2$, $ZnCl_2$, and ZnI_2 were used. Lastly, micro-sized crystals were obtained with $ZnBr_2$ as a precursor. Their study also demonstrated that changes in particle size and morphology has a significant impact on adsorption properties and catalytic activity of ZIF-8, with crystals attained from $Zn(NO_3)_2$ having the highest BET surface area and unsurpassed catalytic activity in Knoevenagel and Friedlander condensation reaction models (*82*).

2.5.2.5 Effect of added surfactant

Surfactants have also been utilized for modulating the size and morphology of MOFs. They do this by acting as capping agents during the early stages of crystal growth.

Cetyltrimethylammonium bromide (CTAB) has been used for this purpose during the formation of ZIF-8 crystals in aqueous solution. It has been demonstrated that the addition of a small amount of this surfactant in an aqueous system during ZIF-8 synthesis results in a change in morphology from the typical RD shape to a TRD shape with a decrease in mean particle size. When the concentration of CTAB concentration is increased the particle size decreases from a micromitre to a nanometre range with another change in morphology, now from TRD to truncated cubes (TC). A further increase in CTAB concentration only leads in a further decrease in the particle size while the TC morphology is maintained. On the other hand, the TRD morphology in ZIF-8 particles may be maintained by controlling both the ligand and capping agent concentration which in turn tunes the particle size. Therefore, the caping effect of CTAB is attributed to competition between the surfactant and the ligand in interacting with the zinc ions (*73, 83, 84*). The surface area and pore volume of ZIF-8 crystals formed in the presence of a surfactant in aqueous media is similar to that obtained when synthesis is performed in organic solvents suggesting that the crystallinity is also maintained (*73, 84*).

In order to understand the role of the quaternary ammonium head, hydrocarbon tail and counter ion of CTAB in ZIF-8 synthesis, Pan *et al* synthesised ZIF-8 in the presence of three other surfactants, that is cetyltrimethylammonium chloride (CTAC), trimethylstearylammonium chloride (STAC) and tetrapropylammonium bromide (TPABr). Unlike CTAB, TPABr does not have a hydrocarbon tail while CTAC is similar to CTAB in that regard but contain a different anion. Similar to CTAC, the chloride ion is found in STAC, but the hydrocarbon tails of these surfactants differ. Pure ZIF-8 crystals can be obtained from all three surfactants. Using CTAC and STAC has the same effect as CTAB as these two surfactants also change both the crystal size and morphology while these properties do not change much with the use of TPABr regardless of its concentration. Thus, we can speculate that the long hydrocarbon chains are responsible for controlling the morphology and size of ZIF-8 crystal while the counter anions only changes the size of the crystals (*73*). In addition to these surfactants, tris(hydroxyethyl)aminomethane (TRIS) has been used to control the crystal morphology of ZIF-8 nanocrystals because it preferentially adsorbs on the [111] facet giving rise to octahedral shaped crystals unlike CTAB which stabilizes the [100] facet resulting in a TC morphology (*85*).

2.6 Zirconium based MOFs

In 2008, Professor Karl Peters from the Chemistry department at the University of Oslo developed a zirconium (Zr) based MOF and named it UiO-66 ($Zr_6O_4(OH)_4(CO_2)_{12}$) (*86, 87*). Isoreticular expansion of UiO-66 using elongated linkers resulted in the formation UiO-67 and UiO-68. The benzene dicarboxylate (BDC) ligand used for UiO-66 synthesis was replaced with biphenyl-dicarboxylate (BPDC) to form UiO-67, and terphenyl dicarboxylate (TPDC) to obtain UiO-68 (*88*). The UiO MOF series has not only gained interest due to its stability and porosity, but its derivatives can also be synthesized with ease at a low cost. Initially, the UiO MOF series was obtained as polycrystalline powders, and their structures were determined using PXRD (*86*). The UiO-66 derivatives have a much higher surface area, but UiO-67 is less stable in aqueous media or moisture compared to UiO-66 (*89*). This work will report on the parent compound which is discussed below.

2.6.1 UiO-66 crystal structure and properties

UiO-66 was synthesized by connecting 1,4-benzene dicarboxylate (BDC) to twelve $Zr_6O_4(OH)_4$ clusters forming a closed packed cubic structure in which the triangular faces of the Zr_6 octahedron are capped by μ_3-O and μ_3-OH groups alternatively (*87*). The robust porous material with a face centred cubic crystal structure is composed of large octahedral microporous cages which are centres to small tetrahedral cages with diameters, 11 Å and 8 Å, respectively. As seen in **Fig. 2.7** these two cages are linked through narrow triangular windows that are approximately 6 Å in diameter (*90, 91*).

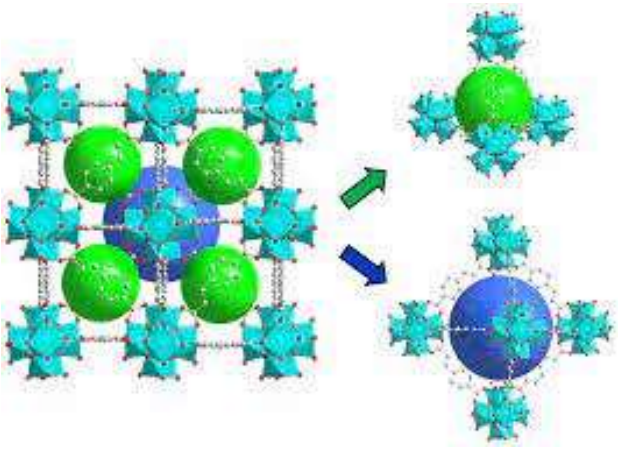

Figure 2.7: Illustration of the crystal structure of UiO-66 indicating the octahedral (blue sphere) and tetrahedral cage (green sphere) (*91*).

The MOF has a high surface area, high thermal stability with a decomposition temperature above 500 °C and also shows chemical resistance in organic solvents such as acetone, benzene, DMF and in aqueous media. The stability of the MOF is attributed to the 12-fold coordination which is the highest coordination number reported for clusters (*87, 92, 93*).

2.6.2 UiO-66 synthesis

Highly crystalline UiO-66 with a high BET surface area of approximately 1200 m^2/g was obtained when the MOF was synthesised using zirconium chloride ($ZrCl_4$) as a metal source (*90, 91*). Owing to the high porosity, and high surface area, UiO-66 can be used for several applications which can be expanded by functionalizing the MOF or forming composites using metals and nanoparticles (*89*). However, conventional synthesis of UiO-66 using zirconium chloride ($ZrCl_4$) hinders its usage as it leads to the production of hydrochloric acid (HCl) which makes it a challenge to encapsulate HCl sensitive materials such as gold nanoparticles Zirconium propoxide (Zr(O*n*Pr) can be used as an alternative to $ZrCl_4$ (*94*). Exercising control over MOF synthesis is essential in ensuring reproductivity of the physical properties of the MOF which include porosity, crystallinity, particle size and morphology. We will discuss on how the solvent, reaction time, temperature, and addition of a modulator influences some of these properties during UiO-66 synthesis.

2.6.2.1 Solvent effect

The low thermal stability of many MOFs make them unsuitable as adsorbents at high temperatures predominantly in the separation of CO_2 from flue gas. The synthesis of the UiO-66 MOF with good thermal stability allowed for its use in gas adsorption. A nanosized Zr-MOF was synthesized by Abid *et al* (*95*) and used it as a hydrogen and CO_2 adsorbent. The UiO-66 MOF with enhanced surface area and thermal stability was synthesized through the solvent-exchange activation process. The process involved immersing UiO-66 synthesised using DMF in chloroform for a few days. Following filtration and vacuum drying, the activated MOF was used for adsorption of hydrogen and CO_2 at different temperatures. The use of chloroform for solvent exchange is efficient for the removal of DMF and unreacted BDC from the MOF pores improving porosity, surface area and enhancing the gas adsorption capacity of the UiO-66.

After reporting the effect of the solvent exchange activation process in UiO-66 synthesis, Abid's group investigated the effects of ammonium hydroxide (NH_4OH) addition in the synthesis solution. The cubic morphology of Zr-MOFs was maintained with NH_4OH

modification. The NH_4OH modified Zr-MOF (Zr-MOF-NH_4) did not cause a significant change in the in the crystallite structure but the particle size of the MOF was reduced. Addition of the base increased BDC solubility and prevented the metal ion from aggregating to form large crystals. The BET surface area and pore volume of Zr-MOF-NH_4 were slightly lower compared to Zr-MOF but the thermal stability of the MOF was not sacrificed. A small reduction in gas adsorption capacity was observed with Zr-MOF-NH_4, however selectivity of the MOF towards carbon dioxide and methane was enhanced (*96*).

2.6.2.2 Reaction time

The heating temperature and time used for MOF synthesis affects the crystallization process. Many researchers have synthesized UiO-66 at 120 °C for 24 hours in DMF. Rahmawati *et al* (*97*) investigated the effect of reaction time in the solvothermal synthesis of UiO-66 at 140 °C and different time intervals. The reactions were performed at 6, 12, 24, 36, 48, 72 and 144 hours. They observed that increasing the reaction time up to 72 hours increases the weight of the crystals, thereafter weight loss of the crystal was observed.

The XRD results obtained showed that UiO-66 with good crystallinity can be formed within 6 hours of heating. Heating hours above 24 hours indicated a change in the XRD pattern and intensity. New peaks were generated indicating a phase change which were consistent with the SEM results that showed a cubic morphology after 6 hours of heating and a needle like morphology after 72 hours of heating. Although 72 hours of heating produced an optimum weight, the group concluded that running the reaction for 6 hours was the best at 140 °C as the crystallinity and morphology corresponded to those reported for standard UiO-66 (*95*).

2.6.2.3 Temperature effect

Shearer and co-workers (*98*) investigated the effect of the reaction temperature on thermal stability of UiO-66. In their study, UiO-66 was synthesized varying the temperature between 100, 160 and 220 °C for 12 hours. They reported that UiO-66 synthesized at 220 °C with a 2:1 BDC:Zr ratio as opposed to the standard 1:1 ratio yielded the best thermal stability up to 350 °C. It was concluded that the reactant ratio had no significant effect on the thermal stability of the material. Therefore, thermally stable UiO-66 with good crystallinity can be synthesized at higher temperatures within a short period of time.

Contrary to the high stability of UiO-66 synthesized at high temperatures, producing Zr-MOF with regular crystalline morphology can be a challenge. Zhao *et al* (*99*), managed to solve this problem by synthesizing UiO-66 at 50 °C. This was done in a water bath to allow crystallization to proceed under static conditions resulting in the formation of octahedral nanocrystals. The octahedral shaped crystal were about 150 - 200 nm in size. Thus, low temperature synthesis did not only afford UiO-66 with a well-defined morphology but also controlled the size of the MOF crystals without compromising the high surface area or thermal stability of the MOF.

2.6.2.4 Effect of added modulator

Zr-MOFs reported in literature have typically displayed morphologies compromising of aggregated irregular inter-grown polyhedral microcrystals, resulting from the high charge density of Zr (IV) which polarizes the Zr-O bond. Polymerization of the Zr-O bond slows down the ligand exchange reaction between Zr clusters and carboxylate ligands (*100, 101*). This has led to the formation of UiO-66 with disordered phases and low surface area, limiting its application in hydrogen adsorption. Kitagawa *et al* demonstrated a modulation approach for MOF synthesis which inspired the modulated synthesis of Zr-MOFs. Modulated synthesis refers to the regulation of the coordination equilibrium by introducing a substance with similar chemical properties as the organic ligand and competes with the ligand for coordinating to the metal ion. Modulated synthesis has proven to improve reproducibility of synthesis procedures, tune the size, morphology and crystallinity of the MOF (*101, 102*).

Monocarboxylic acids (MAs) are normally used for modulated synthesis of MOFs. Formic acid has been used as a modulator for UiO-66 synthesis, yielding UiO-66 with relatively higher crystallinity within 2 hours. The products were reproducible and larger crystals were obtained at longer reaction times. The Zr-MOF exhibited high stability in aqueous media, high thermal stability, comparable surface area and hydrogen storage capacity to literature values. A change in morphology and crystallite size was observed with an increase in the concentration of the modulator. Octahedral shaped particles around 100 nm in size were attained with 50 equivalents of formic acid while octahedral crystals with sharp edges in the range of 1-3 μm were synthesized when the concentration of the modulator was doubled (*103*). Acetic, benzoic and hydrofluoric acid have also been used as modulators for UiO-66 synthesis. Behrens' group produced single octahedral shaped crystals using benzoic acid as a modulator. The size ranged from 85 nm to 200 nm with an increase in modulator concentration (*100*). The UiO-66 crystal could be tuned from small, truncated cubes to large cuboctahedra with sizes between 150 nm

and 7 μm when hydrofluoric acid was used as a modulator. The porosity and thermostability of UiO-66 was improved on the introduction of fluorine ions (*104*).

In addition to gas storage, UiO-66 has shown promise as a material for biomedical applications due to its exceptional chemical stability and biocompatibility. Therefore, upon realising that the pore size might be controlled by varying the alkyl chain length of the organic ligand and concentration of a modulator, Wang and co-workers (*105*) developed a strategy in which dodecanoic acid and triethylamine (TEA) we used as co-modulators for controlling the size and porous structure of UiO-66. The purpose of the base was to increase the deprotonation degree of the carboxylic group on the coordinating ligand and consequently shorten the nucleation period, yielding crystals with a narrow size distribution while the acid controlled the particle size. With the aid of TEA, mesoporous UiO-66 (mesoUiO-66) was synthesized, and the crystal size was tuned within the range of 40 - 270 nm. Taking advantage of the large pore size, and the ability to accommodate a model protein of cytochrome C (Cyt c), mesoUiO-66 served as a delivery agent for the protein and regulated its release from the endosome into the cytoplasm. Evaluation of the size dependent cellular uptake showed that mesoUiO-66 with particle that are 90 nm in size could be endocytosed in living cells with high efficiency, making mesoUiO-66 a promising delivery system for membrane-impermeable biomolecules .

2.7 MOF Composites and their applications

Most MOFs are insulators or semiconductors with poor electrocatalytic activities which limits their application in electrochemistry. The poor conductivity and electrocatalytic abilities of some MOFs has allowed researchers to explore further on how to make the most of the ultrahigh surface area, high porosity, thermal and chemical stability of these MOFs which led to the development of hybrid structures. Composite formation can improve the conductivity and catalytic activity of MOFs like ZIF-8 and UiO-66 making them good candidates for electrochemical sensing, photocatalysis, drug delivery and other applications which we will discuss in the next section (*106-108*).

2.7.1 MOF composites as drug carriers

There has been a lot of progress made in the pharmaceutical industry as new drugs are being developed. This include the development of drug delivery systems which aim at improving drug efficacy, effectiveness, and safety in vivo. Drug delivery systems may come in the form of a small carriers and formulations that introduce the therapeutic drug to the body. Carrier based drug delivery systems in particular are known to protect the therapeutic molecule while improving its bioavailability, preventing biodegradation, decreasing toxicity and controlling drug plasmatic levels in the body (*109*).

Over the years drug delivery carriers such as polymeric nanoparticles, micelles, liposomes, and porous solids have been studied. With each carrier possessing its own benefits and short comings, MOFs were considered as one of the suitable candidates for drug delivery. However, for this to be possible it is required that they are non-toxic, biocompatible, and chemically stable to a certain degree . Anticancer drugs are the most popular drugs that have been loaded on MOFs and their drug releases kinetics have been studied. ZIF-8 has been used as drug a carrier. Anti-tumour drug, 6-mercaptopurine (6-MP) has been loaded inside ZIF-8 and the composite has been investigated for its drug release properties. On its own, 6-MP has a short plasma half-life and suffers from poor bioavailability. The drug delivery study of 6-MP through 6-MP@ZIF-8 composites showed that at neutral pH the drug is released after 7 days while at pH 5 it was released after 10 hours. The acidic pH mimicked the internal environment of cancer cells and it has been demonstrated that ZIF-8 decomposes in acidic pH, hence monitoring pH closely can aid in controlling decomposition of ZIF-8 resulting in the release of the drug in tumour cells without affecting the normal ones (*110*).

In cancer treatment drug delivery systems are meant to minimize the side effects of chemotherapy without causing harm to healthy cells. Owing to the attractiveness of ZIF-8 for drug encapsulation, transportation and selected pH mediated release, another antitumor agent, doxorubicin (DOXO) has been incorporated into ZIF-8 through surface adhesion and released into tumour cells upon increase in acidity of the surrounding environment. However, the DOXO-ZIF-8 composite showed lower cytotoxicity to tumour cells compared to pure doxorubicin therefore it was essential to improve the therapeutic profile of the drug. For this reason, Sharsheeva *et al* further enhanced the effect of the composite in neuroblastoma (IMR-32) cells by depositing it onto photosensible titanium dioxide nanotubes (TNTs) to accelerate

further control of the pH mediated release of DOXO using ultraviolet (UV) light. The DOXO-ZIF-8-TNT model demonstrated that the viability of tumour cells can be supressed effectively in less than an hour (*111*).

Considering the high loading capacity of ZIF-8 and magneticity of Fe_3O_4, another nanocomposite was fabricated and used as a drug carrier for controlled release of DOXO to tumour cells. The Fe_3O_4-ZIF-8 composite was detectable using magnetic resonance imaging (MRI), minimized cytotoxicity of the drug, reduced viability of hepatocellular carcinoma (HCC) cells, and also promoted tumour cell apoptosis. Thus, Fe_3O_4-ZIF-8 can be used for HCC therapy (*112*). Fe_3O_4 nanoparticles (NPs) have also been combined with UiO-66 for DOXO delivery by forming Fe_3O_4@UiO-66 core shell composites. Fabrication of these composites did not only rely on the biocompatibility of the Fe_3O_4 NPs and the compound's prevalence in MRI but also exploited the numerous metal sites, open cavities and amphiphilic property of UiO-66 which permits strong coordination between the hydroxyl groups in the drug and metal centres in UiO-66. Also, UiO-66 showed a relatively low toxicity, thus when tested in vitro and in vivo the Fe_3O_4@UiO-66 nanocomposite showed outstanding tumour size inhibition and high cancer cell mortality indicating effective drug delivery. Therefore, the composites show promise in cancer diagnosis and therapy (*113*).

2.7.2 MOF composites in photocatalysts

Immense attention has been given to the development of heterogenous catalytic systems for the degradation of photo-active pollutant molecules during water remediation. Semiconductor nanoparticles are one of the materials that have been studied extensively for this purpose. In this pool, titanium oxide (TiO_2) was the most preferred because of its low production cost, flat band structure, ease to apply in ambient to harsh conditions and its non-toxicity. The basis of the photocatalytic mechanism of TiO_2 involves the generation of an electron-hole pair in the conduction and valence band of the material which interact through columbic forces and produce excitons. These excitons catalyse the degradation of pollutants such as dyes by dissociation. This is possible in the presence of UV radiation which provides enough energy for the process. This is not the case in the presence of visible light as it does not provide enough energy for exciton generation, instead in aqueous solution TiO_2 NPs produce reactive oxidative species (ROS) from dissolved and aerial oxygen and the exciton energy is transferred to these species.

ROS further oxidise dyes and pollutant molecules in order to degrade them and this mostly results in mineralization, or dye molecules are degraded when the hole reacts directly with the dye. In an attempt to solve this problem, TiO_2 NPs have been encapsulated in different MOFs which resulted in partial loss of activity in the NPs and chemical instability of some MOFs. ZIF-8, however, was found to be a good encapsulation agent because of its thermal and chemical stability therefore Chandra and colleagues fabricated a TiO_2@ZIF-8 composite. Combining the two resulted in enhanced photocatalytic degradation of dyes in visible light and the composite still retained high catalytic efficiency after several cycles (*114*).

The dependence of most photocatalysts on UV radiation has limited their application. Emerging research has introduced a new generation of catalysts that are sensitive to visible light such as molybdenum disulphide (MoS_2) and graphitic carbon nitride (g-C_3N_4). g-C_3N_4 is an organic semiconductor with high chemical and thermal stability that is synthesised from cheap precursors. It is suitable for a variety of photocatalytic application which are limited by high exciton recombination and low surface area of the material. To correct this, a strategy that combines adsorption and photocatalysis was developed. Taking advantage of the high surface area of ZIF-8, g-C_3N_4 was anchored on ZIF-8 forming a photo-generable bifunctional composite for removal of harmful water contaminants without the requirement of a secondary remediation process. The composite exhibited a high adsorption capacity for tetracycline antibiotics through π-π and electrostatic interactions between the aromatic groups of the composite and the pollutant antibiotic. Subsequently, exposure to sunlight degraded over 90 % of the antibiotic within an hour. Thus, this strategy offers an environmentally benign and greener method for efficient degradation of water contaminants (*115*). Efficient tetracycline removal was also observed using recyclable cobalt-doped UiO-66 NPs. Similarly, the enhanced adsorption capacity is attributed to π-π and electrostatic interactions between the MOF composite and antibiotic. On the other hand, cobalt (Co) was responsible for enhanced visible light adsorption and facilitating electron transfer which enhanced photocatalytic performance (*116*).

Photo-active ZIF-8 composites have also been used to try and solve other environmental problems such as global warming caused by excessive CO_2 emission. Due to a remarkable optical response and suitable band structures, cadmium sulphide (CdS) based photocatalysts have been investigate immensely but these suffer from photocorrosion. On the other hand, ZIF-8 has been used for CO_2 capture and storage which is attributed to its high porosity and surface

area. Combining CdS and ZIF-8 to form a core-shell composite (CdS/ZIF-8) enhanced the photostability of CdS. Composite formation also improved the CdS adsorption capacity for CO_2 without interfering with its light harvesting property. As a photocatalyst, CdS/ZIF-8 showed elevated photostability, enhanced selectivity and improved photocatalytic efficiency for reduction of CO_2 to CO compared to the unmodified CdS photocatalyst (*117*). CdS has also been incorporated into UiO-66 and the potential of the resulting composite as a photocatalyst for water splitting was demonstrated as CdS/UiO-66 showed superior hydrogen evolution activity when irradiated under visible light compared to both materials individually. Enhanced hydrogen production with the hybrid material could be ascribed to efficient interfacial charge transfer from the CdS to UiO-66 though which photoactivity efficiency trumps photogenerated electron-hole pair recombination (*118*).

2.7.3 MOF composites as sensors

Rapid, sensitive, and accurate detection of molecules such as rutin is important in clinical analysis. Rutin is a therapeutic medicine that can dilute blood, lower blood pressure and lower capillary permeability. For its detection, an electrochemical sensor was fabricated by modifying a GCE with a methylene blue (MB) loaded ZIF-8 immobilized on reduced GO composite (MB@ZIF-8/RGO). The sensor based on this composite revealed superior sensitivity in the detection of rutin and this could be attributed to the high surface area of ZIF-8 and synergetic effects of RGO and MB as they both possess strong conductive and catalytic properties (*119*).

Dopamine (DA) is also important in clinical diagnostics. A deficiency of this neurotransmitter may result in neurological disorders while elevated levels of DA may lead to a rise in the risk of depression. A series of methods have been used for the detection of DA and amongst them electrochemical methods are the most preferred with advantages including simple instrumentation, rapid response, superior sensitivity, and selectivity. Lu *et al* reported successful synthesis of ZIF-8 embedded with gold nanoparticles (Au@ZIF-8) composites at GCE for the detection of DA. The modified GCE electrode exhibited good selectivity, high sensitivity, low limit of detection (LOD), reproductivity and stability for DA detection as a result of the high ZIF-8 surface area and high catalytical activity of Au NPs which could accelerate electron transfer (*107*). Zheng *et al* also detected DA using an electrochemical sensor fabricated by modifying GCE with a graphene (G) doped ZIF-8 composite (G-ZIF-8/GCE).

The sensor showed high sensitivity to DA owing to the high surface area of ZIF-8 and conductivity of graphene (*106*).

Quantum dots (QDs) are one of the inorganic materials that have been incorporated into ZIF-8 for sensing. Attractive properties of QDs such as low toxicity, quantum size effect, high quantum efficiency, water solubility, narrow and symmetric fluorescence emission spectra among many have made ZnS QDs an excellent choice for fluorescence sensing. Water soluble Mn^{2+} doped ZnS QDs have been used successfully for bioanalysis. Contrary to that, after precipitation and drying QDs may agglomerate. ZIF-8 can serve as a carrier which reduces agglomeration as well as an inexpensive fluorescence ion detecting tool. Cobalt (II) is one of metal ions that play an important role in the human body. It is part of vitamin B_{12}, which stimulates the production of the bone marrow, formation of haemoglobin and promotes the increase in the number of red blood cells in humans. Although this is the case, the body only requires a certain amount of this metallic ion as excessive amounts in the blood may cause allergies, lung, and neurodegenerative diseases. Hence an accurate detection system of cobalt(II) in the body is necessary and for this purpose a Mn^{2+} doped ZnS QDs/ZIF-8 fluorescent probe was developed. The probe displayed outstanding fluorescence properties for the detection of cobalt (II). It also showed exceptional detection ability towards potassium dichromate, a carcinogenic pollutant that is lethal to plants and aquatic life which may be found in wastewater from the manufacturing industry (*120*).

The magnetic Fe_3O_4-ZIF-8 composite mentioned earlier is not only useful in drug delivery systems but may be utilized for water remediation as well. This is applicable for elimination of heavy metal ions like arsenic (As^{3+}) from water. As(III) is extremely toxic to human beings and adsorption onto porous solid material has been considered as an easy, cost effective and highly effective approach for its removal from water. Unfortunately, most porous materials had low capacity or showed dissatisfactory kinetics for As(III) which required a complicated procedure for oxidation of As(III) to less toxic As(IV). The Fe_3O_4-ZIF-8 composite indicated a strong affinity for As(III) in aqueous solution and a high removal efficiency at broad pH range. The study also indicated that ordinary anions would not hamper adsorption of As(III) with the exception of phosphate and carbonate which may compete with As(III) for adsorption sites. Considering this, the composite was deemed as a good candidate for removal of As(III) in aqueous solution which can be separated from the composite by magnetism (*121*). Similarly, UiO-66 was decorated with Fe_3O_4 and the Fe_3O_4@UiO-66 adsorbent showed a higher

adsorption capacity for As(III) than that of Fe_3O_4 due to the high porosity and increase in the number of active sites on the composite (*122*).

Eutrophication is of great concern in water treatment and phosphorus (P) is an important factor for this process. Phosphate may be the principal source of phosphorus but phosphite also supports the growth of algae found in water bodies and can also be converted to phosphate though different pathways. Majority of researchers have therefore focused on the development of sensors for the detection of phosphate with a few reports on phosphite detection due to interference of phosphate and other P species that may be found in contaminated water. Yang *et al* reported on the development of an electrochemical sensor for phosphite detection in the presence of other P species by modifying a GCE with UiO-66/GO composites. Although, the potential of UiO-66 as an electrochemical sensor for P has been reported, its functionality as an electrode material for P detection is limited. Therefore, to enhance P adsorption, UiO-66 was coupled with graphene oxide (GO) because it has a high surface area, good catalytic performance, high electron conductivity and ion absorption. The UiO-66/GO/GCE displayed a wide detection range and outperformed UIO-66/GCE, GO/GCE and palladium film electrochemical sensors for phosphite detection in the presence of unavoidable interferences from phosphate (*123*).

Organophosphorus pesticides (OPs) in the environment are not only toxic to aquatic life and plants but to humans as well and exposure to them may lead to fatalities. Therefore, it was necessary to functionalize UiO-66/GO/GCE with a compound with high affinity for phosphate such as TiO_2 (T). The TGO@UiO-66/GCE sensor revealed a fast response, wide linear detection range with low LOD, satisfactory stability and reproducibility in detecting chlorpyrifos and paraoxon which are two of the most dangerous OPs used in households and crop farming (*124*). This has motivated us to fabricate phthalocyanine-ZIF-8 and phthalocyanine-UiO-66 composites which will be used for the development of sensors for the detection of other toxic environmental contaminants.

2.8 Phthalocyanines

2.8.1 Origin, properties, and applications

Phthalocyanines (Pcs) are a class of macrocyclic organic compounds. Braun and Techrniac accidentally discovered these compounds in 1907, as a blue substance resulting from heating

o-cyanobenzamide (*125-128*). In 1928, they were obtained synthetically at the Grangemouth works of Scottish Dyes Ltd, as a by-product, during phthalimide preparation using ammonia and phthalic anhydride as precursors (*129, 130*). Professor Linstead however, was the first to characterize the structural and chemical properties of phthalocyanine in 1933 (*126, 130*). Due to structural similarity to naturally occurring macrocyclic porphyrins (**Fig. 2.8**), phthalocyanines became second-generation photosensitizers based on the assumption that they behaved like porphyrins. Apart from being cyclic, porphyrins and phthalocyanines adhere to Huckel's rule of aromaticity as they are both planar, conjugated, with an 18-π electron system (*126, 127, 129, 131, 132*). Phthalocyanines may be distinguished from porphyrins which have four π-fused isoindole units (*129*). The macrocyclic ring in phthalocyanines is di-anionic (Pc^{-2}) and can form a metal phthalocyanine complex through the introduction of suitable metal ion inside the ring. Thus, Pcs exists as metal-free phthalocyanines (H_2Pcs) and metallophthalocyanines (MPcs) (*133*).

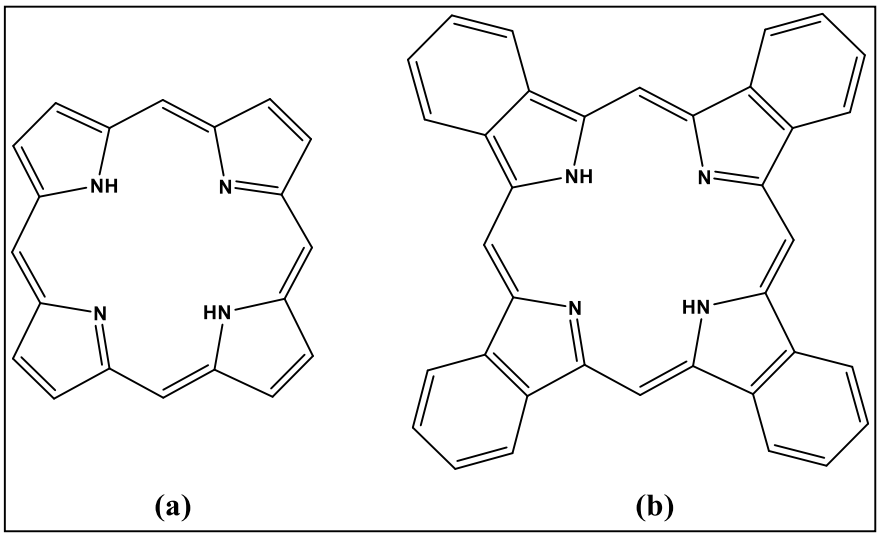

Figure 2.8: Structure of (a) Porphyrin and (b) Phthalocyanine.

Owing to their structure, phthalocyanines possess outstanding properties. These include redox versatility, high absorption coefficients, chemical and thermal stability (*127, 132, 134*). Due to their remarkable properties, there has been an increase interest in the use of phthalocyanines in different areas such as gas sensing (*135*), non-linear optics (*136*), photocatalysis (*137*), semiconductors (*138*), photodynamic therapy (*139*), and photovoltaic cells (*140*). The type of application for phthalocyanines and its derivatives is however dependent on the metal ion introduced into the cavity of the Pc ring and the functional groups introduced onto the non-

peripheral (α) and peripheral (β) positions of the Pc (**Fig. 2.9**). This is because these factors influence the chemical and physical behaviour of the compounds (*133, 141*).

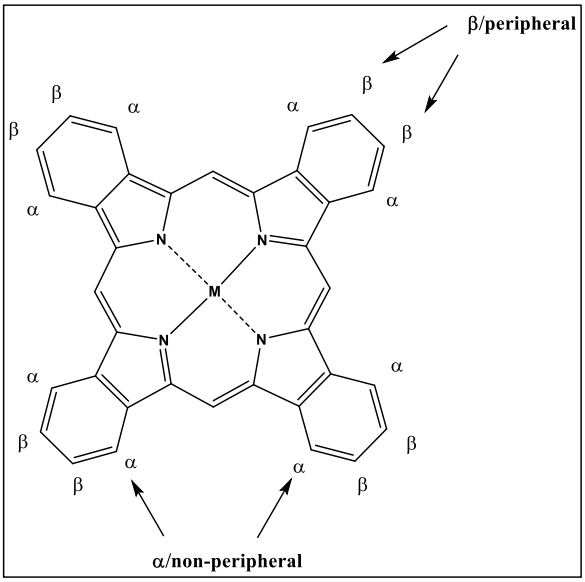

Figure 2.9: Nomenclature of positions in the phthalocyanine core. M being a metal.

Although phthalocyanines have received a lot of attention, they suffer from significant disadvantages. The first being low solubility in common organic solvents and aqueous media (*126, 127, 129*). Introducing bulky or long chain substituents in the peripheral position of Pcs can enhance their solubility in organic solvents. These include alkoxy and alkylthio groups. In aqueous solution, the solubility of Pcs may be improved by the addition of quaternized ammonium groups, carboxylic acid and sulfo groups in the β position of Pcs (*126, 127, 129, 131*).

2.8.2 Phthalocyanine synthesis

Phthalocyanine can be prepared from different precursors which include *o*-dibromobenzene, *o*-cyanobenzamide, phthalic acid and its derivative, which are phthalic anhydride, phthalimide, benzenedicarboxamide and phthalonitrile (**Scheme 2.1**). While anhydrides are the most affordable option, nitriles are the most popular choice as they give high yields (*142*).

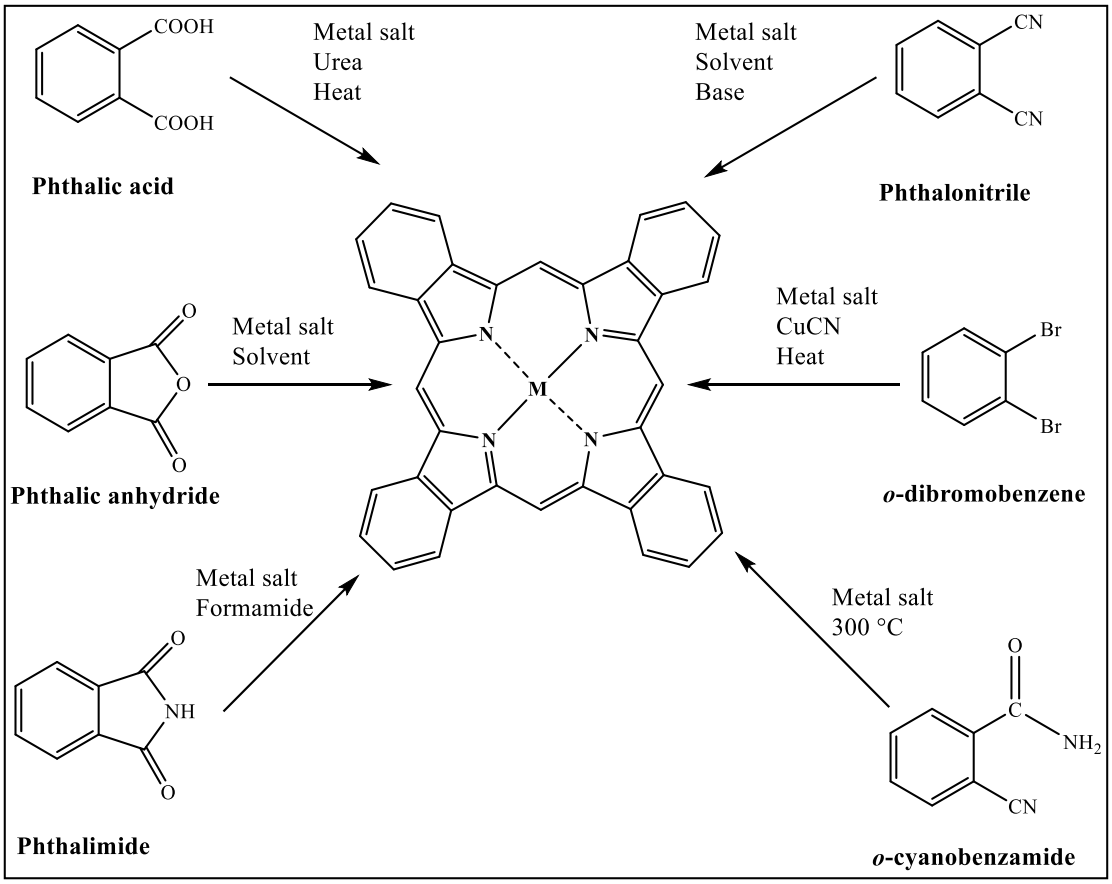

Scheme 2.1: Synthetic routes of MPcs from different precursors.

Substituted metal free or metalated phthalocyanines may be synthesised through electrophilic aromatic substitution reactions and cycloaddition reactions of an already existing phthalocyanine core. An alternative may be through cyclotetramerization of mono substituted phthalocyanine precursors, a method developed by Linstead in the 1930s. This leads to the formation of tetrasubstituted phthalocyanine that exist as regioisomers of D_{4h}, C_{4h}, C_{2v} and C_s symmetry, while the cyclization of disubstituted precursors results in the formation of octasubstituted phthalocyanine as a single isomer of D_{4h} or C_{4v} symmetry (*142-144*).

Octasubstituted phthalocyanines are usually less soluble than their corresponding tetrasubstituted phthalocyanines which may be attributed to the formation of isomers and the high dipole moment in tetrasubstituted phthalocyanines that results from the unsymmetrical arrangement of substituents at the periphery (*143, 145*). Octasubstituted phthalocyanines are however simpler to purify using chromatographic methods as they exist as a single isomer as opposed to tetrasubstituted phthalocyanines. Soxhlet extraction may also be used for the purification of phthalocyanines (*144*).

Preparation of substituted phthalocyanines that are soluble in most organic solvents requires an inert atmosphere and a high boiling point solvent. The presence of a metal salt drives the formation of a metallophthalocyanine, regardless of the precursor (*128, 131*). Where phthalic anhydride is used as a precursor, urea is used as the nitrogen source while ammonium molybdate catalyses the reaction (*128, 146*). The formation of a metal free phthalocyanines from phthalonitriles however, requires the presence of lithium metal or a nitrogen donor base such as 1,8-diazabicyclo[5.4.0]undec-7-ene (DBU) which also acts a catalyst (*127, 131, 133, 143*).

2.8.3 Ultraviolet-visible spectroscopy of phthalocyanines

Several techniques can be employed for the characterization of phthalocyanines. These include Fourier transform infrared (FTIR) spectroscopy, nuclear magnet resonance (NMR) and Ultraviolet-visible (UV/vis) spectroscopy, among others. UV-vis spectroscopy is significant for understanding the electronic properties of phthalocyanines. The most probable electronic transition observed on the absorption spectra occurs between the highest occupied molecular orbital (HOMO) and the lowest unoccupied molecular orbital (LUMO) (*147*).

Phthalocyanines are characterised by two absorption bands in the visible region, known as the Q band and B or Soret band. These are due to π-π^* transitions between the HOMO and the LUMO energy levels. The Soret band arises from transitions between the two a_{2u} (π) and b_{2u} (π) HOMOs to the doubly degenerate e_g (π^*) LUMO. The Q band is a result of an electronic transition involving the a_{1u} (π) HOMO and the π^* (e_g) LUMO (*133, 148*) (**Fig. 2.10**).

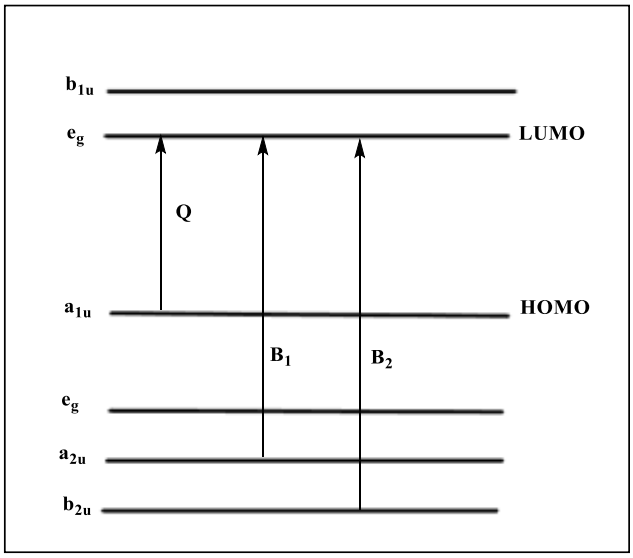

Figure 2.10: Molecular orbital diagram showing electronical transitions that results in the characteristic B and Q band in phthalocyanines.

The more intense band which is the Q band may be observed between 600-750 nm, while the B band appears between 300-400 nm on an absorption spectrum (*131*, *149*). As seen in **Fig. 2.11** MPcs show a single Q-band which depicts D_{4h} symmetry of the complexes and metal free (unmetalated) Pcs show a split Q-band which is due to D_{2h} symmetry (*127*, *131*, *143*).

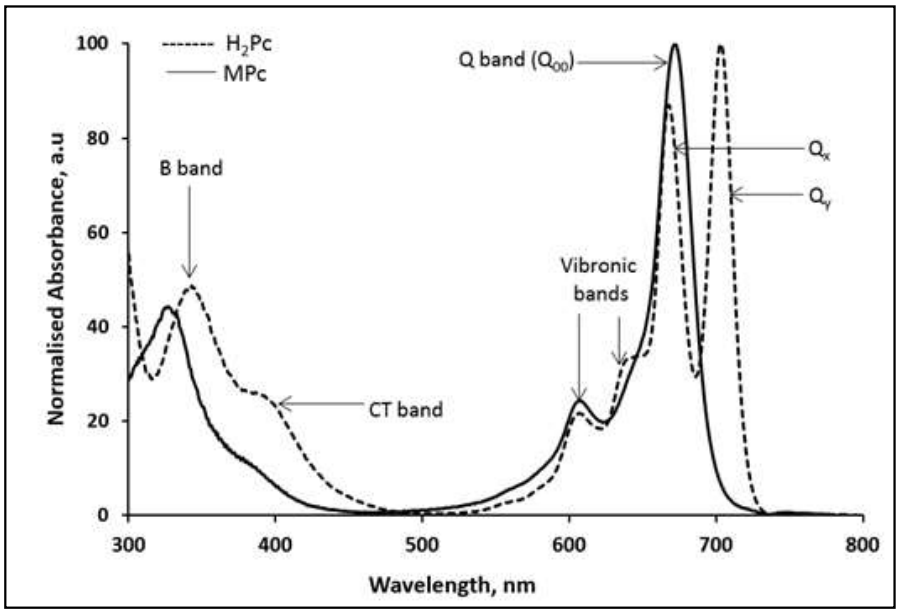

Figure 2.11: Absorption spectra of unmetalated and metalated phthalocyanine showing characteristic phthalocyanine absorption bands.

The absorption spectra of substituted metalated phthalocyanines usually show two effects on the Q band that being either a red (bathochromic) or blue (hypsochromic) shift. The latter may result from the presence of electron withdrawing substituents and the former from substituting Pcs with electron donating groups. The red shift may also be attributed to substituents that enhance the delocalization of π-electrons in a Pc molecule (*128, 149, 150*). An increase in the extent of conjugation causes the electronic levels to move close together, decreasing the energy required to produce a transition from the HOMO to the LUMO. Thus, light of longer wavelength is absorbed (*147*). In addition to that, the position of the substituent in the macrocycle also influences the shift in the Q band. Therefore, substitution at the less crowded α-position does not only reduce aggregation tendencies but also cause a red shift (*145*).

2.8.4 Electrocatalytic activity of metallophthalocyanines

MPcs have been investigated extensively as electrocatalysts for many reactions. The ability of MPc complexes to undergo rapid redox reactions and retain a stable structure during electrocatalysis qualifies them as good candidates for the development of stable, sensitive, and selective sensors. Earlier studies on the electrocatalytic activity of Pc complexes were mostly focused on the oxygen reduction reaction (ORR) for the production of low cost fuel cells with the aim of replacing the existing platinum electrodes (*151, 152*).

Also, the catalytic activity of the complexes can be defined in terms of more definite parameters. These include chemical and physical properties, chemical structures and identification of reactive metal centres which provide interesting theoretical and experimental models. In most fuel cells, electro-reduction of oxygen occurs at the cathode. The reaction involves the complete reduction of oxygen into water through a transfer of four electrons and proceeds via high energy intermediate which slow down the overall reaction. The reaction may however stop after the transfer of two electrons resulting in the formation of hydrogen peroxide. This is observed on most electrode material and is likely a repercussion of the high stability of the O-O bond. The reaction may reach completion through the use of non-noble metal catalysts (*153*).

Modification of electrodes with MPcs influences the potential and current at which the electrode and analyte interact during an electrochemical reaction. A good electrocatalyst is expected to lower the potential that drives redox reactions and increase the selectivity towards

a target analyte with respect to the unmodified electrodes. Catalytic activity of MPc modified electrodes depend on the nature of the metal centre and ring based processes (*151, 152*). Redox inactive M(II) metals behave similar to unmetalated phthalocyanines during redox reaction, the only difference being the potentials corresponding to electron transfer reactions (*151*).

The peak potentials of MPcs with redox inactive metals shift towards negative potential as a result of the small effective nuclear charge of the M(II) ions as opposed to having the H^+ ion in the core of the Pc ring. Redox inactive metal centres with +2 oxidation states such as Ni(II), Cu(II), Zn(II) and Pb(II) are generally preferred for the formation of MPc but the catalytic activity of complexes with redox inactive metal centres may be attributed to the Pc ring which is not the case for MPc complexes with redox active ions in the Pc core. The redox activity of MPc complexes with redox active ion in the Pc core is dependent on whether the d-orbital of the metal ion located between the HOMO and LUMO of the Pc ring is empty or occupied. The presence of empty d-orbitals of the metal ion results in reduction of the metal ion prior to the Pc ring while when occupied d-orbitals of the metal ion are found between the HOMO and LUMO of the Pc ring, oxidation of the metal ion precedes that of the Pc ring. Apart from undergoing redox reaction, MPc complexes with redox active metal centres can further partake in electron transfer reactions (*151*).

2.8.5 Optimization of metallophthalocyanines redox activity

Several authors have reported that there is a correlation between the catalytic activity of MPc and their redox potential. Reason being that the activation energy in electrochemical reaction is lowered in the presence of MPcs as they provide sites for molecular interactions. The redox potential of MPc does not only lower the activation energy of the reaction but also provides free energy required for the reaction to proceed. Therefore, it has been suggested that tuning the redox potential is a good strategy for optimizing the catalytic activity of MPcs in electrochemical reactions when they are attached on electrode surfaces (*154*).

The nature of a metal has an effect on the redox behaviour of Pcs, with cobalt derivatives giving excellent results for the oxidation of thiols and the reduction of corresponding disulphides. For example, during the reduction of 2-mercaptodisulfide, catalytic activity is improved as the Co(II)/Co(I) couple becomes more negative (*155*). On the other hand, a strong interaction is expected to occur between the active site and the sulphur atom prior to or during electron transfer when MPc are used for oxidation of thiols. Thus, the reaction can be regarded as an

inner sphere reaction. In cases where the interaction is too strong, the species adsorbed on the MPc modified electrode can block the active sites, inhibiting the catalytic process (*155, 156*).

Substituents on the Pc ligands can also influence the redox properties of MPc complexes. For examples, the attachment of an electron donating groups on the Pc ring makes the complex easier to oxidize, while the presence of electron withdrawing groups makes it easier to reduce the complex. In comparison to unsubstituted CoPc complexes, a less positive potential can be observed for complexes substituted with electron donating groups and a more positive potential can be observed for complexes substituted with electron withdrawing groups. It has also been demonstrated that the redox potential of MPcs is dependent on the electrolyte and pH of the buffer solution. For example, electrocatalytic oxidation of cysteine by CoPc complexes in acidic media is associated with the Co(III)/Co(II) couple and the Co(II)/Co(I) couple in basic media. In basic solution, the Co(II)/Co(I) couple shifts to more negative potential while the Co(III)/Co(II) couple shifts to more positive potential values in acidic media (*157*).

2.8.6 Electrode modification using metallophthalocyanines

MPc based electrochemical sensors can be developed by anchoring of the complexes on the surface of working electrodes. This can be achieved through different approaches, the first one being adsorption. Adsorption can be achieved by either dipping an electrode in a solution of MPc and drying (dip-dry) or by placing a few droplets of the solution on the surface of electrode, allowing it to dry and rinsing off the non-adsorbed species with a suitable solvent (drop-dry). Similarly, spin coating may be employed if films are desired, whereby droplets of MPc are placed on the surface of a rotating electrode. MPcs may also be immobilized on electrode surfaces by binding graphite powder and the metal complex together. The resulting paste can be packed to fabricate a working electrode known as the modified carbon paste electrode (CPE). Another approach for modifying electrodes with MPcs is through self-assembled monolayers (SAMs). SAMs can be formed by assembling thiol-substituted Pcs onto substrates such as a gold electrode. In addition to all these methods, electropolymerized films of macrocyclic complexes such as MPcs may be formed on conductive substrates. Cyclic voltammetry (CV) can be used for electrochemical reduction or oxidation of polymerizable groups present on the complex or by integrating them into other polymers (*151, 152*).

The most widely used electrodes and support materials used in electroanalytical chemistry are carbon-based. Reason being that carbon materials have robust mechanical strength, high

electrical conductivity, and good chemical stability. The ability of MPcs to strongly adsorb on carbon materials make them suitable for modification of conventional electrodes like GCE and the preparation of composites for electrochemical sensing. The most commonly used carbon materials combined with MPcs for this purpose are graphite, graphene oxide and carbon nanotubes. Interaction between the two materials normally happens via non-covalent interaction, primarily π-π stacking. Covalent bonds are possible in the case that supports are functionalized with specific functional groups which further react with Pcs. Different methods can be used for characterization of electrodes modified using phthalocyanine (*151*).

2.8.7 Techniques for characterization of electrodes modified with phthalocyanines

Microscopy, spectroscopy, and electrochemical methods such as atomic force microscopy (AFM), X-ray photoelectron spectroscopy (XPS) and cyclic voltammetry (CV) can be used for characterization of modified electrodes. These methods provide information on the effectiveness of the modification, properties, and integrity of the surface layer. CV has prevailed as an electrochemical method for studying the surface chemistry of MPc modified electrodes. Surface coverage (Γ) of the modified electrode can be determined using equations 1 and 2:

$$I_p = n^2F^2\Gamma Av/4RT \quad \text{.....1}$$

$$Q = nFA\Gamma \quad \text{.....2}$$

where I_p is the peak current, n is the number of electrons transferred during the redox reaction, F is Faraday's constant, A is the surface area of the electrode, v is the scan rate, R is the gas constant, T is the temperature and Q is the total charge. CV also allows determination of the diffusion coefficient (D) and concentration (C) of the electroactive species in solution which can be described using the Randles-Sevcik equation (*151*):

$$I_p = (2.69 \times 10^5)n^{3/2}ACD^{1/2}v^{1/2} \quad \text{.....3}$$

In this study cyclic voltammetry was employed for determination of electroactive molecules in solution. This technique is discussed briefly in the next section.

2.9 Cyclic voltammetry (CV)

Cyclic voltammetry and linear sweep voltammetry were first reported in 1938 as techniques in which a large potential change is imposed in a system. In 1948, Randles and Sevcik described CV theoretically as a technique in which two predetermined limits are chosen, and the potential is swept back and forth between these two points for one or more cycles and the current is monitored concurrently (*158*). The potential of the working electrode changes linearly with time from an initial potential (E_i) where no redox reaction occurs to potentials where the analyte of interest is either reduced or oxidised until the maximum limit also known as the switching potential (E_f) is reached and the scan is reversed. Reactions of intermediates and products formed during the forward scan can often be detected during the reserve scan. CV measurements are recorded in the presence of a supporting electrolyte which suppresses migration of charged reactants and products (*159-161*).

Electrochemical reactions occur at the working electrode like the GCE, and the potential of this electrode is measured against a reference electrode such as the silver/silver chloride (Ag|AgCl) electrode and the saturated calomel electrode (SCE). Platinum wire is normally used as the counter electrode to complete the circuit and the inertness of the metal permits flow of current without causing any chemical changes which may alter the experimental results of the system being studied (*159*). There are several important parameters that are used for characterization of a cyclic voltammogram. These are the anodic peak and cathodic peak. The anodic peak indicates the anodic potential (E_{pa}) and current (I_{pa}) while the cathodic peak indicate the cathodic potential (E_{pc}) and current (I_{pc}). **Fig. 2.12** indicates that the cathodic peak results from the reduction of species in solution as the potential is swept to more negative values while the anodic peak is observed upon oxidation of species in solution as the potential is swept to more positive values (*160*). Pcs have been used to form Pc-MOFs for sensing applications using voltammetry.

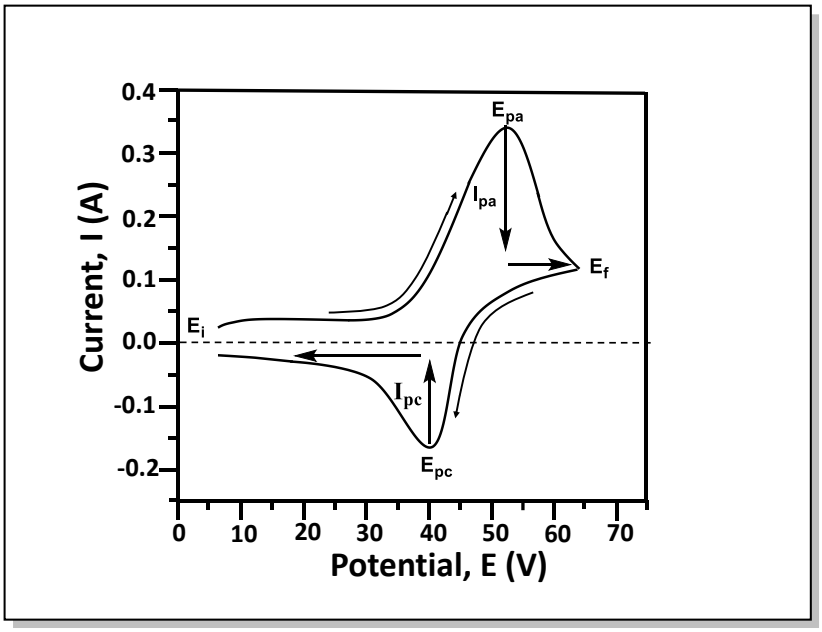

Figure 2.12: A typical cyclic voltammogram.

2.10 Phthalocyanine based MOFs and composites

2.10.1 Pc-MOFs

MOF-IP was the first microporous Pc-based MOF to be reported about a decade ago. It was designed with the hope of obtaining well defined microporous hydrogen storage material with strong hydrogen physisorption. Theoretical studies had shown that hydrogen binds strongly with aromatic compounds, therefore Pcs had a potential as hydrogen storage materials. Designing a Pc-based hydrogen storage systems did not only rely on the aromatic system of Pc but also on increasing the number of available adsorption sites by introducing more electronegative atoms and strong hydrogen binding clusters using ions such as Zn^{2+} to form the MOF. It is for that reason that MOF-IP was designed from a ZnPc with nitrogen rich substituents at its peripheral. Physisorption studies of the Pc-based hydrogen system displayed the capability of using the Pc-based MOF as a material with improved hydrogen storage. It was anticipated that structure optimization of MOF-IP could enhance its hydrogen uptake, following which MOF-IP analogs were investigated (*162*).

Two-dimensional (2D) MOFs with outstanding electrical conductivity have attracted attention as potential electrode material in lithium batteries (LIBs) which were mostly dependent on 3D nanoporous materials. Like in 3D porous structures, it was proposed that the porosity of 2D

MOFs could also facilitate ion transport and prevent deterioration that may results from the insertion of lithium ions. Therefore, a conductive 2D MOF based on Cu-CuPc was synthesized by bridging tetracatechol copper phthalocyanine (CuPcOH) ligands to Cu^{2+} ions in a square planar geometry. Pc was chosen as the bridging ligand because it possesses redox activity and good carrier transport ability due to its large conjugated system. On the other hand, the ability of catechol derivatives to form square planar complexes with metal ions displays redox activity which stem from reversible interconversions between catechol, semiquinone, and quinone forms. Thus, the use of a Pc-based framework with electrical conductivity and redox activity as a LIB cathode resulted in the formation of LIBs with large charge or discharge capacity and high stability (*163*). A 2D NiPc-MOF was also studied and similarly, NiPc acted as an electrocatalytic active site in addition to its use as a linker to form the framework. The MOF catalyst showed remarkable durability and good OER performance under alkaline conditions which may facilitate the development of conjugated conductive MOFs for energy applications (*164*). Not many Pc-based MOFs have been reported, but Pcs have been used to form composites with other MOFs (Pc@MOF).

2.10.2 Pc@MOF composites

UiO-66 (Zr) showed potential as a photocatalyst for dye degradation when incorporated with Ag_2CO_3 (*165*). Unfortunately when compared to commercial standards and inorganic photocatalysts, the MOF failed to achieve good photocatalytic activity on its own due to limited visible light absorption (*166, 167*). Taking advantage of the wide visible light possessed by semiconductor materials, Liang *et al* used zinc tetracarboxy phthalocyanine (ZnTPc) as a photosensitizer to improve photocatalytic activity of UiO-66 (Zr) and its analogue UiO-66 (NH_2). However, due to its high conjugation, ZnTPc suffers from aggregation, which the high surface area and porosity of MOFs confine, thus maximizing active sites for photocatalysis. The composites were used for methylene blue degradation and ZnTPc/UiO-66 (NH_2) exhibited superior photocatalytic activity compared to ZnTCPc/UiO-66 (Zr). Unlike the physical interaction that occurs when the impregnation method is used to form ZnTCPc/UiO-66 (Zr), ZnTCPc/UiO-66 (NH_2) was obtained via a covalent amide bond between the MOF and phthalocyanine which promoted efficient separation of generated electron-hole pairs and charge transfer when the composite was exposed to visible light (*168*).

Monama *et al* also reported on the development of a MPc@MOF composites. In their work, a CuPc@MOF composite was synthesized in order to modify and improve the catalytic activity of an electrode towards HER. Platinum based electrocatalyst are common and highly efficient electrocatalysts in HER, but their application is restricted by the scarcity of the metal and it high cost. HER predominately occurs on the surface of the electrocatalyst and enhanced reactivity is dependent on the size, shape, interface, and composition of the material used for the reaction. Amongst many materials, unique MOF structures hold great potential as multifunctional materials for HER. However, when applied as materials for HER, MOFs suffer from moisture instability, hydrogen embrittlement and poor hydrogen physisorption at ambient conditions. This can be improved by reducing the pore size which introduces open metal sites. Hydrogen uptake can also be enhanced through the hydrogen spill over effect which can be achieved using metal embedded MOFs. Palladium (Pd) is one of the metals used in this phenomenon due to its high affinity for hydrogen. The spillover mechanism using Pd@MOF is affected by many factors unfortunately, thus doping the MOF with MPc can improve and generate new functionalities on the building blocks which results from the ability of the Pc to be stabilized in the formed hybrid structure while substrates are adsorbed onto the pores. In addition, active metal sites for catalysis can be easily realized by tuning the peripheral environments of the Pcs. Therefore, Pd@CuPc/MOF composites were developed and they displayed exceptional structural stability, thermal stability and electrocatalytic activity for HER in acidic medium (*169*). Monama *et al* also synthesized a CuPc@HKUST-1 composite using CuPc and undoped Cu-MOF (HKUST-1). The undoped composite did not depend on the spillover effect for enhanced hydrogen uptake but compared to the use of the HKUST-1 alone in HER, the presence of CuPc within the composite showed improved catalytic performance (*170*). Tetranitro substituted Pc was also used for the same purpose under acidic conditions (*171*). In this work we will focus on the application of Pc@MOF composites in electrochemical sensing.

2.10.3 Pc-MOF and Pc@MOF composites as electrochemical sensors

Research on the applications of Pc@MOFs composites is still in its infancy. However, to date there have been some hybrid materials used for LIBs, photocatalysis, ORR, OER, HER and electrochemical sensing. Therefore, this section will briefly highlight on what has been reported on the use of Pc@MOF composites in electrochemical sensing.

Several analytical techniques have been used for monitoring unwanted chemical molecules in the environment. These include chromatography, spectrometry, and capillary electrophoresis. Despite the high degree of accuracy and good selectivity, these techniques are costly, time consuming, requires more operational skills and complex sample treatment prior to analysis. Thus, the electrochemical approach has received more attention in recent years. Vanillin, commonly known as a food preservative was also found to have antioxidant, antidepressant, anti-inflammatory, and anticancer properties. However, excess intake of vanillin can cause liver and kidney malfunction therefore rapid detection of vanillin is essential and it can be done electrochemically since the molecules contains electrochemically active groups. However, on a bare GCE, the overpotential for vanillin oxidation is too high and the ease of adsorption of vanillin results in electrode poisoning thus limiting its detection. Considering the unique properties of MOFs and MPcs, an electrochemical sensor for vanillin was developed based on FePc@MOF composite modified GCE. Good electrocatalytic performance was observed when the sensor was used for vanillin detection in tablets and human serum. This may be attributed to adsorption of vanillin onto the MOF pores and the extended π-system which facilitates rapid electron-transfer resulting in increased oxidation rate (*172*).

Nitrite is another common environmental contaminant that may be found in soil and water. It is also used in farming and the food industry as a preservative but accumulation of nitrite in the environment results in negative impacts in the eco-system and threatens public health. Thus, development of a detection strategy with high sensitivity, selectivity and rapid response towards nitrite is important. A 2D NiPc-MOF nanosheet biosensor was developed for this purpose. The biosensor exhibited a very wide detection range with LOD, great stability and good selectivity towards nitrite. This is because the high electrochemical conductivity of the nanosheets improves electron transfer which in turn enhances sensitivity towards nitrite detection. The high surface area of the MOF nanosheets also presents excess electrochemically active catalytic sites for nitrite detection (*173*). A similar strategy was used for detection of cytotoxic trichloracetic acid in drinking water using a FePc@ZIF-8 sensor which exhibited excellent sensitivity, LOD and good selectivity towards the contaminant. The enhanced adsorption of the analyte was due to the high adsorption capacity of ZIF-8 which prevents agglomeration in FePc and enhances its sensing ability (*174*).

Realising the gap in the use of Pc@MOF composites modified electrodes as electrochemical sensors in environmental monitoring, our work will focus on the utilization of these hybrid

materials as catalysts for emerging water contaminants. Prior to modelling a water remediation system based on the electrochemistry of Pc@MOF composites, we need to know the sources of the pollutants, understand their effects and why existing water treatment processes are ineffective.

2.11 Micropollutants in water: An overview

2.11.1 Sources, effects, and remediation

The essence of water for the sustainability of all life on earth is undeniable. Regardless of its use, water remains a very important commodity, therefore it is crucial to protect water sources from contamination. The impairment of the natural state of water to an extent that it cannot serve its purpose to humankind and biotic communities can be described as water pollution. Water pollution results from human activities and inadequate removal of hazardous substances from water bodies may results in serious consequences such as the onset of fatal diseases making water pollution a major global concern (*175, 176*). Amongst many other water pollutants, in this study we will focus on micropollutants.

Toxic chemical compounds detectable in the environment at trace concentrations qualify as micropollutants. Micropollutants are also known as emerging water contaminants (EWC). These come from our homes, pharmaceutical, and agricultural industry and amongst various anthropogenic and endocrine disrupting contaminants (EDCs), pharmaceutical and personal care products (PPCPs) are the most common contaminants found in water. Often, EWC are used to improve human livelihood and are ubiquitous, making it difficult to remove significant levels from the water environment. The persistence of EWC in wastewater when conventional water treatment processes are used for remediation threaten human health and the ecosystem (*177*). To circumvent this problem chromatography, spectrochemistry and fluorescence amongst others have been explored as techniques for monitoring micropollutants in water system. However, these techniques have low specificity and requires multistep sample preparation (*178*). Simple, affordable, specific, and efficient detection of micropollutants in water systems may be achieved through electrochemical sensing and for the purpose of this study we will briefly discuss on the electrochemical detection of chlorophenols as emerging water contaminants.

2.11.2 Electrochemical detection of chlorophenols in water

Phenols are a group of compounds that contain at least one aromatic ring and hydroxyl substituents. They are mainly produced from industrial processes but may also be a product of waste incineration. Chlorophenols (CPs) in particular are widely used in our homes, agricultural and pharmaceutical industry as disinfectants, dyes, insecticides, herbicides, drugs and in wood preservation. Due to their resistance to biodegradation and accumulation in the environment, CPs have been classified as priority pollutants because of their potent toxicity to both terrestrial and aquatic ecosystems. Therefore, it is crucial to monitor CPs rapidly and efficiently in the environment. Thus, electrochemical analysis has taken precedence over other conventional analytical techniques in the detection of CPs (*179-181*).

The basis of electrochemical analysis is the generation of a measurable electrical signal when an analyte interacts with a material sensitive to it. CPs are good candidates for this technique as their phenol and hydroxyl groups make them electrochemical active. Unfortunately, there is weak interaction between CPs and conventional electrochemical sensors therefore electrode modification is required in order to improve electrode performance. Many materials have been used for this purpose for example, Cu-Au NPs had been loaded on rGO for modification of a GCE which was used for CP detection. The modified Cu-Au/rGO/GCE demonstrated high sensitivity and selectivity towards 4-CP even in the presence of other organic compounds and common ions owing to an increased surface area which improves electron transfer. The composite electrode also exhibited high stability, could be reproduced and its shelf-life made it suitable for industrial use (*182*).

To our knowledge, MPc@ZIF-8 and MPc@UiO-66 composites have not yet been used for the detection of chlorophenols. Therefore, this study will focus on the electrochemical sensing of 4-chlorophenol on GCE modified with MPc@MOF composites.

Chapter 3: Experimental

3.1 Materials

All reagents and solvents were obtained from accredited suppliers. 1,4-Benzene dicarboxylic acid (H_2BDC), 1,8-Diazabicyclo (5.4.0) undec-7-ene (DBU), 2-methylimidazole (Hmim) 4-chlorophenol, acetic anhydride (Ac_2O), aluminium oxide (Al_2O_3), ammonium solution (NH_4OH), cobalt (II) acetate ($Co(OAc)_2$), formamide ($HCONH_2$) , formic acid (HCO_2H) , iron (II) phthalocyanine (Fe(II)Pc), manganese (II) phthalocyanine (Mn(II)Pc), monobasic potassium phosphate (KH_2PO_4), phthalic acid, sodium hydroxide (NaOH), thionyl chloride ($SOCl_2$), zinc acetate dihydrate ($Zn(OAc)_2.2H_2O$), zirconium (IV) chloride ($ZrCl_4$) were purchased from Merck. Diethyl ether, deuterated dimethyl sulfoxide (δ-DMSO), N, N-dimethylformamide (DMF) , n-pentanol were purchased from Radchem or Merck. All solvents were used without further purification except DMF which was distilled before use. Dry solvents were dried on molecular sieved purchased from Merck and Millipore water was used for aqueous solutions.

3.2 Instrumentation

A thermo scientific Labofuge 700 centrifuge was used to separate the pellet from the supernatant. Brunker Alpha Fourier transform infrared (FTIR) spectroscopy with platinum attenuated total reflectance (ATR) sampling accessory was employed for recording infrared spectra. Proton NMR (^{1}H-NMR) spectrum was recorded on Brunker Avance III 300 MHz NMR spectrometer. Brunker D2 Phaser benchtop diffractometer using Cu Kα ($\lambda = 1.5405$ Å) was used for recording powder X-ray diffraction (PXRD) patterns. A rate of 2 per minute at $5° < 2\theta < 70°$ was applied when scanning the samples. UV-vis measurements were recorded on Agilent Cary 60 UV-Vis spectrophotometer. Information about the topography of the samples was obtained by scanning the surface of the samples using the Zeiss Crossbeam 540 FEG scanning electron microscopy (SEM) coupled with energy dispersive X-ray (EDX) spectroscopy to determine the elemental composition of the samples. The BET surface area analysis was carried out on Quantachrome (NOVAtouch NT 2LX-1, Volts 220, USA), a gas sorption analyser operated with Quantachrome TouchWin Software Version 1.22. The samples were degassed at 150 °C.

3.3 Electrochemical analysis

A three-electrode system was used to obtain CV data. A modified GCE with a 3 mm diameter was used as a working electrode. The electrode was modified by drop casting of concentrated MOF composites on the surface of the GCE. Ag|AgCl wire was employed as the reference electrode while a platinum wire was used as the counter electrode. The data was recorded using the VersaSTAT 3F potentiostat from Princeton Applied Research operated with Versa Studio software. Phosphate buffered saline (PBS), pH 7 was used as the supporting electrolyte. Prior to performing the experiments, the GCE was polished with a slurry of alumina on a Buehler felt pad and rinsed with Millipore water. Electrocatalytic measurements for oxidation of 4-chlorophenol were performed in solutions containing 0.2 – 1 mM of the analyte.

3.4 Synthesis

3.4.1 Phthalocyanine

Phthalocyanines were synthesized following procedures similar to those reported in (*183*) and (*184*).

3.4.1.1 Phthalic anhydride (2)

Phthalic acid (**1**) (10 g, 60.19 mmol) was refluxed in Ac_2O (12 ml) until a yellow solution was formed. Following which, the solution was refluxed for another 10 minutes. The solution was transferred from the round bottom flask into a porcelain dish and allowed to cool. As a result of cooling, a yellow precipitated was formed, ground with a pestle then washed with diethyl ether several times until the unreacted acid was undetected. Yields: 8.5g (85%). IR (v_{max}/cm^{-1}): 1757 (C=O).

3.4.1.2 Phthalimide (3)

Compound **2** (8g, 54.02 mmol) was heated under reflux in the presence of $HCONH_2$ (13 ml). The mixture formed was cooled at room temperature, and the resulting product was washed with water and isolated through suction filtration. The title compound was dried in an oven at 60 °C. Yield: 7.4 g (93%). IR (v_{max}/cm^{-1}): 3180 (N-H).

3.4.1.3 Phthalamide (4)

In 35% NH_4OH (60 ml), phthalimide (**3)** (7 g, 47.58 mmol) was stirred for 24 hours. The mixture was filtered and the resulting precipitated was washed several times with ice cold water

until excess ammonia was untraceable, then the compound was dried at 60 °C. Yield: 6.5 g (92%). IR (v_{max}/cm^{-1}): 3424 (N-H).

3.4.1.4 Phthalonitrile (5)

In a two-necked round bottom flask, dry DMF (61 ml) was cooled to 0 °C under nitrogen (N_2). $SOCl_2$ (62 ml) was added dropwise under continuous stirring and the temperature was maintained at 0 °C for 2 hours using an ice bath. Compound **4** (6g, 36.55 mmol) was introduced to the reaction, forming a yellow mixture. The temperature was maintained below 5 °C while the mixture was stirred for an additional 5 hours then allowed to reach ambient temperature and left to stir overnight. Finally, the mixture was precipitate on crushed ice, and the precipitate was isolated by filtration and washing with cold water. The light-yellow compound was then dried at 110 °C. Yield: 5 g (83%). IR (v_{max}/cm^{-1}): 2233 (CN). ^{1}H-NMR (DMSO-d_6): δ (ppm): 8.16 (1H, m, Ar-H), 7.94 (1H, m, Ar-H).

3.4.1.5 Metal (II) phthalocyanine (6-8)

A mixture of phthalonitrile (**5**) (2 g, 15.61 mmol), $Co(OAc)_2$ (0.7 g, 3.9 mmol) and anhydrous pentanol (15 ml) were heated at 160 °C under nitrogen. The reaction was performed in the presence of DBU (8 drops) as a catalyst. The temperature was maintained while stirring for 24 hours. The mixture was filtered off and the crude product was refluxed in ethanol for 2 hours, then washed multiple times with hot ethanol, water, and diethyl ether to obtain Cobalt (II) phthalocyanine (**6**). The product was left to dry in air. Yield: 1.3 g (58%). Formation of the title compound was confirmed by the Q-band at λ_{max}: 667 nm and B-band at λ_{max}: 320 nm observed in the UV/vis spectrum of the compound. Iron (II) phthalocyanine **(7**) and manganese (II) phthalocyanine (**8**) were obtain in a similar way using $FeCl_2$ and $MnCl_2$ as metal sources.

3.4.2 MOF synthesis

3.4.2.1 ZIF-8 (9)

ZIF-8 was prepared by dry-gel conversion (*62*) with some changes. $Zn(OAc)_2.2H_2O$ (3 g, 13.67 mmol) and Hmim (11.22 g, 136.7 mmol) were placed in a Teflon lined stainless steel autoclave. Millipore water (55 ml) was added at the bottom of the autoclave. The autoclave was sealed tightly and heated at 120 °C for 24 hours. The autoclave was then allowed to cool down at ambient temperature. Centrifugal force was applied to isolate the newly prepared ZIF-8. The product was washed repeatedly with Millipore water then dried in vacuum at 150 °C for

6 hours to obtain a white powder. Yield: 1.96 g, (63%). The PXRD pattern corresponded to literature (*67*) which confirmed successful synthesis of the ZIF-8.

3.4.2.2 UiO-66 (10)

UiO-66 was synthesized following a procedure reported in (*185*) with some modifications. $ZrCl_4$ (1.06g, 4.55 mmol) and H_2BDC were dissolved in DMF and sonicated for 30 minutes. HCO_2H (17 ml) was added in the mixture then transferred to Teflon lined autoclave and placed in an oven at 120 °C for 24 hours. The crude product was collected by centrifugation and finally washed with hot ethanol. The final white precipitate obtained was then dried at 80 °C in a conventional oven. Yield: 1.07 g. PXRD confirmed that the white powdery compound was indeed UiO-66.

3.4.3 MOF composites

3.4.3.1 ZIF-8 composites

CoPc@ZIF-8 **(11)** was obtained by dry gel conversion. Compound **6** was dispersed into DMF (50 ml) and sonicated for 30 minutes. Compound **9** was added to the mixture then sonicated for a further 30 min. The solution was placed in a Teflon plate inside a stainless-steel autoclave and heated for 24 hours at 120 °C. The composite was isolated by centrifugation, washed with water several times, and dried in a vacuum oven for 6 hours at 150 °C. This was repeated for FePc@ZIF-8 **(12)** and MnPc@ZIF-8 **(13)** replacing compound **6** with compound **7** and **8** respectively.

3.4.3.2 UiO-66 composites

CoPc@UiO-66 **(14)**, FePc@UiO-66 **(15)** and MnPc@UiO-66 **(16)** were prepared as described for ZIF-8 composites (**11-13**) except compound **9** was replaced with compound **10** and hot ethanol was used for washing.

3.5 4-Chlorophenol solution preparation

A solution of 4-chlorophenol (1 mM) in PBS was prepared in a 200 ml volumetric flask. This was diluted with PBS to 0.8 mM, 0.6 mM, 0.4 mM, and 0.2 mM in 50 ml volumetric flasks and the different concentrations were used to determine the limit of detection of the composite modified electrodes in pH 7 buffer.

Chapter 4: Results and discussion

4.1 Phthalocyanine synthesis and characterization

Metal phthalocyanines were synthesized according to literature (*131, 186*) as shown in **Scheme 4.1**. Phthalic acid (**1**) was used as a precursor for phthalonitrile (**5**) synthesis which was used for the synthesis of unsubstituted metal phthalocyanines (MPcs) **(6-8)**.

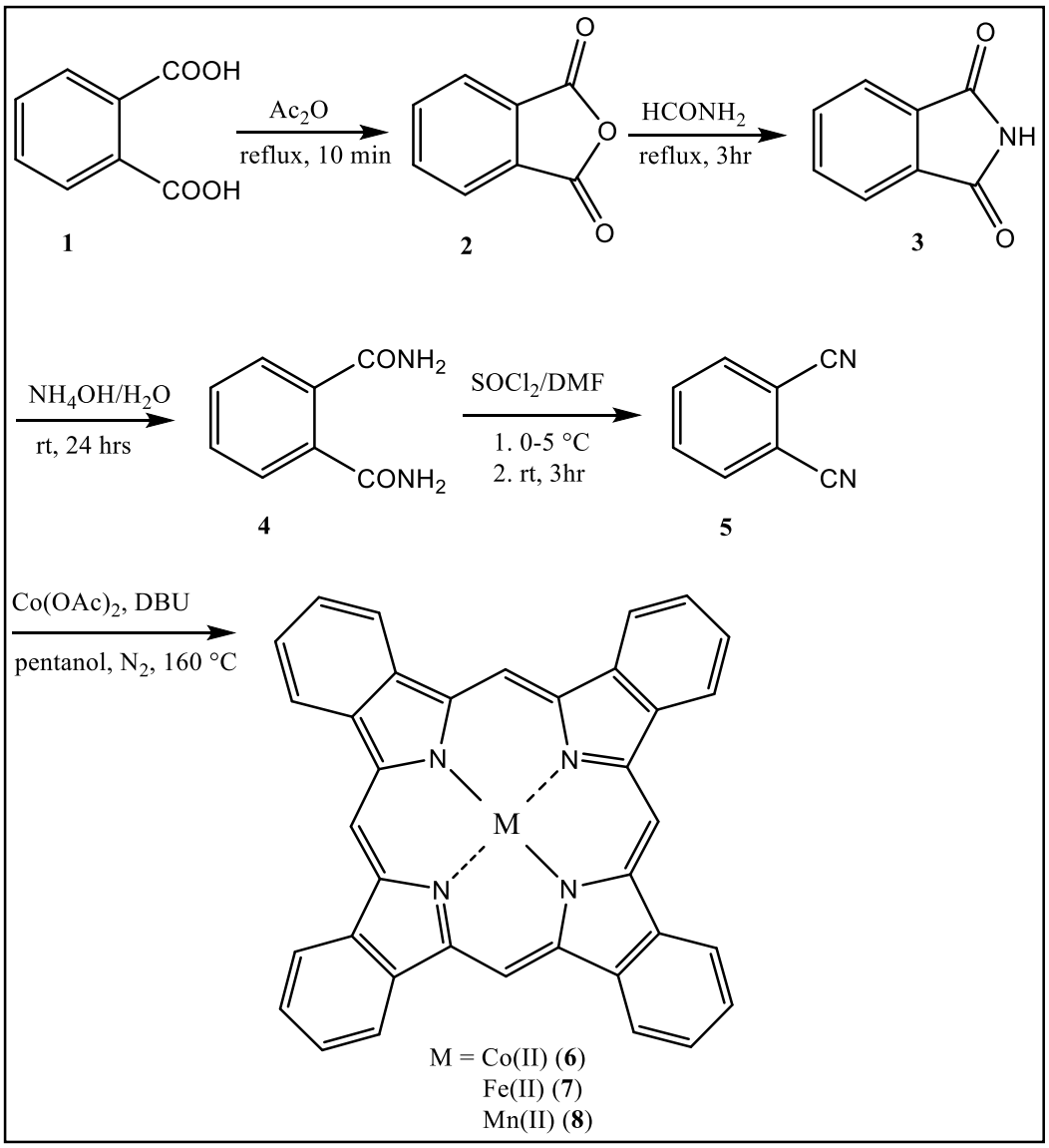

Scheme 4.1: Synthetic pathway to MPc formation.

Fourier transform infrared (FTIR) spectroscopy data was obtained for the stepwise synthesis of the Pc precursor (**5**). The presence of the two C=O bands at 1757 cm^{-1} and 1845 cm^{-1} confirmed conversion of the acid (**1**) to an anhydride (**2**). Amide formation to yield compound **3** was confirmed by the appearance of the N-H band at 3180 cm^{-1}. Ammonium solution was

used for the conversion of compound **3** to compound **4**, an amide band at 3424 cm^{-1} confirmed successful conversion. The disappearance of the amide band and appearance of the CN stretch at 2233 cm^{-1}, presence of the aromatic C-H band at 3040 cm^{-1} and multiple C=C bands between 1400 – 1600 cm^{-1} (**Fig. 4.1**) confirmed formation of compound **5**.

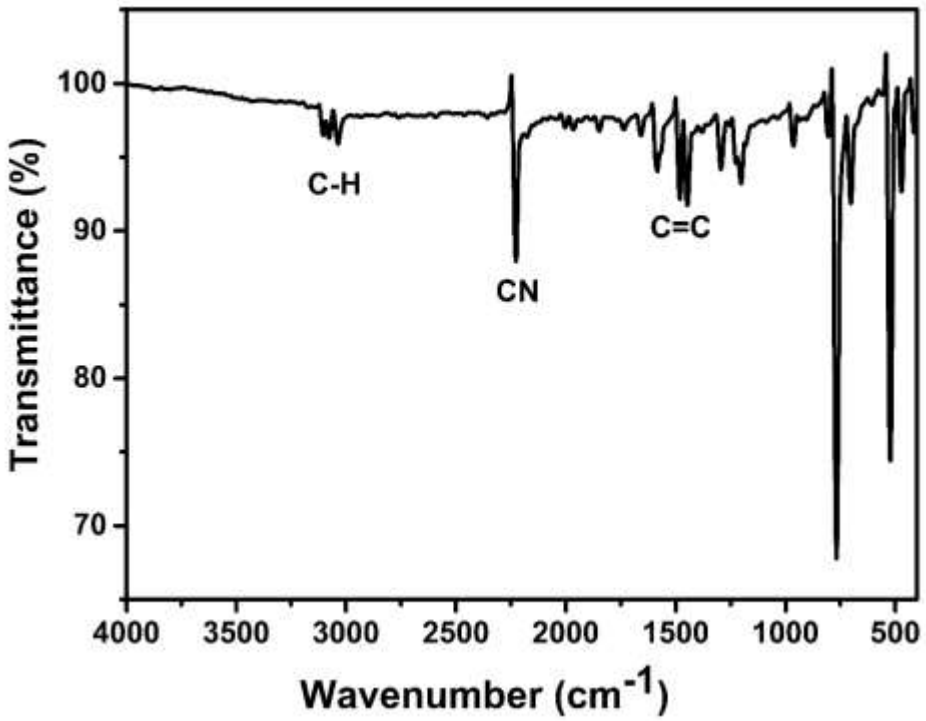

Figure 4.1: IR spectrum of compound **5**.

Nuclear magnetic resonance (NMR) was used to confirm formation of the symmetrical compound (**5**). The proton NMR of compound **5** (**Fig. 4.2**) shows a doublet of doublets (d,d) at 8.16 ppm corresponding to proton **a**, and another at 7.94 ppm corresponding to proton **b**. This type of coupling is due to ortho and meta coupling. Meta coupling, being the coupling between protons that are four bonds apart and is normally observed in aromatic compounds due to maximised orbital interactions between protons, lining up in a zig-zag planar fashion. Proton **a** appears downfield due to the presence of electron withdrawing nitrile groups which pull electron density away from the nucleus, deshielding it, leading to a larger chemical shift. As a result of symmetry in the chemical structure of the compound, two protons can be found in the same environment. Therefore, each doublet of doublets represents two protons (2H) for protons **a** and **b** which in total represents all the four protons present in the phthalonitrile structure.

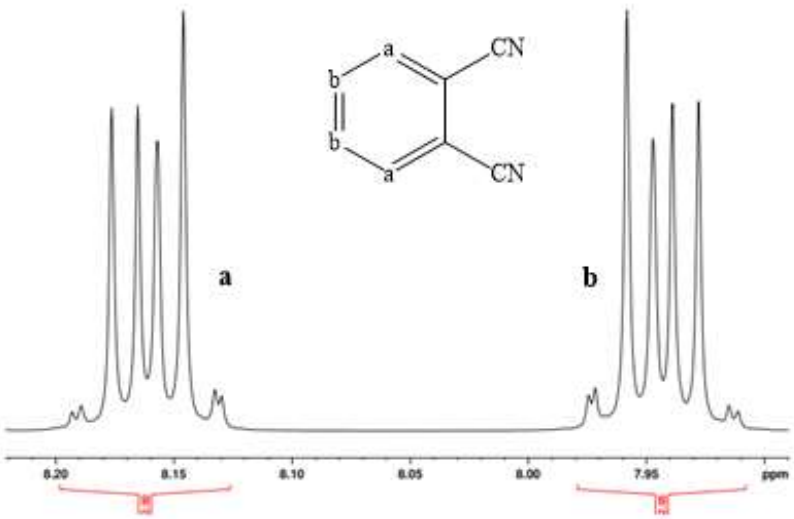

Figure 4.2: ^{1}H NMR spectrum of compound 5 in DMSO-d_6.

Compound **5** was used for the formation of MPcs (compounds **6-8**). This was confirmed using UV-vis spectroscopy amongst other techniques. **Fig. 4.3** shows the absorption spectra of CoPc (**6**), FePc (**7**) and MnPc (**8**) in DMF which exhibit the characteristic absorption peaks of phthalocyanines. The B band result from transitions between the a_{2u} (π) and b_{2u} (π) HOMO to the doubly degenerate e_g (π^*) LUMO. The Q band is a result of an electron transition between the a_{1u} (π) HOMO and the π^* (e_g) LUMO (**Fig 2.10**). Compounds **6**, **7** and **8** exhibit B bands at 321 nm, 326 nm, and 358 nm respectively while the Q bands of the compounds were observed at 662 nm, 653 nm, and 715 nm respectively.

The Q band of compound **8** is red shifted compared to those of compound **6** and **7**. This can be attributed to the Mn(II) ion being very labile, therefore, strong electron donor power of the Pc ligand may result in easy oxidation of the complex to Mn(III) state (*187*). Among all transition metal Pcs, Mn(II)Pc possesses the smallest energy gap between occupied and unoccupied molecular orbitals of the complex which results in the red shift of the Q band (*188*). The delocalisation of π-electrons within the conjugated system of MPcs permit interaction between the metal and ligand and this can lead to charge transfer. There are three types of charge transfer reactions, namely, ligand to metal charge transfer (LMCT), metal to ligand charge transfer (MLCT) and metal to metal charge transfer (MMCT). MLCT bands were observed at 450 nm

and 500 nm in the absorption spectra of the MPcs (**Fig. 4.3**) which are attributed to π-π* transitions between the HOMO of the metal and the LUMO of the ligand (*189*).

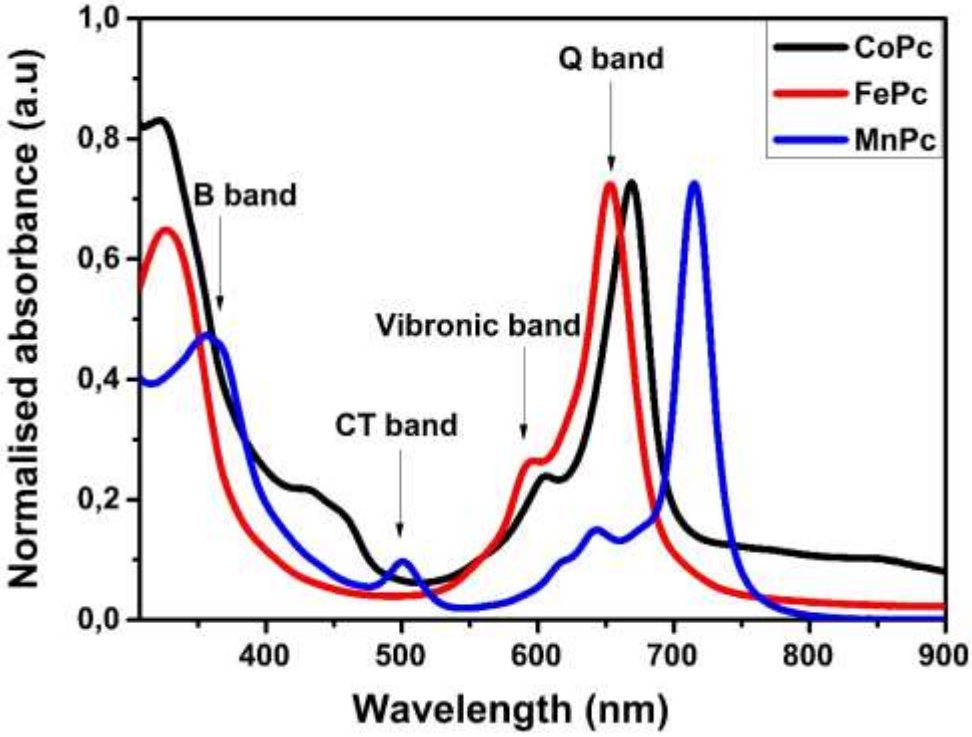

Figure 4.3: Absorption spectra of CoPc (black), FePc (red) and MnPc (blue) in DMF.

4.2 MOF synthesis and characterization

ZIF-8 and UiO-66 were synthesized using previously reported methods (*62, 185*). Zn $(OAc)_2.2H_2O$ and $ZrCl_4$ were used as metal sources. Hmim and H_2BDC were used as coordinating ligands to form ZIF-8 and UiO-66, respectively. The reactions were performed in a sealed Teflon lined stainless steel autoclave at 120 °C, overnight. Water was used a solvent for ZIF-8 synthesis and DMF was used for UiO-66 synthesis. The crude products were isolated using centrifugal force, washed with water or ethanol, and dried in a conventional oven or under vacuum to obtain white ZIF-8 or UiO-66 powders.

4.2.1 Scanning electron microscopy (SEM) and EDX

SEM was used to investigate the morphology of ZIF-8, and UiO-66. A rhombic morphology was observed for ZIF-8 which corresponds to what is reported in literature (*64, 67*). However, the experimental sample displayed aggregated particles with irregular sizes (**Fig. 4.4a**). Similarly, the SEM images for UiO-66 revealed aggregated particles of irregular sizes and shapes (**Fig.4.4b**). EDX was used to analyse the elemental composition of the MOFs (**Fig. 4.4c**

and d). The compounds were coated with carbon prior to analysis and during analysis nitrogen and oxygen may have also been picked up from the atmosphere while hydrogen is too light to be detected by the instrument. Although the synthesized compounds contain these elements, we will only focus on the atomic masses of the transition metal elements to confirm the composition of the compounds. **Table S1** displays that ZIF-8 contains 29% Zinc (Zn) and **Fig 4.4c** shows that a peak which arises from the removal of an electron from the core K shell of the atom was detected at 8.2 ekV. **Table S2** shows that UiO-66 contains 16% of zirconium (Zr) which was confirmed by the presence of the peak at 2 keV (**Fig. 4.4d**) resulting from the ejection of an electron from the L shell of the Zr atom. The MOFs showed high purity as no impurities were detected.

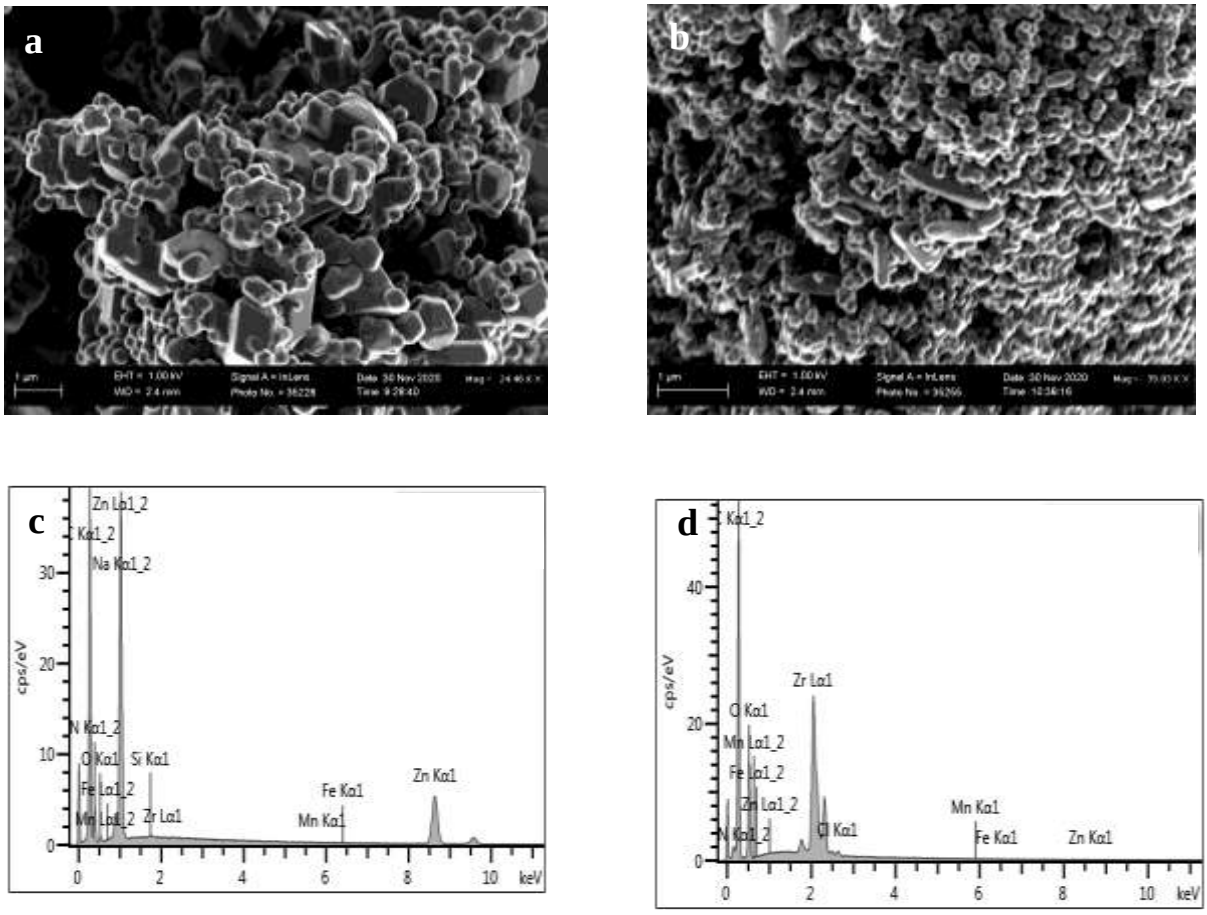

Figure 4.4: SEM images of (a) ZIF-8 and (b) UiO-66. EDX spectra of (c) ZIF-8 and (d) UiO-66.

4.2.2 Powder X-ray diffraction (PXRD)

PXRD was used to assess the phase purity and crystallinity of ZIF-8 and UiO-66. The ZIF-8 diffractogram (**Fig. 4.5a**) exhibited peaks at 7.48°, 10.55°, 12.87°, 14.89°, 16.69°, 18.26°, 24.61°, 25.88°, 26.78°, 29.85°, 30.89°, 32.61° which correspond to (011), (002), (112), (022), (013), (222), (222), (114), (223), (134), (044), (244), (235) planes with more pronounced peaks visible at $2\theta < 20°$. UiO-66 (**Fig. 4.5b**) exhibited peaks at 7.53°, 8.66°, 12.17°, 14.34°, 18.75°, 19.28°, 21.14°, 22.34°, 24.51°, 25.93°, 28.33°, 30.05°, 30.94°, 32.44°, 33.34°, 34.68° which correspond to the (111), (002), (022), (113), (222), (004), (133), (024), (115), (044), (135), (006), (335), (444), (117), (246), (355), (008) planes.

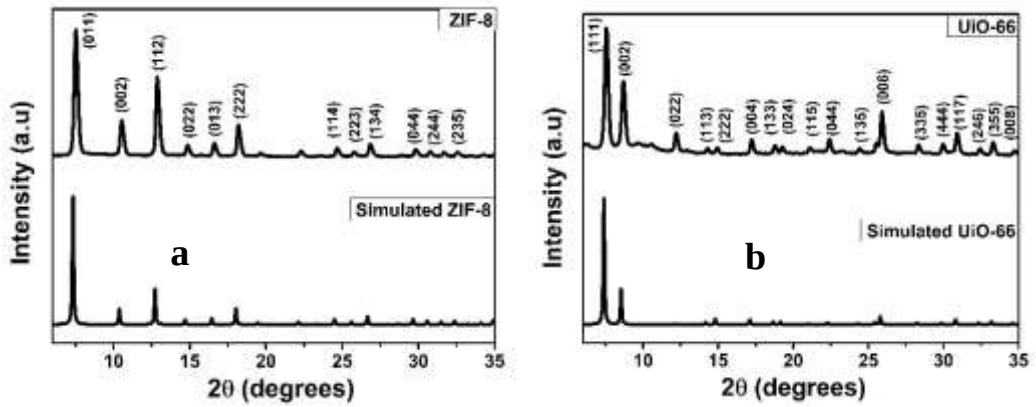

Figure 4.5: Diffractograms of simulated and experimental (a) ZIF-8 and (b) UiO-66.

The XRD patterns were in good agreement with the XRD COD database file 4118891 and CCDC database file 733454 simulated using Mercury software. This revealed that the synthesized MOFs were pure. Furthermore, the diffraction peaks of the synthesized MOFs are sharp compared to the simulated pattern, indicating good crystallinity. The sample crystallite sizes of 276 nm and 34 nm were calculated from half the peak width at maxima (011) and (111) for ZIF-8 and UiO-66 respectively, using Scherrer's equation:

$$D = \frac{0.9\lambda}{\beta Cos\theta} \qquad 4.1$$

where D is the crystallite size, λ is the copper wavelength (1.5405 Å), θ is Bragg's diffraction angle of the most the intense peak and β is peak broadening, measured in radians (Rad) at the full width at half maximum (FWHM) of the most intense peak. β is calculated using Origin software.

4.2.3 Brunauer Emmett Teller (BET) analysis

The specific surface area and pore volume of ZIF-8 and UiO-66 were calculated using BET. The surface area and a pore volume of 1943 m^2/g and of 0.58 cc/g were obtained for ZIF-8 in agreement with literature (*71*) . On the other hand, a surface area and a pore volume of 1634 m^2/g and 0.66 cc/g were reported for UiO-66, which are also similar to literature (*190*). ZIF-8 exhibits a type I isotherm with a H3 type loop (**Fig 4.6a**) indicating a combination of microporous and mesoporous particles (*191*). The H3 type loop observed in the ZIF-8 isotherm is related to non-rigid aggregates of plate-like particles giving rise to slit-like pores (*192*). The N_2 sorption isotherms of UiO-66 (**Fig. 4.6b**) shows a type IV isotherm for UiO-66. The increase in adsorbate uptake observed for this isotherm is associated with monolayer and multilayer adsorption on mesoporous materials with smaller mesopore widths. This type of isotherm is characteristic of conical and cylindrical mesopores that are closed at the tapered end (*58*). A narrow pore size distribution (**Fig. 4.6 c and d**) was obtained for both ZIF-8 and UiO-66.

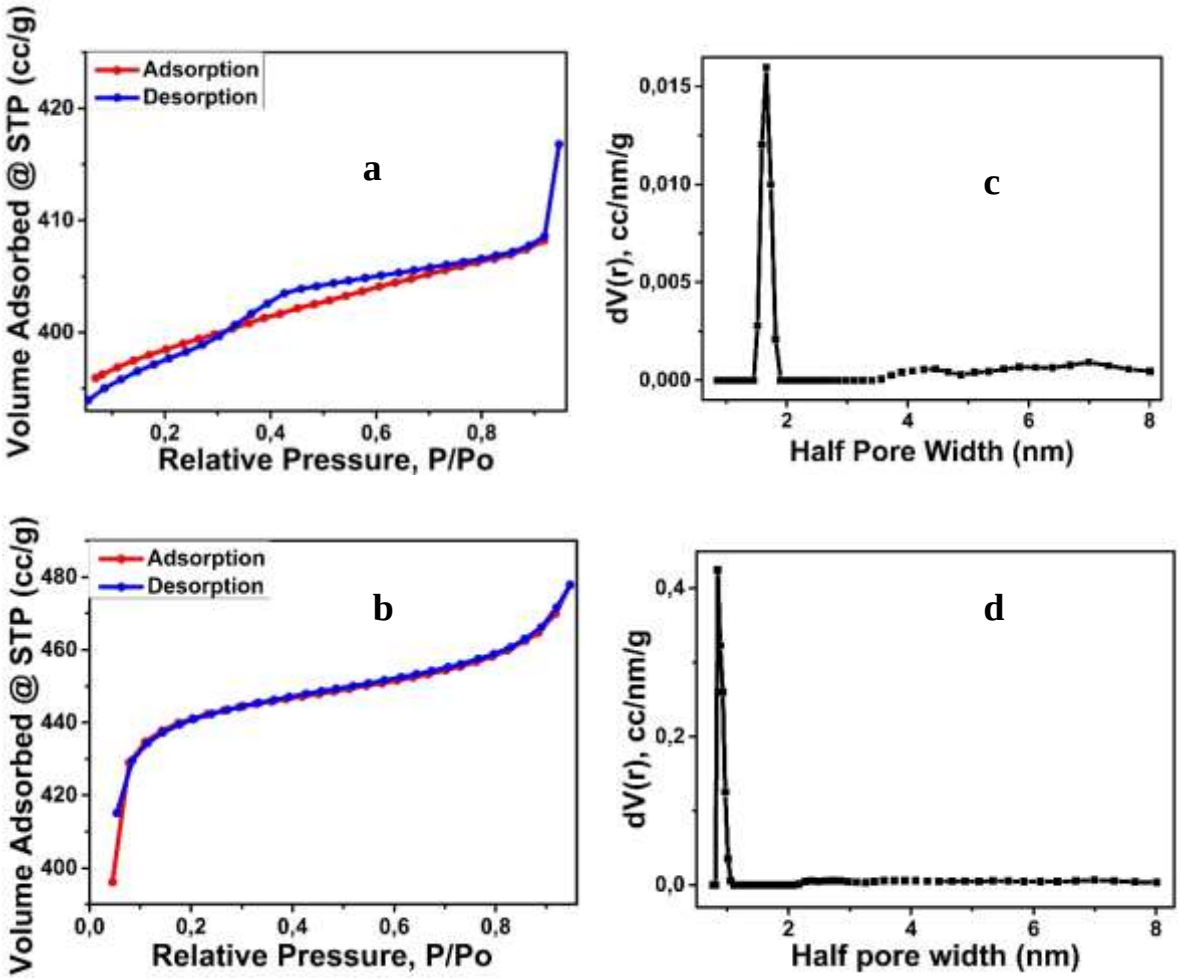

Figure 4.6: Adsoprtion isotherms of (a) ZIF-8 (b) UiO-66 and pore size distribution of (c) ZIF-8 (d) UiO-66.

4.3 MOF composite synthesis and characterization

MPc@MOF composites were synthesize according to the dry-gel conversion method (*62*). MPcs (CoPc, FePc or MnPc) were dispersed in DMF and sonicated for 30 minutes. ZIF-8 or UiO-66 were added to the MPc mixture then sonicated for another 30 minutes. The solution was placed in a Teflon plate inside a stainless-steel autoclave and heated overnight at 120 °C. The crude products were isolated by centrifugation, washed with water several times, and dried in a vacuum oven, obtaining green or blue MPc@MOF composite powders.

4.3.1 Scanning electron microscopy (SEM) and EDX

The morphology of the MOF composites was investigated using SEM. **Fig. 4.7** shows the SEM micrographs of the MOF composites. As seen from the SEM images, the composites appear as highly agglomerated structures with particles of undefined shapes wrapped around rod like structures. EDX was used to perform elemental analysis and the atomic percentages of the metal elements that the ZIF-8 composites contains can be seen in **Tables S3-S5**. We except the composites to be composed of either Zn or Zr from the MOFs and Fe, Mn, or Co from the MPcs. The FePc@ZIF-8 composite (**Table S3**) is composed of 10% Zn and 45% iron (Fe). The MnPc@ZIF-8 composite (**Table S4**) is made up of 20% Zn and 10% Mn. The CoPc@ZIF-8 composite (**Table S5**) contains 70% Co and 30% Zn. As seen in **Fig. S1 a-c**, the EDX spectra of the ZIF-8 composites indicate that the elemental data was obtained by removing an electron from the core K shell of Fe, Mn, and Co metals in FePc@ZIF-8, MnPc@ZIF-8 and CoPc@ZIF-8, respectively. The presence of the Fe signal at 6.2 keV (**Fig. S1a**) , Mn and Co signals at 6 keV (**Fig. S1 b and c**) confirm that the MPcs were incorporated into ZIF-8.

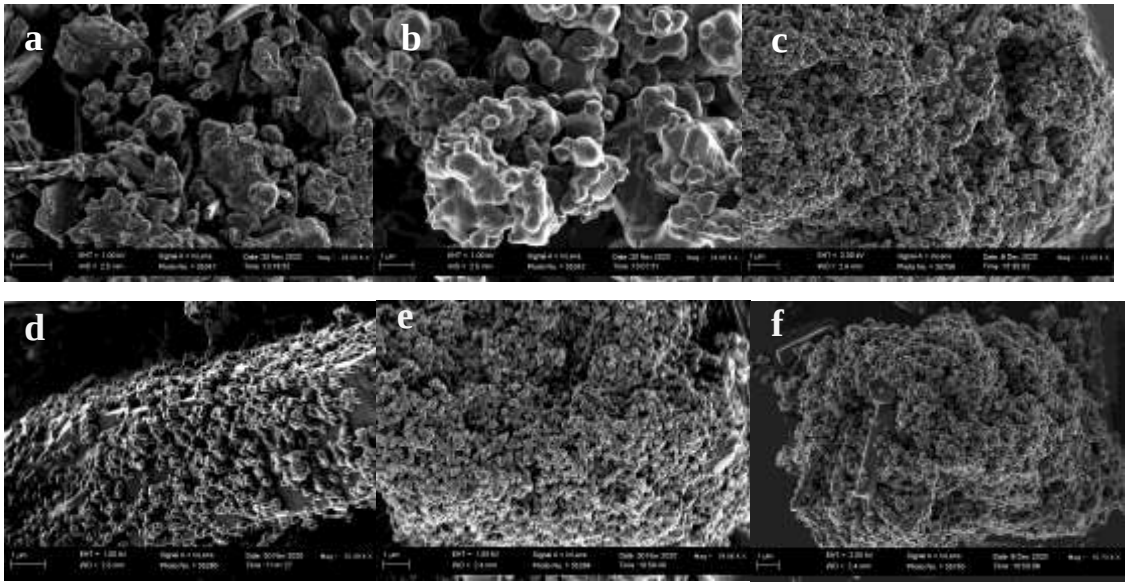

Figure 4.7: SEM images of MOF composites (a) FePc@ZIF-8 (b) MnPc@ZIF-8 (c) CoPc@ZIF-8 (d) FePc@UiO-66 and (e) MnPc@UiO-66 and (f) CoPc@UiO-66.

Similarly, the MPc@UiO-66 composite (**Fig. S1 d-f**) displayed elemental signals attributed to the Fe, Mn and Co atoms of the MPcs. The signals observed on the EDX spectra of UiO-66 composites in **Fig. S1 d** show that an electron was lost from the core K shell of Fe at 6.2 keV for the FePc@UiO-66 composite. Two elemental signals were observed for the MnPc@UiO-66 and CoPc@UiO-66 composites (**Fig. S1 e and f**). The first signal at 2 keV indicates the loss of an electron from the L shell of Zr and the second signal at 6 keV indicates the loss of the core K shell electron from Mn and Co, respectively. The atomic percentages are in agreement with the EDX spectra for the UiO-66 composites. **Tables S6-S8**, show that FePc@UiO-66 contains 10% Fe and 7% Zr. The MnPc@UiO-66 composite is made up of 13% Zr and 4% Mn. Lastly, the CoPc@UiO-66 composite contains 19% Zr and 28% Co.

4.3.2 Powder X-ray diffraction (PXRD)

XRD analysis was used to probe the crystallographic properties and phase purity of the MOF composites. **Fig. 4.8** shows that the diffraction peaks of the all the MPc@ZIF-8 composites are sharp and clear indicating good crystallinity. All the diffraction peaks agreed with the XRD patterns for the MPcs and MOFs. An increase in peak intensity is evident in the XRD patterns of the FePc@ZIF-8 composite (**Fig 4.8a**) and is usually an indication of increased order in the structure. The MnPc@ZIF-8 composite (**Fig 4.8b**) exhibit narrow peaks indicating a reduction in crystallite size while the opposite is true for the CoPc@ZIF-8 composite (**Fig. 4.8c**) displaying broad peaks.

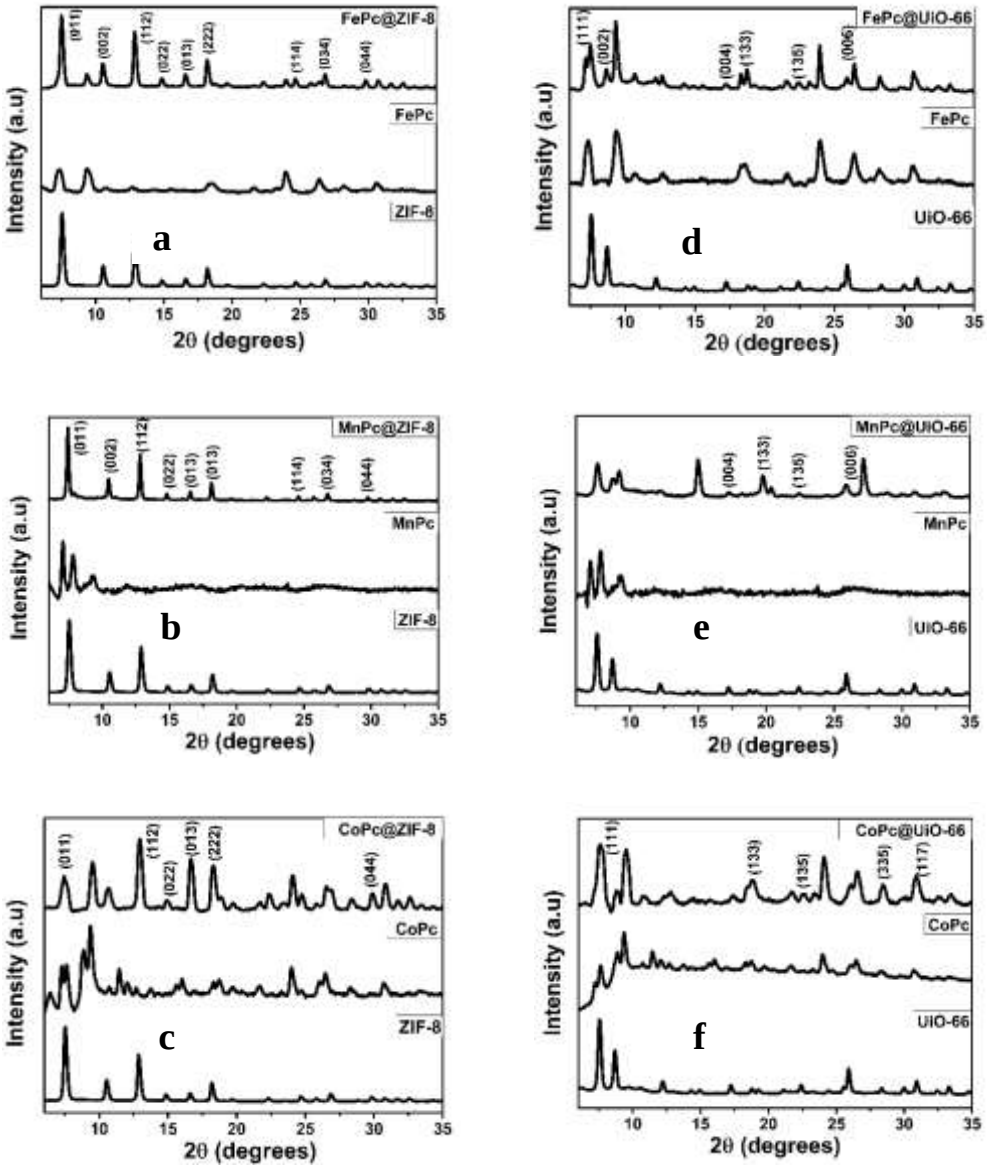

Figure 4.8: PXRD patterns for (a) FePc@ZIF-8 (b) MnPc@ZIF-8 (c) CoPc@ZIF-8 (d) FePc@UiO66 (e) MnPc@UiO-66 and (f) CoPc@UiO-66.

MPc@ UiO-66 composite formation was a success as seen in the diffraction patterns of the synthesized composites. The diffraction pattern of FePc@UiO-66 (**Fig. 4.8d**), exhibits good crystallinity. The appearance of a new peak observed at 15° for MnPc@UiO-66 (**Fig. 4.8e**) is an indication of formation of new phase (*193*). The diffractogram of the composite also displays a right hand shift of peaks at higher 2theta values. The peak shift can be attributed to internal stress within the crystal lattice and phase transformation (*194*). An increase in peak intensity was observed on the diffraction pattern for CoPc@UiO-66 (**Fig. 4.8f**) and peak enhancement indicates increase in crystallinity (*195, 196*). Furthermore, no additional peaks resulting from impurities were detected which indicates phase purity of the composite (*197*).

4.3.3 Brunauer Emmett Teller (BET) analysis

BET analysis was used for investigating the surface area and pore size of the synthesised MPc@MOF composites. The N_2 adsorption curves of ZIF-8 composites (**Fig. 4.9 a-c**) exhibit a type I isotherm and a H3 type hysteresis loop. Contrary to what was observed for ZIF-8, a low-pressure hysteresis loop was observed for the ZIF-8 composites which is associated with irreversible chemical interaction between ZIF-8 and FePc, MnPc or CoPc for the FePc@ZIF-8, MnPc@ZIF-8 and CoPcPc@ZIF-8 composites, respectively. It is also related to deformation of the nonrigid pores of the adsorbent upon interaction with the adsorbate which may be attributed to uptake of adsorbate molecules into pores of the same width (*192*). Type IV isotherms were observed for UiO-66 composites (**Fig. 4.9 d-f**) with the exception of MnPc@UiO-66 (**Fig. 4.9e**) displaying a hysteresis loop that is typical of type IV isotherms and results from condensation of adsorbed vapour into the mesopores, limiting N_2 uptake at higher pressures. With both monolayer and multilayer adsorption demonstrated by this type of isotherm we can assume that the MPc molecules that are not in contact with the surface of the UiO-66 are adsorbed in a non-porous form (*58*). The pore size distribution of ZIF-8 composites (**Fig. S2 a-c**) is broad with the exception of FePc@ZIF-8 (**Fig. S2a**) which shows a narrow pore size distribution like ZIF-8. Similarly to UiO-66, its corresponding phthalocyanine composites display a narrow pore size distribution (**Fig. S2 d-f**).

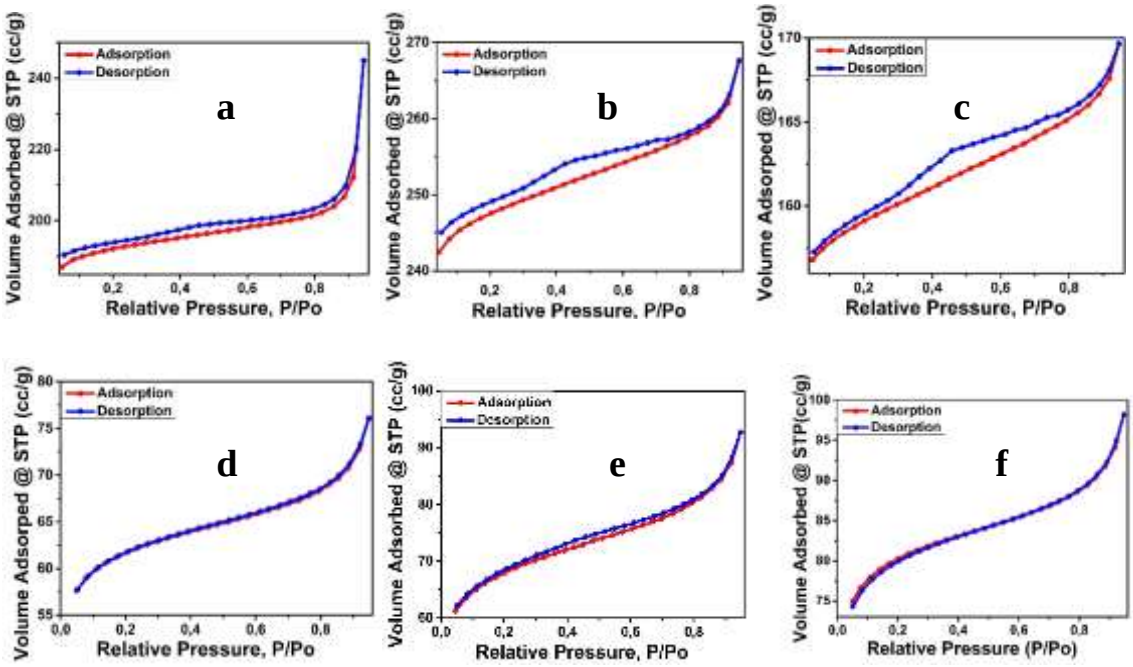

Figure 4.9: Adsorption isotherms of MOF composites (a) FePc@ZIF-8 (b) MnPc@ZIF-8 (c) CoPc@ZIF-8 (d) FePc@UiO-66 (e) MnPc@UiO-66 and (f) CoPc@UiO-66.

Table 4.1 shows the surface areas and pore volumes obtained for the MOFs and their corresponding composites. ZIF-8 shows the highest surface area and pore volume and these decrease upon modification with MPcs. A similar trend was observed for UiO-66 and its composites. However, the UiO-66 composites show a much more significant decrease. The decrease in the surface area and pore volume indicate that the MPcs are within the pores of the MOFs.

Table 4.1 BET surface area and pore volume for MOFs and MOF composites.

MOF/ Composite	**Surface area (m^2/g)**	**Pore volume (cc/g)**
ZIF-8	1943	0.58
UiO-66	1634	0.66
CoPc@ZIF-8	801	0.24
FePc@ZIF-8	806	0.31
MnPc@ZIF-8	1229	0.37
CoPc@UiO-66	238	0.13
FePc@UiO-66	182	0.10
MnPc@UiO-66	192	0.12

4.3.4 UV-vis absorption of MOF composites

Ultraviolet-visible spectroscopy was used to explore the absorption properties of the MOF composites. Unlike MPcs, ZIF-8 and UiO-66 do not absorb in the visible region. The absorption spectra of the composites however, matched those of the MPcs, with the B and Q bands present in the composites between 300-400 nm and 600-700 nm respectively (**Fig. 4.10a - f**). Apart from the charge transfer band around 500 nm observed for MnPc@ZIF-8, a new band was also observed around 600 nm (**Fig. 4.10b**). This peak may result from MPc dimerization due to metal-metal interactions between MnPc molecules. The discovered absorption properties of the composites support all the other characterization techniques in confirming that the MOF composites were formed.

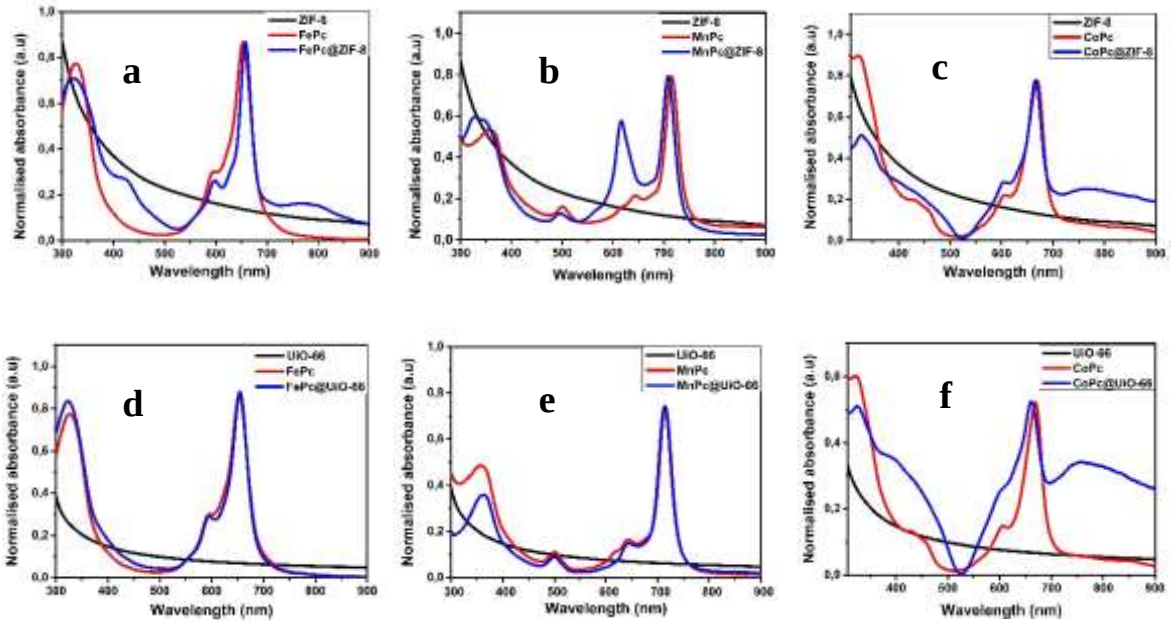

Figure 4.10: Absorption spectra of (a) FePc@ZIF-8 (b) MnPc@ZIF-8 (c) CoPc@ZIF-8 (d) FePc@UiO-66 (e) MnPc@UiO-66 and (f) CoPc@UiO-66.

Chapter 5: Electrocatalysis

5.1 Electrode modification

Phthalocyanine-metal organic framework sensors were fabricated as illustrated in **Fig. 5.1**. The synthesized MOFs and MPc@MOF composites were dispersed in DMF and ultrasonicated to form suspensions. Prior to electrode modification, the GCE surface (3 mm) was polished using alumina slurry on a polishing pad and rinsed off with Millipore water. The GCE was modified using the drop dry method. A sufficient amount of suspension was dropped on the shiny surface of the GCE, and thereafter the electrode was dried in the oven at 100 °C for 5 minutes. The electro-oxidation of 4-chlorophenol on the modified electrode was probed using cyclic voltammetry.

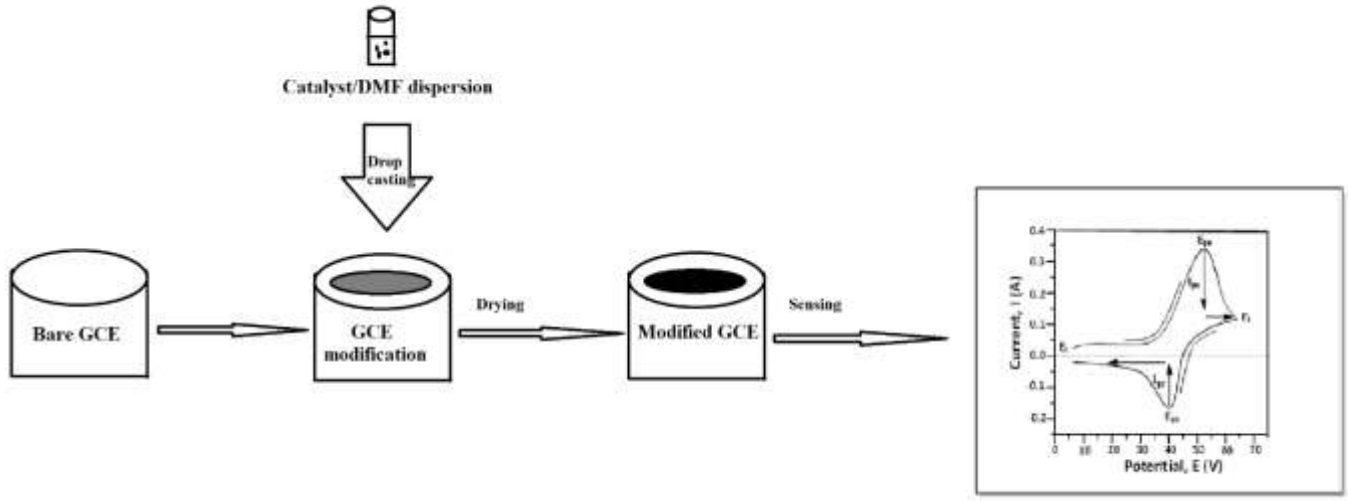

Figure 5.1: Illustration of electrode modification using the drop drying method.

5.2 4-Chlorophenol oxidation

Electrocatalytic oxidation of 4-chlorophenol does not occur at the bare electrode. Therefore, MPc@MOF modified electrodes were used to mediate electron transfer with the aim of reducing the potential and enhancing catalytic currents. **Fig. 5.2** shows catalytic responses of the MOFs and MPc@MOFs. Amongst the ZIF series (**Fig. 5.2a**), the ZIF-8 (**9)** modified GCE showed better catalytic potential with an oxidation peak at 0.49 V. The FePc@ZIF-8 (**12**) modified GCE however, displayed better catalytic current with a peak at 20.06 μA and the MnPc@ZIF-8 (**13**) modified electrode showed no catalytic response.

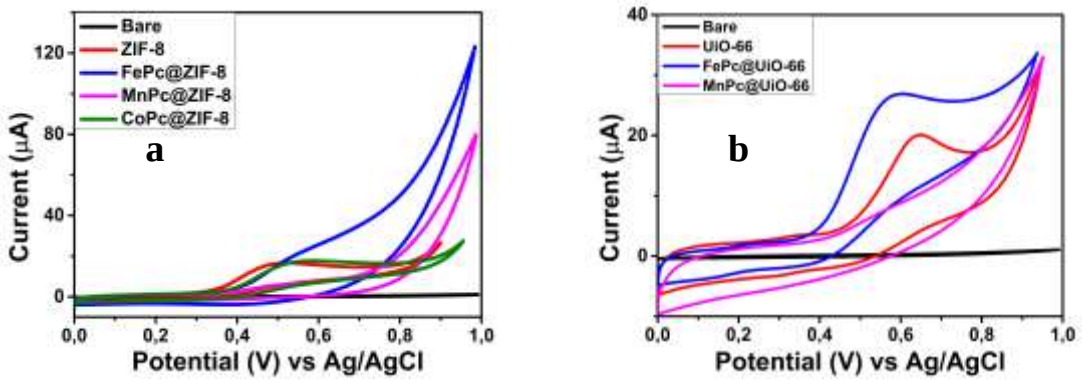

Figure 5.2: Cyclic voltammograms of bare GCE, (a) ZIF-8 composite modified GCE and (b) UiO-66 composite modified electrode for 1 mM 4-chlorophenol oxidation in PBS. Scan rate = 500 $mV.s^{-1}$.

Table 5.1 shows the catalytic responses obtained with Ui0-66 (**10**) and FePc@UiO-66 (**15**) modified electrodes displaying catalytic responses within the UiO-66 series (**Fig. 5.2b**). The FePc@UiO-66 (**15**) modified GCE showed better catalytic response with an oxidation peak at 0.58 V and catalytic current at 26.62 µA. As seen in **Table 5.1** overall, ZIF-8 (**9**) showed the best catalytic performance in terms of potential reduction, and FePc@UiO-66 (**15**) showed the best catalytic current.

Table 5.1 Oxidation of 1 mM 4-chlorophenol on phthalocyanine-MOF modified electrodes in pH 7 PBS buffer. Scan rate 500 $mV.s^{-1}$.

Complex	**E_P (V vs Ag/AgCl)**	**I_p (µA)**	**Limit of detection (mM)**
ZIF-8 (9)	0.49	16.39	1.3
UiO-66 (10)	0.65	20.08	2.8
CoPc@ZIF-8 (11)	0.57	17.62	0.34
FePc@ZIF-8 (12)	0.54	20.06	0.05
FePc@UiO-66 (15)	0.58	26.62	0.67

The ability of the MOFs to detect 4-chlorophenol in aqueous medium can be attributed to their high surface area which provides more active sites for the MOF to interact with 4-chlorophenol in solution. It is noteworthy that the high pore volumes of the MOFs permits adsorption of the MPcs through π-π interactions. Higher catalytic currents were observed using the composites modified electrodes which imply that the presence of MPcs in the composites increases the number of active sites for interaction between the composites and 4-chlorophenol hence better catalytic activity. This is a result of the extended conjugated system that exists in MPc that enhances electron transfer and adsorption of 4-chlorohenol though π-π interactions. Thus on the composites, catalysis occurs on the MPcs with the MOF providing electron transmission.

The limit of detection of the electro-active sensors towards 4-chlorophenol detection was studied and calculated using the 3σ criteria. The results revealed that the current observed for the responsive modified electrodes increased linearly with an increase in 4-chlorophenol concentration (**Fig. 5.3**). The detection limit for the materials ranged from 0.05 mM to 2.8 mM for **9** to **15** and was calculated using data points shown in **Table S9**. The composites showed a lower limit of detection compared to the MOFs alone which agrees with the high currents observed implying superior sensitivity of the composites towards 4-chlorophenol detection compared to the MOFs. The World Health Organization limits the concentration of various chlorophenols in aqueous environment to values less than 2.3 mM (*182*), which suggests that the MPc@MOF composites are suitable for fabrication of sensors for detection of 4-chlorophenol in aqueous medium.

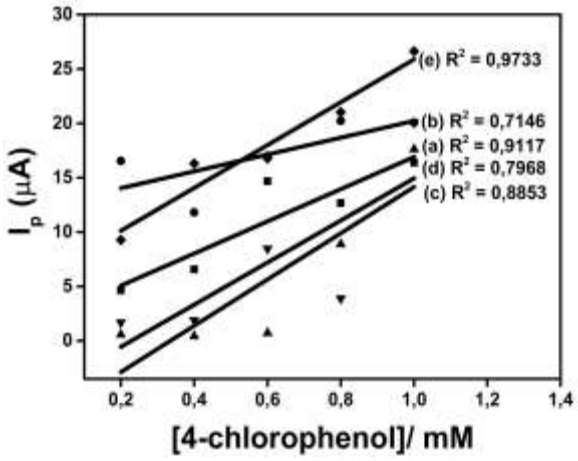

Figure 5.3: Plot of anodic peak current against concentration for the oxidation of 4-chlorophenol on composite (a) **9** (b) **10** (c) **11** (d) **12 and** (e) **15** modified electrodes in pH 7 buffer.

The effect of scan rate on the performance of the newly developed sensors was explored and MPc@MOF modified electrode surfaces were passivated after the first or second scan rate (**Fig. S3**). The FePc@ZIF-8 (**12**) modified electrode however, showed the least electrode fouling compared to the other modified electrodes. **Fig. 5.4** shows the catalytic voltammograms obtained using the FePc@ZIF-8 (**12**) modified electrode and as seen in the graph, catalytic currents increased with increasing scan rate. This suggests that the FePc@ZIF-8 (**12**) modified electrode can be employed in routine monitoring of 4-chlorophenol levels in water for human safety.

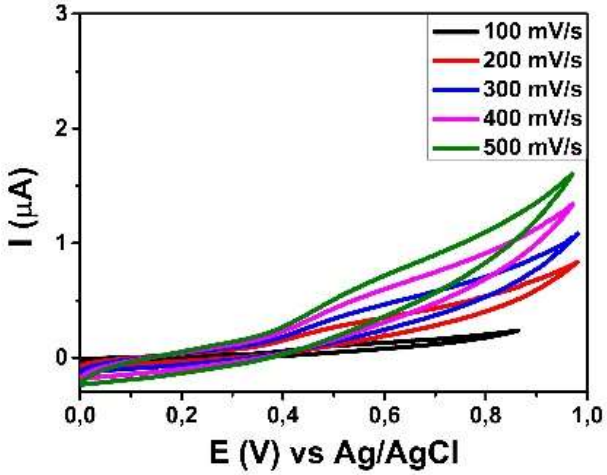

Figure 5.4 Effect of scan rate on 4-chlorophenol oxidation using composite **12** modified electrodes, in pH 7 buffer.

Electrocatalytic oxidation of 4-chlorophenol on MPc@MOF electrocatalysts has been reported in literature (*198, 199*). Therefore, based on these previous reports and the resistance of the FePc@ZIF-8 electrocatalyst to passivation we propose that the reaction mechanism of 4-chlorophenol oxidation on FePc@ZIF-8 (**12**) is as depicted in **Scheme 5.1**. The first step of the reaction is the deprotonation of 4-chlorophenol (step 1) followed by the electrochemical oxidation of Fe^{II} to Fe^{III} (step 2). The oxidised Fe^{III} reacts with the deprotonated 4-chlorophenol in the presence of water molecules to form benzoquinone (step 3).

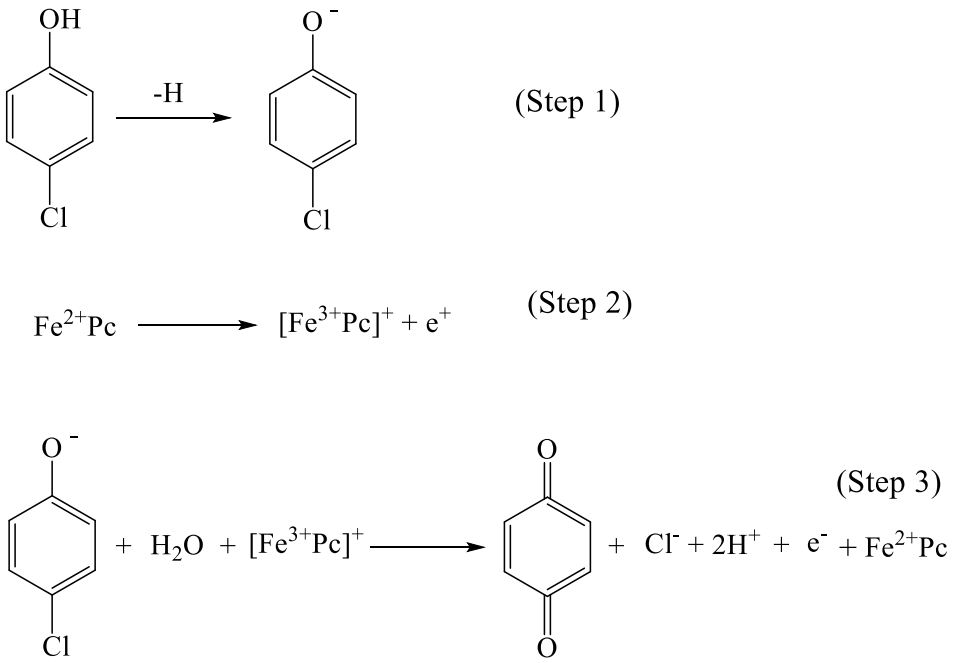

Scheme 5.1: Proposed reaction mechanism for 4-chlorophenol oxidation.

In cyclic voltammetry an electrocatalytic reaction can either be controlled by diffusion or adsorption. Therefore, the reaction kinetics of 4-chlorophenol oxidation on the composite **12** modified electrode were investigated. In diffusion controlled reactions, peak currents are linearly proportional to the square root of the scan rate (*200*) while in adsorption controlled reactions the peak current is linearly proportional to the scan rate. This means that in the case of diffusion, the number of particles diffusing through the catalyst is proportional to the concentration differences across the catalyst while electroactive species migrate from the bulk phase to the interface in the case of adsorption processes. Both processes are dependent on the scan rate, therefore, to determine if the catalysis is diffusion or adsorption controlled the slope of the plot of the logarithm of current against the logarithm of scan rate can be used. The slope is 0.5 for diffusion controlled reactions and 1 for adsorption dominated reactions (*201*). **Fig 5.5** shows the plot of log current (I_p) versus log scan rate (ν) for the oxidation of 4-chlorophenol on FePc@ZIF-8 (**12**) modified electrode. The value of the slope of the graph is 1 indicating an adsorption process. Thus during the detection of 4-chlrophenol in water on the FePc@ZIF-8 (**12**) modified electrode, oxidation is driven by the migration of 4-chlorophenol particles to the catalyst on the electrode surface, hence the adsorption of 4-chlorophenol on FePc@ZIF-8 (**12**) modified electrode.

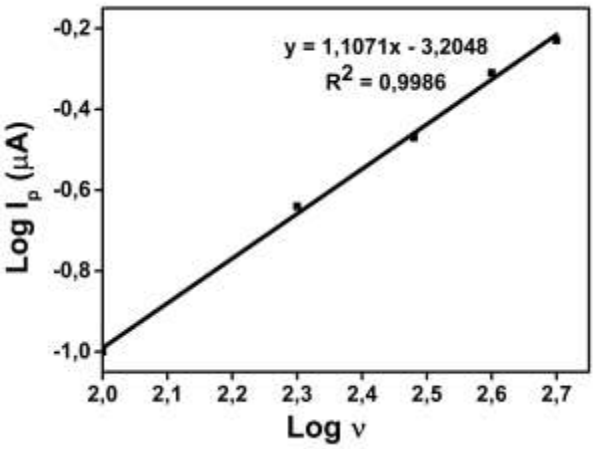

Figure 5.5: Plot of the logarithm of peak current versus the logarithm of scan rate for electro-oxidation of 1 mM 4-chlorophenol on composite **12** modified electrode in pH 7 buffer.

The rate determining step of the adsorption process occurring during the detection of 4-chlorophenol was assessed from the plot of E_p vs log scan rate and equation 5.1 (*202*).

$$E_p = [2.3RT/\,2(1-\alpha)\,n_aF]\,log\,\nu + K \qquad 5.1$$

where E_p is the peak potential, R is the rate constant, T is the temperature, α is the transfer coefficient, n_a is the number of electrons involved in the rate determining step. F is Faraday's constant, ν is the scan rate and K is a constant.

The gradient of the plot in **Fig. 5.6** gives b/2 where b is the tafel slope (*200*), therefore b = 0.059/ (1- α)n_a. Tafel slopes close to 60 mV/decade suggest that the rate determining step is a chemical step that is preceded by a fast one electron transfer process while tafel slopes ~ 120 mV/decade imply that the first electron transfer is the rate determining step. Tafel slopes above 120 mV/decade have been related to a mechanism in which a chemical step or weak substrate-catalyst interaction controls the rate of the reaction. Tafel slope values above 300 mV/decade have been reported and they reflect that the rate of the reaction is determined by strong substrate-catalyst interactions. A tafel slope of 208 mV/decade was obtained for the composite **12** electrocatalyst and because the reaction occurring at the electrode surface is dominated by adsorption, the tafel slope obtained suggests that the rate determining step is the weak interaction between the FePc@ZIF-8 (**12**) composite and intermediate product formed during the oxidation of 4-chlorophenol. Furthermore, the transfer coefficient, α, can be used to determine if the reaction is reactant or product favoured. Transfer coefficient values lie between 0 and 1. α values between 0 and 0.5 indicate that there is a high probability for reactant formation, that is, the reverse reaction is favoured while α values between 0.5 and 1 imply that

there is a high probability for product formation, that is, the forward reaction is favoured. In our work the transfer coefficient, α, was determined to be 0.72 indicating that the oxidation of 4-chlorophenol to benzoquinone on composite **12** modified electrode is a favourable process (*202*, *203*).

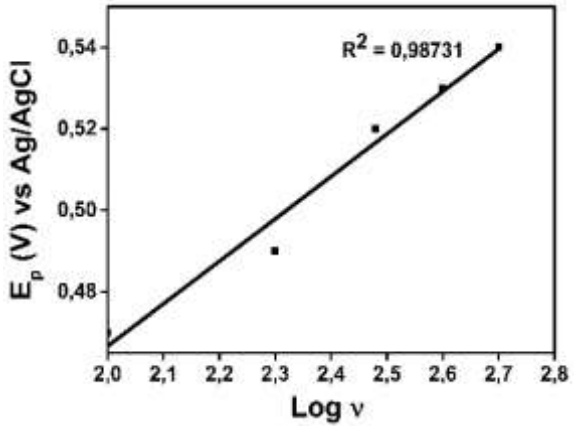

Figure 5.6: Anodic peak potential variation versus the logarithm of scan rate for electro-oxidation of 1 mM 4-chlorophenol on composite **12** modified electrode in pH 7 buffer.

Lastly, the total number of electrons (*n*) transferred during electrocatalysis was determined using equation 5.2 (*204*) .

$$I_p = (2.69 \times 10^5)\, n^{3/2} A C D^{1/2} \nu^{1/2} \qquad 5.2$$

where *A* is the area of the electrode, *C* is the concentration of 4-chlorophenol, and *D* is the diffusion coefficient of 4-chlorophenol.

Approximately four electrons were transferred in total, suggesting that the detection of 4-chlorophenol using the FePc@ZIF-8 (**12)** sensor in water requires the transfer of four electrons between 4-chlorophenol and the FePc@ZIF-8 electrocatalyst which results in the formation of benzoquinone, a well-known product for the electrocatalytic oxidation of 4-chlorophenol.

Chapter 6: Conclusion and future prospects

6.1 Conclusion

In this work, unsubstituted Co, Fe and Mn Pcs were synthesised using a phthalonitrile as the starting material. UV-vis was employed to confirm the formation of the synthesized MPcs. ZIF-8 and UiO-66 MOFs were synthesized and characterised using standard spectroscopic methods which confirmed successful synthesis. The MPcs and MOFs were combined to form MPc@MOF composites which were characterised using appropriate spectroscopic methods. SEM images for ZIF-8 showed the desired rhombic morphology while UiO-66 did not exhibit the expected cubic structure. The composites on the other hand showed agglomeration. Elemental analysis of the composites confirmed successful synthesis as both the elements for MPc and MOF were present for all composites. XRD analysis of the free MOFs and composites confirmed the structural information obtained from SEM analysis as the diffraction patterns of the composites displayed phase transformation through changes in peak intensities, peak position, and peak narrowing. The results obtained from BET analysis revealed that the composites had lower surface areas and pore volumes compared to the free MOFs, further confirming the incorporation of the MPcs within the MOF structures.

The MOFs and corresponding composites were immobilized on GCE using the drop-dry method and the modified electrodes were studied for 4-chlorophenol oxidation. Electrochemical analysis showed that the bare GCE was incapable of oxidising 4-chlorophenol. However, electro-oxidation of 4-chlorophenol was possible upon modification of the electrode surface with the synthesized MOFs and their corresponding composites. The voltammograms obtained showed that 4-chlorophenol oxidation on the fabricated sensors occurred at catalytic potentials between 0.49 - 0.65 V with catalytic currents ranging between 16.39 – 26.62 μA. The peak currents of the composite modified surfaces were higher than when modified with the MOFs alone. This showed that the composites were better catalysts compared to the free MOFs. This implies that the MPcs impart significant improvement on the electrochemical properties of the electrode. The limit of detection of the modified electrodes ranged from 0.05 mM to 2.8 mM. The FePc@ZIF-8 catalyst displayed the best catalytic performance with the lowest LOD. As expected, the free MOFs showed the least electrochemical activity with low currents and high LODs.

6.2 Future prospects

Electrocatalysis is dependent on the materials used for electrode surface modification. Therefore, in future, it would be beneficial to invest in research directed at strategies that will minimise electrode fouling. Understanding the structural contribution of MOFs and MPcs in the detection of 4-chlorophenol is essential, thus size and morphology control of the materials will be explored to find out if these parameters have an effect on the catalytic performance of the fabricated sensors. We will further investigate the effect of pH on the catalytic response of the sensors. Examining the effect of the amount of catalyst used for electrode modification is key to understanding the interaction between the MPc@MOF catalysts and 4-chlorophenol which will be help in developing sensors with improved catalytic activity. The consequences of interfering ions in real wastewater samples on the sensing ability of the modified electrodes will be probed in order to fabricate and reproduce electrochemical sensors with fast electron transfer, very low LOD, and improved sensitivity towards 4-chlorophenol.

Supplementary information

Appendix A

Table S1 showing the elemental compositttion of ZIF-8.

Element	Wt%	Wt% Sigma	Atomic %
N	31.64	0.48	65.07
O	3.55	0.23	6.38
Mn	0.00	0.00	0.00
Fe	0.00	0.00	0.00
Zn	64.71	0.50	28.52
Zr	0.11	0.21	0.03
Total:	100.00		100.00

Table S2 showing the elemental composition of UiO-66.

Element	Wt%	Wt% Sigma	Atomic %
N	2.47	0.48	5.01
O	43.82	0.39	77.88
Cl	0.73	0.07	0.58
Mn	0.07	0.08	0.04
Fe	0.00	0.00	0.00
Zn	0.02	0.13	0.01
Zr	52.90	0.42	16.49
Total:	100.00		100.00

Table S3 showing the elemental composition of FePc@ZIF-8.

Element	Wt%	Wt% Sigma		Atomic %
N	10.77	0.52		29.52
O	6.48	0.23		15.56
Mn	0.00	0.00		0.00
Fe	64.86	0.60		44.60
Zn	16.76	0.45		9.85
Zr	1.13	0.35		0.48
Total:	100.00			100.00

Table S4 showing the elemental comosition of MnPc@ZIF-8.

Element	Wt%	Wt% Sigma	Atomic %
N	22.02	0.58	45.71
O	13.16	0.35	23.92
Mn	19.20	0.29	10.16
Fe	0.00	0.00	0.00
Zn	44.99	0.52	20.01
Zr	0.62	0.29	0.20
Total:	100.00		100.00

Table S5 showing the elemental composition of CoPcZIF-8.

Element	Wt%	Wt% Sigma	Atomic %
Co	68.30	0.68	70.50
Zn	31.70	0.68	29.50
Total:	100.00		100.00

Table S6 showing the elemental composition of FePc@Uio-66.

Element	Wt%	Wt% Sigma	Atomic %
N	19.89	0.58	35.20
O	30.68	0.42	47.54
Mn	0.10	0.09	0.05
Fe	22.16	0.28	9.84
Zn	0.00	0.00	0.00
Zr	27.16	0.37	7.38
Total:	100.00		100.00

Table S7 showing the elemental composition of MnPc@UiO-66.

Element	Wt%	Wt% Sigma	Atomic %
N	2.78	0.49	5.42
O	45.42	0.41	77.48
Mn	8.03	0.15	3.99
Fe	0.10	0.09	0.05
Zn	0.00	0.00	0.00
Zr	43.67	0.40	13.07
Total:	100.00		100.00

Table S8 showing the elemental composition of CoPc@UiO-66.

Element	Wt%	Wt% Sigma	Atomic %
O	19.60	0.34	52.35
Co	38.91	0.35	28.21
Zr	41.49	0.39	19.43
Total:	100.00		100.00

Table S9 Showing data used to calculate the limit of detection of 4-chlorophenol on ZIF-8, UiO-66, CoPc@ZIF-8, FePc@ZIF-8 and FePc@UiO-66 modified electrodes in pH 7 buffer. Scan rate 500 Mv.s^{-1}.

4-chlorophenol concentration (mM)	**ZIF-8 I_p (µA)**	**UiO-66 I_p (µA)**	**CoPc@ZIF-8 I_p (µA)**	**FePc@ZIF-8 I_p (µA)**	**FePc@UiO-66 I_p (µA)**
0.2	4.64	16.55	0.57	1.68	9.28
0.4	6.57	11.82	0.42	1.89	16.31
0.6	14.68	17.00	0.72	8.47	16.78
0.8	12.68	20.23	8.89	3.89	21.03
1.0	16.39	20.08	17.62	20.06	26.62

Appendix B

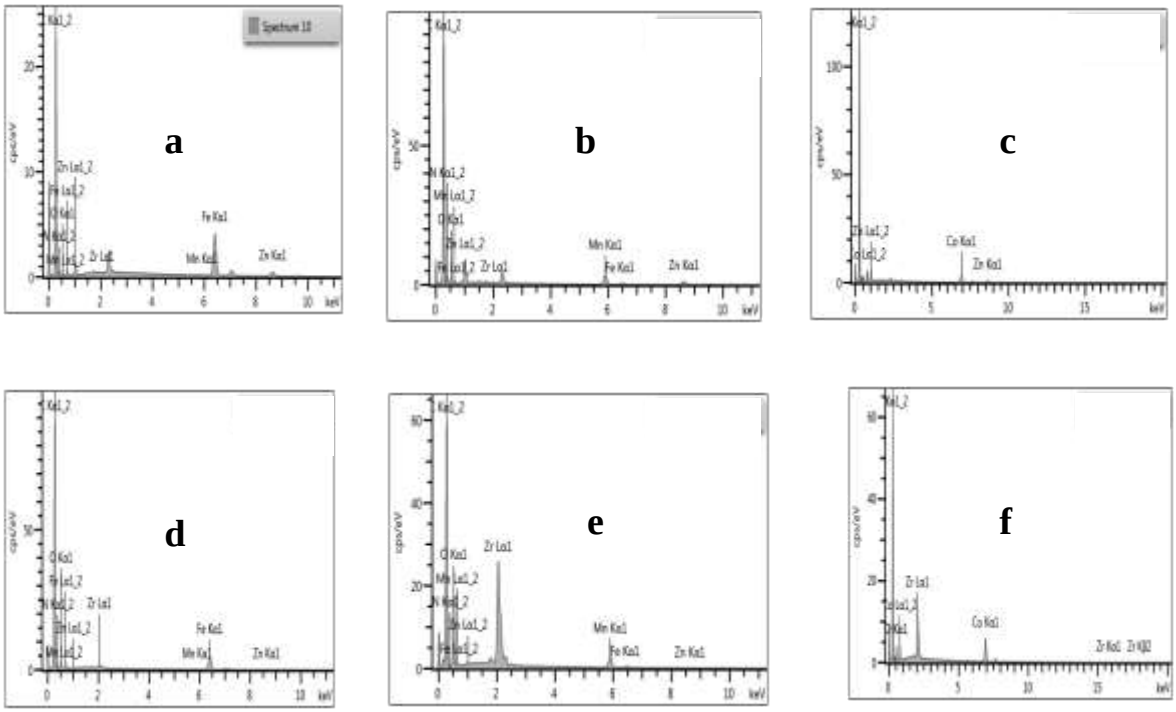

Figure S1: Elemental analysis spectra for MOF composites (a) FePc@ZIF-8 (b) MnPc@ZIF-8 (c) CoPc@ZIF-8 (d) FePc@UiO-66 (e) MnPc@UiO-66 and (f) CoPc@UiO-66.

Appendix C

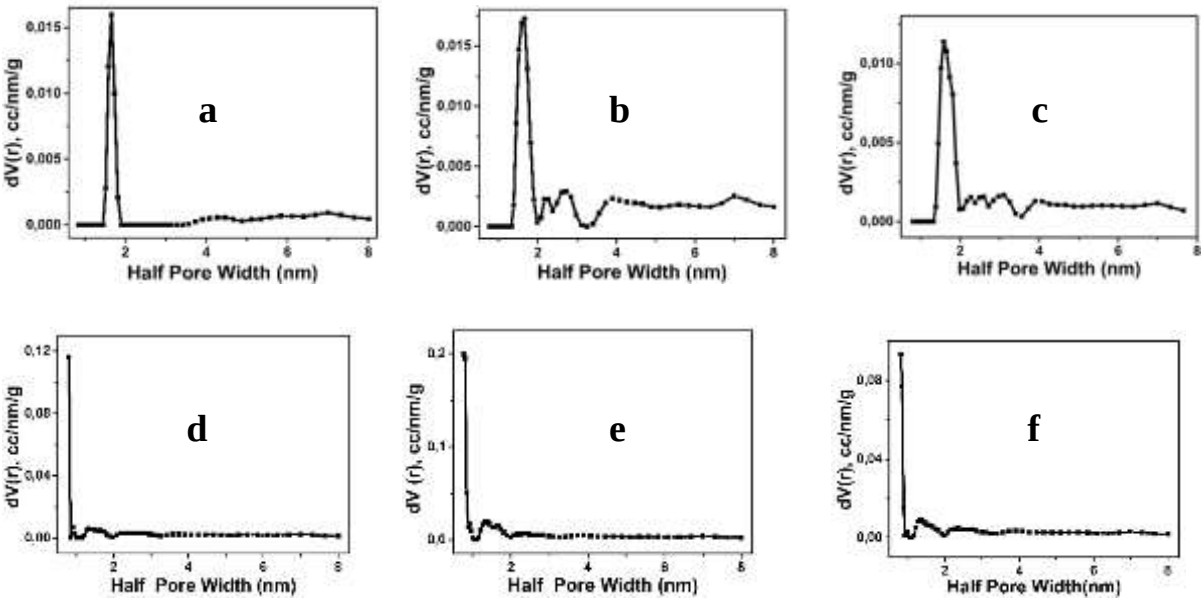

Figure S2: Pore size distribution of MOF composites (a) FePc@ZIF-8 (b) MnPc@ZIF-8 (c) CoPc@ZIF-8 (d) FePc@UiO-66 (e) MnPc@UiO-66 and (f) CoPc@UiO-66.

Appendix D

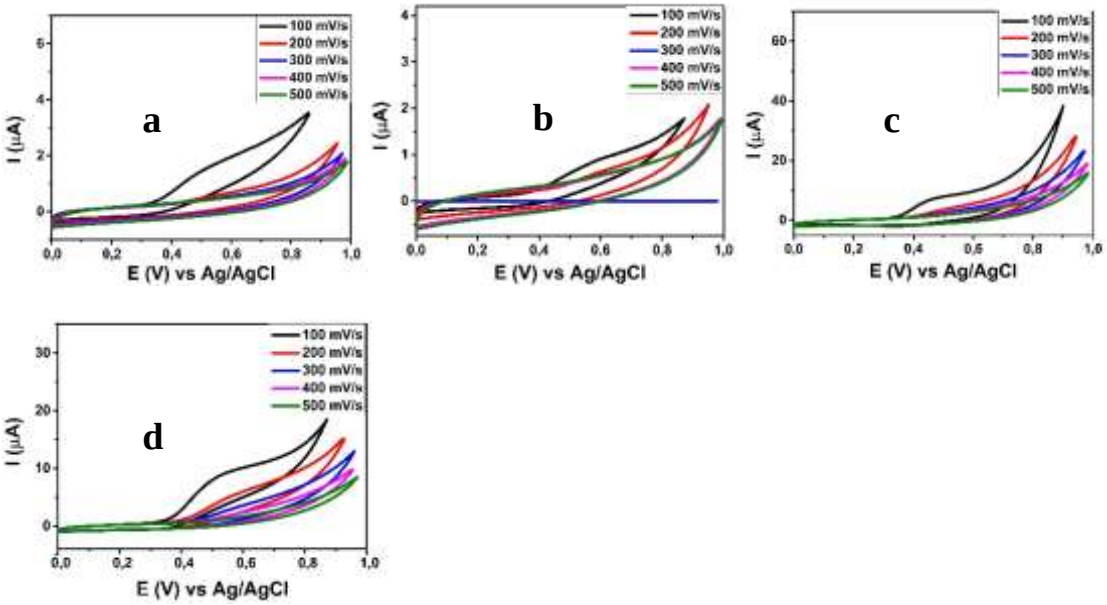

Figure S3: Effecct of scan rate on 4-chlorophenol oxidation using compound (a) **9** (b) **10** (c) **11** and (d) **15** modified electrodes in pH 7 buffer.

References

1. M. M. Zeitoun, E. Mehana, Impact of water pollution with heavy metals on fish health: overview and updates. *Global Veterinaria* **12**, 219-231 (2014).
2. S. Srivastava, A. K. Dwivedi, Biological wastes the tool for biosorption of arsenic. *Journal of Bioremediation & Biodegradation* **7**, 323 (2015).
3. C. Wang, Z. Ying, M. Ma, M. Huo, W. Yang, Degradation of micropollutants by UV–chlorine treatment in reclaimed water: pH effects, formation of disinfectant byproducts, and toxicity assay. *Water* **11**, 2639 (2019).
4. E. M. Wanda, H. Nyoni, B. B. Mamba, T. A. Msagati, Occurrence of emerging micropollutants in water systems in Gauteng, Mpumalanga, and North West Provinces, South Africa. *International journal of environmental research and public health* **14**, 79 (2017).
5. S.-W. Nam, Y. Yoon, S. Chae, J.-H. Kang, K.-D. Zoh, Removal of selected micropollutants during conventional and advanced water treatment processes. *Environmental Engineering Science* **34**, 752-761 (2017).
6. S. U. ODABASI, Removal of Micropollutants in Water with Advanced Treatment Processes.
7. Y.-m. Shi *et al.*, Sensitive acetaminophen electrochemical sensor with amplified signal strategy via non-covalent functionalization of soluble tetrahydroxyphthalocyanine and graphene. *Microchemical Journal* **160**, 105609 (2021).
8. W. Zhang *et al.*, An electrochemical sensor based on electro-polymerization of caffeic acid and Zn/Ni-ZIF-8–800 on glassy carbon electrode for the sensitive detection of acetaminophen. *Biosensors and Bioelectronics* **131**, 200-206 (2019).
9. Ü. Anik, S. Timur, Z. Dursun, Metal organic frameworks in electrochemical and optical sensing platforms: a review. *Microchimica Acta* **186**, 1-15 (2019).
10. S. K. Bhardwaj *et al.*, An overview of different strategies to introduce conductivity in metal–organic frameworks and miscellaneous applications thereof. *Journal of Materials Chemistry A* **6**, 14992-15009 (2018).
11. A. Morozan, F. Jaouen, Metal organic frameworks for electrochemical applications. *Energy & environmental science* **5**, 9269-9290 (2012).
12. F. Zhao, T. Sun, F. Geng, P. Chen, Y. Gao, Metal-organic frameworks-based electrochemical sensors and biosensors. *Int. J. Electrochem. Sci* **14**, 5287-5304 (2019).

13. L. Liu, Y. Zhou, S. Liu, M. Xu, The applications of metal− organic frameworks in electrochemical sensors. *ChemElectroChem* **5**, 6-19 (2018).
14. Ü. Anik, S. Çevik, Double-walled carbon nanotube based carbon paste electrode as xanthine biosensor. *Microchimica Acta* **166**, 209-213 (2009).
15. S. Timur, U. Anik, D. Odaci, L. Gorton, Development of a microbial biosensor based on carbon nanotube (CNT) modified electrodes. *Electrochemistry Communications* **9**, 1810-1815 (2007).
16. T. Q. N. Tran, G. Das, H. H. Yoon, Nickel-metal organic framework/MWCNT composite electrode for non-enzymatic urea detection. *Sensors and Actuators B: Chemical* **243**, 78-83 (2017).
17. J. Xu, Y. Wang, S. Hu, Nanocomposites of graphene and graphene oxides: synthesis, molecular functionalization and application in electrochemical sensors and biosensors. A review. *Microchimica Acta* **184**, 1-44 (2017).
18. W. Zhang *et al.*, Selective Electrochemical Detection of Dopamine on Polyoxometalate-Based Metal–Organic Framework and Its Composite with Reduced Graphene Oxide. *Advanced Materials Interfaces* **4**, 1601241 (2017).
19. H. Hosseini *et al.*, A novel electrochemical sensor based on metal-organic framework for electro-catalytic oxidation of L-cysteine. *Biosensors and Bioelectronics* **42**, 426-429 (2013).
20. H. Hosseini *et al.*, Au-SH-SiO2 nanoparticles supported on metal-organic framework (Au-SH-SiO2@ Cu-MOF) as a sensor for electrocatalytic oxidation and determination of hydrazine. *Electrochimica Acta* **88**, 301-309 (2013).
21. P. Arul, S. A. John, Silver nanoparticles built-in zinc metal organic framework modified electrode for the selective non-enzymatic determination of H2O2. *Electrochimica Acta* **235**, 680-689 (2017).
22. P. Ling, J. Lei, L. Jia, H. Ju, Platinum nanoparticles encapsulated metal–organic frameworks for the electrochemical detection of telomerase activity. *Chemical Communications* **52**, 1226-1229 (2016).
23. P. Falcaro *et al.*, Application of metal and metal oxide nanoparticles@ MOFs. *Coordination Chemistry Reviews* **307**, 237-254 (2016).
24. H. An *et al.*, Incorporation of biomolecules in metal-organic frameworks for advanced applications. *Coordination Chemistry Reviews* **384**, 90-106 (2019).
25. F. Y. Yi, D. Chen, M. K. Wu, L. Han, H. L. Jiang, Chemical sensors based on metal–organic frameworks. *ChemPlusChem* **81**, 675-690 (2016).

26. C. H. Chuang, C. W. Kung, Metal− Organic Frameworks toward Electrochemical Sensors: Challenges and Opportunities. *Electroanalysis* **32**, 1885-1895 (2020).
27. M. D. Brown, M. H. Schoenfisch, Catalytic selectivity of metallophthalocyanines for electrochemical nitric oxide sensing. *Electrochimica acta* **273**, 98-104 (2018).
28. H. Montaseri, P. B. Forbes, Analytical techniques for the determination of acetaminophen: A review. *TrAC Trends in Analytical Chemistry* **108**, 122-134 (2018).
29. M. Zhao, Q. Lu, Q. Ma, H. Zhang, Two-Dimensional Metal–Organic Framework Nanosheets. *Small Methods* **1**, 1600030 (2017).
30. D. Chen, J. Zhao, P. Zhang, S. Dai, Mechanochemical synthesis of metal-organic frameworks. *Polyhedron* **162**, 59-64 (2019).
31. U. Mueller *et al.*, Metal–organic frameworks—prospective industrial applications. *Journal of Materials Chemistry* **16**, 626-636 (2006).
32. A. Anumah *et al.*, Metal-Organic Frameworks (MOFs): Recent Advances in Synthetic Methodologies and Some Applications. *Chemical Methodologies* **3**, 283-305 (2019).
33. J. L. Rowsell, O. M. Yaghi, Metal–organic frameworks: a new class of porous materials. *Microporous and mesoporous materials* **73**, 3-14 (2004).
34. J. D. Evans *et al.*, Metal–organic frameworks in Germany: From synthesis to function. *Coordination Chemistry Reviews* **380**, 378-418 (2019).
35. H. Li, M. Eddaoudi, T. L. Groy, O. Yaghi, Establishing microporosity in open metal− organic frameworks: gas sorption isotherms for Zn (BDC)(BDC= 1, 4-benzenedicarboxylate). *Journal of the American Chemical Society* **120**, 8571-8572 (1998).
36. S. S.-Y. Chui, S. M.-F. Lo, J. P. Charmant, A. G. Orpen, I. D. Williams, A chemically functionalizable nanoporous material [Cu3 (TMA) 2 (H2O) 3] n. *Science* **283**, 1148-1150 (1999).
37. S.-L. Li, Q. Xu, Metal–organic frameworks as platforms for clean energy. *Energy & Environmental Science* **6**, 1656-1683 (2013).
38. T. Mehtab *et al.*, Metal-organic frameworks for energy storage devices: Batteries and supercapacitors. *Journal of Energy Storage* **21**, 632-646 (2019).
39. M. Zhao *et al.*, Two-dimensional metal–organic framework nanosheets: synthesis and applications. *Chemical Society Reviews* **47**, 6267-6295 (2018).
40. Y. Xu, Q. Li, H. Xue, H. Pang, Metal-organic frameworks for direct electrochemical applications. *Coordination Chemistry Reviews* **376**, 292-318 (2018).

41. V. Bon, Metal-organic frameworks for energy-related applications. *Current Opinion in Green and Sustainable Chemistry* **4**, 44-49 (2017).
42. N. Stock, S. Biswas, Synthesis of metal-organic frameworks (MOFs): routes to various MOF topologies, morphologies, and composites. *Chemical reviews* **112**, 933-969 (2011).
43. L. Huang *et al.*, Synthesis, morphology control, and properties of porous metal–organic coordination polymers. *Microporous and mesoporous materials* **58**, 105-114 (2003).
44. J. H. Bang, K. S. Suslick, Applications of ultrasound to the synthesis of nanostructured materials. *Advanced materials* **22**, 1039-1059 (2010).
45. N. A. Khan, I. J. Kang, H. Y. Seok, S. H. Jhung, Facile synthesis of nano-sized metal-organic frameworks, chromium-benzenedicarboxylate, MIL-101. *Chemical engineering journal* **166**, 1152-1157 (2011).
46. A. U. Czaja, N. Trukhan, U. Müller, Industrial applications of metal–organic frameworks. *Chemical Society Reviews* **38**, 1284-1293 (2009).
47. S. Ma, H.-C. Zhou, Gas storage in porous metal–organic frameworks for clean energy applications. *Chemical Communications* **46**, 44-53 (2010).
48. A. R. Millward, O. M. Yaghi, Metal− organic frameworks with exceptionally high capacity for storage of carbon dioxide at room temperature. *Journal of the American Chemical Society* **127**, 17998-17999 (2005).
49. F. X. Llabrés i Xamena, A. Corma, H. Garcia, Applications for metal− organic frameworks (MOFs) as quantum dot semiconductors. *The Journal of Physical Chemistry C* **111**, 80-85 (2007).
50. C. C. Lee, C. I. Chen, Y. T. Liao, K. C. W. Wu, C. C. Chueh, Enhancing efficiency and stability of photovoltaic cells by using perovskite/Zr-MOF heterojunction including bilayer and hybrid structures. *Advanced Science* **6**, 1801715 (2019).
51. T. H. Chang *et al.*, Planar heterojunction perovskite solar cells incorporating metal–organic framework nanocrystals. *Advanced Materials* **27**, 7229-7235 (2015).
52. J. Liu, C. Wöll, Surface-supported metal–organic framework thin films: fabrication methods, applications, and challenges. *Chemical Society Reviews* **46**, 5730-5770 (2017).
53. E. D. Spoerke *et al.*, MOF-sensitized solar cells enabled by a pillared porphyrin framework. *The Journal of Physical Chemistry C* **121**, 4816-4824 (2017).
54. J. Rouquerol *et al.*, Recommendations for the characterization of porous solids (Technical Report). *Pure and applied chemistry* **66**, 1739 (1994).

55. P. Holister, C. R. Vas, T. Harper, Nanoporous materials. *Technology white paper*, (2003).
56. J. Haber, Manual on catalyst characterization (Recommendations 1991). *Pure and applied chemistry* **63**, 1227-1246 (1991).
57. K. S. Walton, R. Q. Snurr, Applicability of the BET method for determining surface areas of microporous metal− organic frameworks. *Journal of the American Chemical Society* **129**, 8552-8556 (2007).
58. M. Thommes *et al.*, Physisorption of gases, with special reference to the evaluation of surface area and pore size distribution (IUPAC Technical Report). *Pure and applied chemistry* **87**, 1051-1069 (2015).
59. C. De Smedt, F. Ferrer, K. Leus, P. Spanoghe, Removal of pesticides from aqueous solutions by adsorption on zeolites as solid adsorbents. *Adsorption Science & Technology* **33**, 457-485 (2015).
60. Q. Bao, Y. Lou, T. Xing, J. Chen, Rapid synthesis of zeolitic imidazolate framework-8 (ZIF-8) in aqueous solution via microwave irradiation. *Inorganic Chemistry Communications* **37**, 170-173 (2013).
61. J. J. Beh, J. K. Lim, E. P. Ng, B. S. Ooi, Synthesis and size control of zeolitic imidazolate framework-8 (ZIF-8): From the perspective of reaction kinetics and thermodynamics of nucleation. *Materials Chemistry and Physics* **216**, 393-401 (2018).
62. Y.-R. Lee *et al.*, ZIF-8: A comparison of synthesis methods. *Chemical Engineering Journal* **271**, 276-280 (2015).
63. J. Troyano, A. Carné-Sánchez, C. Avci, I. Imaz, D. Maspoch, Colloidal metal–organic framework particles: the pioneering case of ZIF-8. *Chemical Society Reviews* **48**, 5534-5546 (2019).
64. Z. Zhao *et al.*, A smart nanoprobe based on a gadolinium complex encapsulated by ZIF-8 with enhanced room temperature phosphorescence for synchronous oxygen sensing and photodynamic therapy. *Dalton Transactions* **48**, 16952-16960 (2019).
65. A. Ahmed, M. Forster, J. Jin, P. Myers, H. Zhang, Tuning morphology of nanostructured ZIF-8 on silica microspheres and applications in liquid chromatography and dye degradation. *ACS applied materials & interfaces* **7**, 18054-18063 (2015).
66. J.-P. Zhang, X.-M. Chen, Crystal engineering of binary metal imidazolate and triazolate frameworks. *Chemical communications*, 1689-1699 (2006).
67. K. Kida, M. Okita, K. Fujita, S. Tanaka, Y. Miyake, Formation of high crystalline ZIF-8 in an aqueous solution. *CrystEngComm* **15**, 1794-1801 (2013).

68. Z. Lai, Development of ZIF-8 membranes: opportunities and challenges for commercial applications. *Current opinion in chemical engineering* **20**, 78-85 (2018).
69. H.-Y. Cho, J. Kim, S.-N. Kim, W.-S. Ahn, High yield 1-L scale synthesis of ZIF-8 via a sonochemical route. *Microporous and Mesoporous Materials* **169**, 180-184 (2013).
70. J.-Q. Jiang, C.-X. Yang, X.-P. Yan, Zeolitic imidazolate framework-8 for fast adsorption and removal of benzotriazoles from aqueous solution. *ACS applied materials & interfaces* **5**, 9837-9842 (2013).
71. K. S. Park *et al.*, Exceptional chemical and thermal stability of zeolitic imidazolate frameworks. *Proceedings of the National Academy of Sciences* **103**, 10186-10191 (2006).
72. J. Cravillon *et al.*, Formate modulated solvothermal synthesis of ZIF-8 investigated using time-resolved in situ X-ray diffraction and scanning electron microscopy. *CrystEngComm* **14**, 492-498 (2012).
73. Y. Pan *et al.*, Tuning the crystal morphology and size of zeolitic imidazolate framework-8 in aqueous solution by surfactants. *CrystEngComm* **13**, 6937-6940 (2011).
74. J. Cravillon *et al.*, Controlling zeolitic imidazolate framework nano-and microcrystal formation: insight into crystal growth by time-resolved in situ static light scattering. *Chemistry of Materials* **23**, 2130-2141 (2011).
75. Y. Pan, Y. Liu, G. Zeng, L. Zhao, Z. Lai, Rapid synthesis of zeolitic imidazolate framework-8 (ZIF-8) nanocrystals in an aqueous system. *Chemical Communications* **47**, 2071-2073 (2011).
76. S. Tanaka, K. Kida, M. Okita, Y. Ito, Y. Miyake, Size-controlled synthesis of zeolitic imidazolate framework-8 (ZIF-8) crystals in an aqueous system at room temperature. *Chemistry Letters* **41**, 1337-1339 (2012).
77. N. L. Torad *et al.*, Facile synthesis of nanoporous carbons with controlled particle sizes by direct carbonization of monodispersed ZIF-8 crystals. *Chemical communications* **49**, 2521-2523 (2013).
78. R. Wu, T. Fan, J. Chen, Y. Li, Synthetic factors affecting the scalable production of zeolitic imidazolate frameworks. *ACS Sustainable Chemistry & Engineering* **7**, 3632-3646 (2019).
79. J. Cravillon *et al.*, Rapid room-temperature synthesis and characterization of nanocrystals of a prototypical zeolitic imidazolate framework. *Chemistry of Materials* **21**, 1410-1412 (2009).

80. X. C. Huang, Y. Y. Lin, J. P. Zhang, X. M. Chen, Ligand-directed strategy for zeolite-type metal–organic frameworks: zinc (II) imidazolates with unusual zeolitic topologies. *Angewandte Chemie International Edition* **45**, 1557-1559 (2006).
81. Y. Wang *et al.*, Synthesis of ZIF-8 in a deep eutectic solvent using cooling-induced crystallisation. *Microporous and mesoporous materials* **195**, 50-59 (2014).
82. A. Schejn *et al.*, Controlling ZIF-8 nano-and microcrystal formation and reactivity through zinc salt variations. *CrystEngComm* **16**, 4493-4500 (2014).
83. F. Yang *et al.*, Morphological map of ZIF-8 crystals with five distinctive shapes: feature of filler in mixed-matrix membranes on C3H6/C3H8 separation. *Chemistry of Materials* **30**, 3467-3473 (2018).
84. C. Avci *et al.*, Self-assembly of polyhedral metal–organic framework particles into three-dimensional ordered superstructures. *Nature chemistry* **10**, 78 (2018).
85. G. Zheng *et al.*, Shape control in ZIF-8 nanocrystals and metal nanoparticles@ ZIF-8 heterostructures. *Nanoscale* **9**, 16645-16651 (2017).
86. S. Yuan, J.-S. Qin, C. T. Lollar, H.-C. Zhou, Stable metal–organic frameworks with group 4 metals: current status and trends. *ACS central science* **4**, 440-450 (2018).
87. J. H. Cavka *et al.*, A new zirconium inorganic building brick forming metal organic frameworks with exceptional stability. *Journal of the American Chemical Society* **130**, 13850-13851 (2008).
88. Z. Hu, D. Zhao, De facto methodologies toward the synthesis and scale-up production of UiO-66-type metal–organic frameworks and membrane materials. *Dalton transactions* **44**, 19018-19040 (2015).
89. M. Bosch, S. Yuan, H. C. Zhou, Group 4 Metals as Secondary Building Units: Ti, Zr, and Hf-based MOFs. *The Chemistry of Metal–Organic Frameworks: Synthesis, Characterization, and Applications* **1**, 137-170 (2016).
90. A. D. Wiersum *et al.*, An evaluation of UiO-66 for gas-based applications. *Chemistry–An Asian Journal* **6**, 3270-3280 (2011).
91. H. Wang, Q. Wang, S. J. Teat, D. H. Olson, J. Li, Synthesis, structure, and selective gas adsorption of a single-crystalline zirconium based microporous metal–organic framework. *Crystal Growth & Design* **17**, 2034-2040 (2017).
92. L. Valenzano *et al.*, Disclosing the complex structure of UiO-66 metal organic framework: a synergic combination of experiment and theory. *Chemistry of Materials* **23**, 1700-1718 (2011).

93. W. Lu *et al.*, Tuning the structure and function of metal–organic frameworks via linker design. *Chemical Society Reviews* **43**, 5561-5593 (2014).
94. K. Tulig, K. S. Walton, An alternative UiO-66 synthesis for HCl-sensitive nanoparticle encapsulation. *Rsc Advances* **4**, 51080-51083 (2014).
95. H. R. Abid *et al.*, Nanosize Zr-metal organic framework (UiO-66) for hydrogen and carbon dioxide storage. *Chemical Engineering Journal* **187**, 415-420 (2012).
96. H. R. Abid, G. H. Pham, H.-M. Ang, M. O. Tade, S. Wang, Adsorption of CH4 and CO2 on Zr-metal organic frameworks. *Journal of colloid and interface science* **366**, 120-124 (2012).
97. I. D. Rahmawati, R. Ediati, D. Prasetyoko, Synthesis of UiO-66 using solvothermal method at high temperature. *IPTEK Journal of Proceedings Series* **1**, (2014).
98. G. C. Shearer *et al.*, Tuned to perfection: ironing out the defects in metal–organic framework UiO-66. *Chemistry of Materials* **26**, 4068-4071 (2014).
99. Q. Zhao, W. Yuan, J. Liang, J. Li, Synthesis and hydrogen storage studies of metal–organic framework UiO-66. *International journal of hydrogen energy* **38**, 13104-13109 (2013).
100. A. Schaate *et al.*, Modulated synthesis of Zr-based metal–organic frameworks: from nano to single crystals. *Chemistry–A European Journal* **17**, 6643-6651 (2011).
101. Y. Bai *et al.*, Zr-based metal–organic frameworks: design, synthesis, structure, and applications. *Chemical Society Reviews* **45**, 2327-2367 (2016).
102. T. Tsuruoka *et al.*, Nanoporous nanorods fabricated by coordination modulation and oriented attachment growth. *Angewandte Chemie* **121**, 4833-4837 (2009).
103. J. Ren, H. W. Langmi, B. C. North, M. Mathe, D. Bessarabov, Modulated synthesis of zirconium-metal organic framework (Zr-MOF) for hydrogen storage applications. *international journal of hydrogen energy* **39**, 890-895 (2014).
104. Y. Han *et al.*, Facile synthesis of morphology and size-controlled zirconium metal–organic framework UiO-66: the role of hydrofluoric acid in crystallization. *CrystEngComm* **17**, 6434-6440 (2015).
105. Z. Wang *et al.*, Nanoscale Zr-Based MOFs with Tailorable Size and Introduced Mesopore for Protein Delivery. *Advanced Functional Materials* **28**, 1707356 (2018).
106. Y.-Y. Zheng *et al.*, Detection of dopamine at graphene-ZIF-8 nanocomposite modified electrode. *Chinese Chemical Letters* **28**, 1473-1478 (2017).
107. S. Lu *et al.*, Synthesis of Au@ ZIF-8 nanocomposites for enhanced electrochemical detection of dopamine. *Electrochemistry Communications* **114**, 106715 (2020).

108. G. Chen *et al.*, Controlled synthesis of Fe 3 O 4@ ZIF-8 nanoparticles for drug delivery. *CrystEngComm* **20**, 7486-7491 (2018).
109. P. Horcajada *et al.*, Flexible porous metal-organic frameworks for a controlled drug delivery. *Journal of the American Chemical Society* **130**, 6774-6780 (2008).
110. H. Kaur, G. C. Mohanta, V. Gupta, D. Kukkar, S. Tyagi, Synthesis and characterization of ZIF-8 nanoparticles for controlled release of 6-mercaptopurine drug. *Journal of Drug Delivery Science and Technology* **41**, 106-112 (2017).
111. A. Sharsheeva *et al.*, Light-controllable systems based on TiO 2-ZIF-8 composites for targeted drug release: communicating with tumour cells. *Journal of Materials Chemistry B* **7**, 6810-6821 (2019).
112. C. Cheng *et al.*, Doxorubicin-loaded Fe3O4-ZIF-8 nano-composites for hepatocellular carcinoma therapy. *Journal of biomaterials applications* **33**, 1373-1381 (2019).
113. H.-X. Zhao *et al.*, Theranostic metal–organic framework core–shell composites for magnetic resonance imaging and drug delivery. *Chemical science* **7**, 5294-5301 (2016).
114. R. Chandra, S. Mukhopadhyay, M. Nath, TiO2@ ZIF-8: A novel approach of modifying micro-environment for enhanced photo-catalytic dye degradation and high usability of TiO2 nanoparticles. *Materials Letters* **164**, 571-574 (2016).
115. S. Panneri *et al.*, C 3 N 4 anchored ZIF 8 composites: photo-regenerable, high capacity sorbents as adsorptive photocatalysts for the effective removal of tetracycline from water. *Catalysis Science & Technology* **7**, 2118-2128 (2017).
116. J. Cao *et al.*, One-step synthesis of Co-doped UiO-66 nanoparticle with enhanced removal efficiency of tetracycline: Simultaneous adsorption and photocatalysis. *Chemical Engineering Journal* **353**, 126-137 (2018).
117. Y. Liu *et al.*, Photostable core-shell CdS/ZIF-8 composite for enhanced photocatalytic reduction of CO2. *Applied Surface Science* **498**, 143899 (2019).
118. J.-J. Zhou *et al.*, In situ growth of CdS nanoparticles on UiO-66 metal-organic framework octahedrons for enhanced photocatalytic hydrogen production under visible light irradiation. *Applied Surface Science* **346**, 278-283 (2015).
119. Z. Wang, G. Yu, J. Xia, F. Zhang, Q. Liu, One-step synthesis of a methylene blue@ ZIF-8-reduced graphene oxide nanocomposite and its application to electrochemical sensing of rutin. *Microchimica Acta* **185**, 1-8 (2018).
120. X. Fu *et al.*, Synthesis of Mn2+ doped ZnS quantum dots/ZIF-8 composite and its applications as a fluorescent probe for sensing Co2+ and dichromate. *Journal of Solid State Chemistry* **264**, 35-41 (2018).

121. J.-B. Huo *et al.*, Magnetic responsive Fe3O4-ZIF-8 core-shell composites for efficient removal of As (III) from water. *Colloids and Surfaces A: Physicochemical and Engineering Aspects* **539**, 59-68 (2018).
122. J.-B. Huo *et al.*, Direct epitaxial synthesis of magnetic Fe3O4@ UiO-66 composite for efficient removal of arsenate from water. *Microporous and Mesoporous Materials* **276**, 68-75 (2019).
123. Y. Yang *et al.*, UiO-66/GO Composites with Improved Electrochemical Properties for Effective Detection of Phosphite (P (III)) in Phosphate (P (V)) Buffer Solutions. *ChemistrySelect* **5**, 10855-10862 (2020).
124. N. Karimian *et al.*, A novel sensing layer based on metal–organic framework UiO-66 modified with TiO 2–graphene oxide: application to rapid, sensitive and simultaneous determination of paraoxon and chlorpyrifos. *New Journal of Chemistry* **43**, 2600-2609 (2019).
125. N. B. McKeown, Phthalocyanine-containing polymers. *Journal of Materials Chemistry* **10**, 1979-1995 (2000).
126. A. Nas, N. Kahriman, H. Kantekin, N. Yaylı, M. Durmuş, The synthesis of novel unmetallated and metallated phthalocyanines including (E)-4-(3-cinnamoylphenoxy) groups at the peripheral positions and photophysicochemical properties of their zinc phthalocyanine derivatives. *Dyes and Pigments* **99**, 90-98 (2013).
127. A. Nas, Ü. Demirbaş, M. Pişkin, M. Durmuş, H. Kantekin, The photophysical and photochemical properties of new unmetallated and metallated phthalocyanines bearing four 5-chloroquinolin-8-yloxy substituents on peripheral sites. *Journal of luminescence* **145**, 635-642 (2014).
128. S. A. RA, J. Keshavayya, M. Harish, S. AH, Synthesis and Studies on 2, 9, 16, 23-tetra anilido nickel (II) Phthalocyanines. *Synthesis* **3**, 1145-1151 (2011).
129. A. Nas, G. Dilber, M. Durmuş, H. Kantekin, The influence of the various central metals on photophysical and photochemical properties of benzothiazole-substituted phthalocyanines. *Spectrochimica Acta Part A: Molecular and Biomolecular Spectroscopy* **135**, 55-62 (2015).
130. R. Linstead, 212. Phthalocyanines. Part I. A new type of synthetic colouring matters. *Journal of the Chemical Society (Resumed)*, 1016-1017 (1934).
131. A. Nas, H. Kantekin, M. Durmuş, N. Gümrükçüoğlu, Unmetallated and metallated phthalocyanines bearing oxadiazole groups: synthesis, photophysical and photochemical studies. *Journal of luminescence* **154**, 15-21 (2014).

132. O. J. Achadu, M. Managa, T. Nyokong, Fluorescence behaviour of supramolecular hybrids containing graphene quantum dots and pyrene-derivatized phthalocyanines and porphyrins. *Journal of Photochemistry and Photobiology A: Chemistry* **333**, 174-185 (2017).
133. D. Mwanza, S. Khene, P. Mashazi, Tetra (4-propargyloxyphenoxy) phthalocyanines: Facile synthesis, fluorescence and thermal properties. *Polyhedron* **134**, 263-274 (2017).
134. Y. Arslanoğlu, T. Nyokong, Synthesis and photophysical studies of monocarboxy phthalocyanines containing quaternizable groups. *Polyhedron* **30**, 2733-2739 (2011).
135. J. D. Wright *et al.*, Crowned and liquid-crystalline phthalocyanines as gas-sensor materials. *Sensors and Actuators B: Chemical* **13**, 276-280 (1993).
136. D. Gounden, N. Nombona, W. E. van Zyl, Recent advances in phthalocyanines for chemical sensor, non-linear optics (NLO) and energy storage applications. *Coordination Chemistry Reviews* **420**, 213359 (2020).
137. D. Qu *et al.*, Highly luminescent S, N co-doped graphene quantum dots with broad visible absorption bands for visible light photocatalysts. *Nanoscale* **5**, 12272-12277 (2013).
138. Z.-M. Dang, Y. Gao, H.-P. Xu, J. Bai, Fabrication and characteristics of organic semiconductor nanoparticles of copper phthalocyanine oligomers. *Journal of colloid and interface science* **322**, 491-496 (2008).
139. S. Banfi *et al.*, Zinc phthalocyanines-mediated photodynamic therapy induces cell death in adenocarcinoma cells. *Journal of organometallic chemistry* **692**, 1269-1276 (2007).
140. Z. U. Islam *et al.*, Fabrication and Photovoltaic Properties of Organic Solar Cell Based on Zinc Phthalocyanine. *Energies* **13**, 962 (2020).
141. P. Sen, M. Managa, T. Nyokong, New type of metal-free and Zinc (II), In (III), Ga (III) phthalocyanines carrying biologically active substituents: Synthesis and photophysicochemical properties and photodynamic therapy activity. *Inorganica Chimica Acta* **491**, 1-8 (2019).
142. V. N. Nemykin, E. A. Lukyanets, Synthesis of substituted phthalocyanines. *Arkivoc* **1**, 136-208 (2010).
143. F. Hacıvelioğlu *et al.*, The synthesis, spectroscopic and thermal properties of phenoxycyclotriphosphazenyl-substituted phthalocyanines. *Dyes and Pigments* **79**, 14-23 (2008).

144. P. Tau, T. Nyokong, Synthesis and photophysical properties of octa-substituted phthalocyaninato oxotitanium (IV) derivatives. *Journal of Porphyrins and Phthalocyanines* **10**, 1040-1048 (2006).
145. P. Tau, T. Nyokong, Electrochemical characterisation of tetra-and octa-substituted oxo (phthalocyaninato) titanium (IV) complexes. *Electrochimica acta* **52**, 3641-3650 (2007).
146. P. Yiru, H. Fenghua, L. Zhipeng, C. Naisheng, H. Jinling, Synthesis and characterization of an unsymmetrical diimide-disulfonato phthalocyaninatozinc dipotassium salt. *Inorganic Chemistry Communications* **7**, 967-970 (2004).
147. D. L. Pavia, G. M. Lampman, G. S. Kriz, J. A. Vyvyan, *Introduction to spectroscopy*. (Cengage Learning, 2008).
148. B. Ortiz, S. M. Park, N. Doddapaneni, Electrochemical and spectroelectrochemical studies of cobalt phthalocyanine polymers. *Journal of The Electrochemical Society* **143**, 1800 (1996).
149. M. Canlıca, T. Nyokong, Synthesis and photophysical properties of metal free, titanium, magnesium and zinc phthalocyanines substituted with a single carboxyl and hexylthio groups. *Polyhedron* **30**, 1975-1981 (2011).
150. G. Mbambisa, T. Nyokong, Synthesis and electrochemical characterisation of a near infrared absorbing oxo vanadium (IV) octapentylthio-phthalocyanine. *Polyhedron* **27**, 2799-2804 (2008).
151. J. H. Zagal, F. Bedioui, *Electrochemistry of N4 macrocyclic metal complexes*. (Springer, 2016), vol. 2.
152. T. Nyokong, in *N4-Macrocyclic Metal Complexes*. (Springer, 2006), pp. 315-361.
153. J. H. Zagal, Metallophthalocyanines as catalysts in electrochemical reactions. *Coordination Chemistry Reviews* **119**, 89-136 (1992).
154. G. I. Cárdenas-Jiron *et al.*, Reactivity of electrodes modified with substituted metallophthalocyanines. Correlations with redox potentials, Hammett parameters and donor–acceptor intermolecular hardness. *Electrochimica acta* **46**, 3227-3235 (2001).
155. F. Bedioui *et al.*, Tuning the redox properties of metalloporphyrin-and metallophthalocyanine-based molecular electrodes for the highest electrocatalytic activity in the oxidation of thiols. *Physical Chemistry Chemical Physics* **9**, 3383-3396 (2007).
156. M. A. Gulppi *et al.*, Inverted correlations between rate constants and redox potential of the catalyst for the electrooxidation of 2-aminoethanethiol mediated by surface

confined substituted cobalt-phthalocyanines. *Journal of Electroanalytical Chemistry* **580**, 50-56 (2005).

157. S. Maree, T. Nyokong, Electrocatalytic behavior of substituted cobalt phthalocyanines towards the oxidation of cysteine. *Journal of Electroanalytical Chemistry* **492**, 120-127 (2000).
158. P. Christensen, A. Hamnet, *Techniques and mechanisms in electrochemistry*. (Springer Science & Business Media, 2007).
159. P. T. Kissinger, W. R. Heineman, Cyclic voltammetry. *Journal of Chemical Education* **60**, 702 (1983).
160. D. H. Evans, K. M. O'Connell, R. A. Petersen, M. J. Kelly. (ACS Publications, 1983).
161. G. A. Mabbott, An introduction to cyclic voltammetry. *Journal of Chemical education* **60**, 697 (1983).
162. C.-H. Lee, R. Filler, J. Lee, J. Li, B. K. Mandal, Synthesis and hydrogen adsorption properties of a new phthalocyanine-based metal–organic framework. *Renewable Energy* **35**, 1592-1595 (2010).
163. H. Nagatomi, N. Yanai, T. Yamada, K. Shiraishi, N. Kimizuka, Synthesis and Electric Properties of a Two-Dimensional Metal-Organic Framework Based on Phthalocyanine. *Chemistry–A European Journal* **24**, 1806-1810 (2018).
164. H. Jia *et al.*, A novel two-dimensional nickel phthalocyanine-based metal–organic framework for highly efficient water oxidation catalysis. *Journal of Materials Chemistry A* **6**, 1188-1195 (2018).
165. Z. Sha, H. S. O. Chan, J. Wu, Ag2CO3/UiO-66 (Zr) composite with enhanced visible-light promoted photocatalytic activity for dye degradation. *Journal of hazardous materials* **299**, 132-140 (2015).
166. R. Lin *et al.*, Enhanced photocatalytic hydrogen production activity via dual modification of MOF and reduced graphene oxide on CdS. *Chemical Communications* **50**, 8533-8535 (2014).
167. Y.-P. Yuan *et al.*, Improving photocatalytic hydrogen production of metal–organic framework UiO-66 octahedrons by dye-sensitization. *Applied Catalysis B: Environmental* **168**, 572-576 (2015).
168. Q. Liang *et al.*, Zinc phthalocyanine coupled with UIO-66 (NH2) via a facile condensation process for enhanced visible-light-driven photocatalysis. *Journal of Alloys and Compounds* **690**, 123-130 (2017).

169. G. R. Monama *et al.*, Palladium deposition on copper (II) phthalocyanine/metal organic framework composite and electrocatalytic activity of the modified electrode towards the hydrogen evolution reaction. *Renewable Energy* **119**, 62-72 (2018).
170. G. R. Monama *et al.*, Copper (II) phthalocyanine/metal organic framework electrocatalyst for hydrogen evolution reaction application. *International Journal of Hydrogen Energy* **44**, 18891-18902 (2019).
171. G. R. Monama *et al.*, Hierarchiral 4-tetranitro copper (II) phthalocyanine based metal organic framework hybrid composite with improved electrocatalytic efficiency towards hydrogen evolution reaction. *Results in Physics* **15**, 102564 (2019).
172. J. Peng *et al.*, Novel porous iron phthalocyanine based metal–organic framework electrochemical sensor for sensitive vanillin detection. *RSC Advances* **10**, 36828-36835 (2020).
173. S. Lu *et al.*, Two-dimensional conductive phthalocyanine-based metal–organic frameworks for electrochemical nitrite sensing. *RSC Advances* **11**, 4472-4477 (2021).
174. Z. Zeng *et al.*, Electrochemically sensing of trichloroacetic acid with iron (II) phthalocyanine and Zn-based metal organic framework nanocomposites. *ACS sensors* **4**, 1934-1941 (2019).
175. F. Owa, Water pollution: sources, effects, control and management. *Mediterranean journal of social sciences* **4**, 65 (2013).
176. A. Anju, P. Ravi S, S. Bechan, Water pollution with special reference to pesticide contamination in India. *Journal of Water Resource and Protection* **2010**, (2010).
177. M.-K. Kim, K.-D. Zoh, Occurrence and removals of micropollutants in water environment. *Environmental Engineering Research* **21**, 319-332 (2016).
178. R. Rosen, Mass spectrometry for monitoring micropollutants in water. *Current Opinion in Biotechnology* **18**, 246-251 (2007).
179. L. Wang, Q. Sun, Y. Liu, Z. Lu, Voltammetric determination of 4-chlorophenol using multiwall carbon nanotube/gold nanoparticle nanocomposite modified glassy carbon electrodes. *RSC advances* **6**, 34692-34698 (2016).
180. Y. Zhu, M. Wu, S. Liu, Self-assembly of Ag-phosphotungstic acid composite nanoparticles on a modified ITO electrode for the electrochemical detection of 4-chlorophenol. *Journal of Applied Electrochemistry* **43**, 1035-1041 (2013).
181. C. Qiu, X. Dong, H. Ma, S. Hou, J. Yang, Electrochemical Behavior and Amperometric Detection of 4-Chlorophenol on Nano-Au Thin Films Modified Glassy Carbon Electrode. *Electroanalysis* **24**, 1201-1206 (2012).

182. Y. Yang, N. Ma, Z. Bian, Cu-Au/rGO nanoparticle based electrochemical sensor for 4-chlorophenol detection. *Int. J. Electrochem. Sci* **14**, 4095-4113 (2019).
183. M. Li, E. Khoshdel, D. M. Haddleton, Synthesis of water soluble PEGylated (copper) phthalocyanines via Mitsunobu reaction and Cu (i)-catalysed azide–alkyne cycloaddition (CuAAC)"click" chemistry. *Polymer Chemistry* **4**, 4405-4411 (2013).
184. S. Gökçe, E. T. Saka, Z. Bıyıklıoğlu, H. Kantekin, Synthesis, characterization of metal-free, metallophthalocyanines and catalytic activity of cobalt phthalocyanine in cyclohexene oxidation. *Synthetic metals* **176**, 108-115 (2013).
185. L. Y. Molefe *et al.*, Polymer-Based Shaping Strategy for Zeolite Templated Carbons (ZTC) and Their Metal Organic Framework (MOF) Composites for Improved Hydrogen Storage Properties. *Frontiers in chemistry* **7**, 864 (2019).
186. R. D. George, A. W. Snow, Synthesis of 3-nitrophthalonitrile and tetra-α-substituted phthalocyanines. *Journal of Heterocyclic Chemistry* **32**, 495-498 (1995).
187. J. D. Blakemore, J. F. Hull, R. H. Crabtree, G. W. Brudvig, Aqueous speciation and electrochemical properties of a water-soluble manganese phthalocyanine complex. *Dalton Transactions* **41**, 7681-7688 (2012).
188. F. Rückerl *et al.*, Charge transfer from and to manganese phthalocyanine: bulk materials and interfaces. *Beilstein journal of nanotechnology* **8**, 1601-1615 (2017).
189. H. Peisert, J. Uihlein, F. Petraki, T. Chassé, Charge transfer between transition metal phthalocyanines and metal substrates: The role of the transition metal. *Journal of Electron Spectroscopy and Related Phenomena* **204**, 49-60 (2015).
190. J. Ren *et al.*, Microwave-assisted modulated synthesis of zirconium-based metal–organic framework (Zr-MOF) for hydrogen storage applications. *International journal of materials research* **105**, 516-519 (2014).
191. T. Xing, Y. Lou, Q. Bao, J. Chen, Surfactant-assisted synthesis of ZIF-8 nanocrystals in aqueous solution via microwave irradiation. *CrystEngComm* **16**, 8994-9000 (2014).
192. K. S. Sing, Reporting physisorption data for gas/solid systems with special reference to the determination of surface area and porosity (Recommendations 1984). *Pure and applied chemistry* **57**, 603-619 (1985).
193. M. Du, L. Cui, F. Liu, A New Reversible Phase Transformation of Intermetallic Ti3Sn. *Materials* **12**, 2484 (2019).
194. A. D. Prasetya, M. Rifai, H. Miyamoto, in *Journal of Physics: Conference Series*. (IOP Publishing, 2020), vol. 1436, pp. 012113.

195. M. D. Yadav, in *Handbook of Nanomaterials for Wastewater Treatment*. (Elsevier, 2021), pp. 513-534.
196. L. Zhang, A. A. Gonçalves, M. Jaroniec, Identification of preferentially exposed crystal facets by X-ray diffraction. *RSC Advances* **10**, 5585-5589 (2020).
197. Y. He *et al.*, Preparation, characterization, and photocatalytic activity of novel AgBr/ZIF-8 composites for water purification. *Advanced Powder Technology* **31**, 439-447 (2020).
198. B. Agboola, T. Nyokong, Electrocatalytic oxidation of chlorophenols by electropolymerised nickel (II) tetrakis benzylmercapto and dodecylmercapto metallophthalocyanines complexes on gold electrodes. *Electrochimica acta* **52**, 5039-5045 (2007).
199. S. Khene, K. Lobb, T. Nyokong, Interaction between nickel hydroxy phthalocyanine derivatives with p-chlorophenol: Linking electrochemistry experiments with theory. *Electrochimica acta* **56**, 706-716 (2010).
200. M. A. Kamyabi, S. Shahabi, H. Hosseini-Monfared, Electrocatalytic oxidation of hydrazine at a cobalt (II) Schiff-base-modified carbon paste electrode. *Journal of The Electrochemical Society* **155**, F8 (2007).
201. S. Nyoni, T. Nyokong, Electrocatalytic behahiour of cobalt tetraamino-phthalocyanine in the presence of a composite of reduced graphene nanosheets and of multi-walled carbon nanotubes. *Electrochimica Acta* **136**, 240-249 (2014).
202. P. Tau, T. Nyokong, Electrocatalytic activity of arylthio tetra-substituted oxotitanium (IV) phthalocyanines towards the oxidation of nitrite. *Electrochimica Acta* **52**, 4547-4553 (2007).
203. N. Nombona, P. Tau, N. Sehlotho, T. Nyokong, Electrochemical and electrocatalytic properties of α-substituted manganese and titanium phthalocyanines. *Electrochimica acta* **53**, 3139-3148 (2008).
204. A. J. Bard, L. R. Faulkner, Fundamentals and applications. *Electrochemical methods* **2**, 580-632 (2001).